



UNIVERSIDAD NACIONAL AUTÓNOMA DE MÉXICO

POSGRADO EN ASTROFÍSICA

ASTROFÍSICA OBSERVACIONAL

**STUDY OF THE STELLAR PHYSICS THROUGH INFRARED
INTERFEROMETRIC IMAGING**

TESIS

**QUE PARA OPTAR POR EL GRADO DE:
DOCTOR EN CIENCIAS (ASTROFÍSICA)**

PRESENTA:

JESÚS ABEL ROSALES GUZMÁN

TUTOR PRINCIPAL

**DR. JOEL SÁNCHEZ BERMÚDEZ
(INSTITUTO DE ASTRONOMÍA, UNAM - CU)**

MIEMBROS DEL COMITÉ TUTOR

**DRA. IRENE ANTONIA CRUZ GONZÁLEZ ESPINOSA
(INSTITUTO DE ASTRONOMÍA, UNAM - CU)**

**DR. JULIO CÉSAR RAMÍREZ VELEZ
(INSTITUTO DE ASTRONOMÍA, UNAM - ENSENADA)**

Ciudad Universitaria, Ciudad de México, Abril de 2024



Universidad Nacional
Autónoma de México

Dirección General de Bibliotecas de la UNAM

Biblioteca Central



UNAM – Dirección General de Bibliotecas
Tesis Digitales
Restricciones de uso

DERECHOS RESERVADOS ©
PROHIBIDA SU REPRODUCCIÓN TOTAL O PARCIAL

Todo el material contenido en esta tesis esta protegido por la Ley Federal del Derecho de Autor (LFDA) de los Estados Unidos Mexicanos (México).

El uso de imágenes, fragmentos de videos, y demás material que sea objeto de protección de los derechos de autor, será exclusivamente para fines educativos e informativos y deberá citar la fuente donde la obtuvo mencionando el autor o autores. Cualquier uso distinto como el lucro, reproducción, edición o modificación, será perseguido y sancionado por el respectivo titular de los Derechos de Autor.

Agradecimientos

Sin duda alguna, el doctorado ha sido uno de los viajes más largos, difíciles e, irónicamente, gratificantes en mi vida, tanto personal como académica. Por ello, deseo expresar mi profundo agradecimiento a todas aquellas personas que compartieron sus conocimientos y experiencia conmigo en este camino.

En primer lugar quiero agradecer a mi asesor Joel Sánchez por haberme guiado a lo largo de este proceso, por esas discusiones que me llevaron a entender las cosas que se me complicaban y por alentarme siempre a desarrollar nuevas ideas para poner en práctica. Agradezco también a los miembros de mi comité tutor, Irene Cruz y Julio Ramirez por haberme mostrado siempre su apoyo en los momentos difíciles y guiarme siempre hacia adelante en cada reunión.

Agradezco a mis sinodales Julio Ramirez, Gisela Ortíz, Jesús Toalá, Laurence Sabin y Aina Palau por sus valiosos comentarios y correcciones que ayudaron a mejorar en gran manera el contenido que se encuentra a lo largo de éstas páginas.

Finally, I would like to express my heartfelt gratitude to Claudia Paladini, whose invaluable guidance has been instrumental throughout my doctoral journey. Not only has she shared her wealth of knowledge with me, but she has also extended her generosity by inviting me to collaborate with her in Chile. Thank you very much Claudia for all your kindness.

Yo Jesús Abel Rosales Guzmán agradezco al proyecto CONAHCyT “Ciencia de Frontera” CF-2019/263975 y al proyecto UNAM PAPIIT IA 105023 por el apoyo brindado para la realización de esta tesis. Agradezco también a CONAHCYT por el apoyo financiero otorgado a través de la beca doctoral con número 760678.

Resumen

¿Qué mecanismos dan lugar a la pérdida de masa y a la formación de estructuras asimétricas de gas y polvo en estrellas AGB (Asymptotic Giant Branch, por sus siglas en inglés)? ¿Qué tan importante es la composición química del gas y polvo circundante a las estrellas para la formación de vientos? ¿Cómo funciona la convección en estrellas diferentes al Sol? Al día de hoy, éstas son preguntas que no tienen una respuesta concreta. Aunque las estrellas AGB son de las principales contribuyentes al enriquecimiento del medio interestelar, la manera en la que el material procesado durante la evolución de la estrella es devuelto al medio interestelar es un fenómeno que no se encuentra caracterizado completamente. En particular las estrellas AGB de tipo M (o ricas en O, Capítulo 1) son de las menos entendidas debido a la enorme complejidad química existente en las partes más cercanas a la estrella, donde ocurren las primeras interacciones que dan lugar a la subsecuente pérdida de masa.

Una de las dificultades encontradas al tratar de observar las regiones más internas de estrellas AGB es la alta resolución angular necesaria para su estudio. Por ejemplo, la envoltura circunestelar de polvo de una estrella AGB, observada a $11 \mu\text{m}$, tiene un tamaño angular aproximado de 50 milisegundos de arco (mas) equivalentes a 50 UA a una distancia de 1 kilopársec (kpc). Para poder resolver un objeto con este tamaño angular necesitaríamos un telescopio de al menos 45 m de diámetro. Si nos vamos a regiones todavía más internas con tamaños de unos pocos mas, necesitaríamos telescopios cada vez más grandes, con un costo que se dispara de manera exponencial. Es entonces que el uso de interferómetros (Capítulo 2) adquiere una enorme importancia para estudiar estructuras con tamaños angulares tan pequeños como algunos mas con el fin de brindar pistas que nos ayuden a entender que ocurre en el intrincado y complejo entorno de las estrellas AGB.

IV

Esta tesis se centra en el estudio de estrellas AGB con interferometría infrarroja. De manera más concreta, presento un análisis de las partes más internas ($1-3 R_*$) de la estrella Mira R Car utilizando datos interferométricos adquiridos con los instrumentos PIONIER y GRAVITY del VLTI (Very Large Telescope Interferometer, por sus siglas en inglés) en las bandas H ($1.6 - 1.99 \mu\text{m}$) y K ($2.0 - 2.4 \mu\text{m}$) en el infrarrojo cercano.

El trabajo de tesis está dividido en 5 capítulos que abarcan tres partes principales. Los primeros dos capítulos ofrecen una introducción a las estrellas AGB y a la interferometría infrarroja, respectivamente. En el Capítulo 3 titulado **Interferometric analysis of the M-type Mira star R Car with PIONIER-VLTI** exploramos la superficie estelar de R Car en la banda H en dos épocas diferentes separadas por alrededor de 7 años. La resolución angular alcanzada nos permitió detectar una serie de estructuras brillantes en la superficie de la estrella que cambian de posición y tamaño en el tiempo. Fuimos capaces de determinar el tamaño de estas estructuras y realizamos comparaciones de tamaño con extrapolaciones de diferentes modelos de convección que fueron desarrollados para estrellas gigantes, enanas y enanas blancas. Aunque a la fecha no existen modelos específicos de convección para cada AGB, no es del todo incorrecto pensar que los procesos que gobiernan la convección deben ser similares en todas las estrellas a lo largo del diagrama Hertzsprung–Russell (HR). Es por ello que pudimos comparar nuestros resultados con extrapolaciones de modelos diseñados para otro tipo de estrellas. Derivado de estas comparaciones encontramos que las estructuras observadas en la superficie de R Car son consistentes en tamaño con las extrapolaciones usadas, lo cual sugiere que tales estructuras brillantes pueden estar asociadas a células convectivas. Poder observar y caracterizar tales estructuras estelares y sus cambios temporales nos abre la puerta para brindar nueva y mejor evidencia observacional que nos permita entender mejor los modelos actuales de convección, los cuales, a pesar de ser muy abundantes, carecen de un soporte observacional en el cual basarse.

El mecanismo más aceptado para la pérdida de masa en la fase de AGB es un proceso de 2 pasos, (i) las pulsaciones de la estrella elevan el gas a una distancia a partir de la cual el polvo puede comenzar a condensarse y (ii) la radiación de la estrella acelera al gas y polvo hasta escapar del potencial gravitacional. Aunque este esquema funciona, algo que no se entiende del todo bien es ¿Qué tipos de granos de polvo son eficientes para transportar dicha radiación, ya sea mediante absorción o dispersión? Para arrojar luz sobre este problema es indispensable poder observar las capas de gas más

cercanas a la superficie de la estrella, por lo que, además de una buena resolución angular, necesitamos una ventana donde el polvo sea lo más transparente posible. En las estrellas AGB de tipo M se cumple el segundo requisito observando en la banda K , razón por la cual en el Capítulo 4 titulado **Interferometric Analysis of the Mira star R Car with GRAVITY-VLTI** llevamos a cabo la caracterización de las capas gaseosas más próximas a la superficie estelar en esta banda en dos épocas diferentes separadas por alrededor de 1 mes.

La importancia de este estudio radica en que las condiciones físicas de temperatura y densidad en las que se encuentra el gas, principalmente el CO, son compatibles con las regiones donde se origina el polvo que da lugar a los vientos y a la pérdida de masa en este tipo de estrellas. En el análisis de estos datos encontramos que la distribución de las capas de gas que rodean a la estrella es asimétrica y cambia de forma en periodos cortos de tiempo. Al ser capaces de estimar la temperatura, tamaño y densidad de las capas de gas más internas, pudimos determinar de manera observacional si los tipos de granos de polvo propuestos como "*wind-drivers*" pueden o no ser eficientes para transportar la radiación de la estrella.

Una manera de comprobar si las afirmaciones hechas en el Capítulo 4 sobre los posibles "*wind-drivers*" que se encuentran distribuidos en diferentes capas alrededor de la estrella es mediante la observación y caracterización de sus transiciones moleculares. Dado que éstas no pueden ser detectadas en las bandas H y K , para comprobar su existencia en las cercanías de la estrella sería necesario observar en las bandas L (3.2 - 3.9 μm), M (4.5 - 5.0 μm) y N (8 - 13 μm) principalmente, ya que es ahí donde se espera que ocurran tales transiciones. En el Capítulo 5 se plantea como trabajo a futuro la caracterización de las capas más externas de gas y polvo, observadas en las bandas mencionadas previamente.

Esta tesis tiene como objetivo científico inmediato brindar, por primera vez, un estudio detallado desde adentro hacia afuera de las diferentes regiones de una AGB rica en O para brindar evidencias observacionales y mejorar los modelos actuales de convección y de pérdida de masa, además de motivar los estudios observacionales periodicos y detallados con técnicas de alta resolución angular.

Producción Científica

Artículos de primer autor

Mi trabajo doctoral tuvo como resultado la escritura de dos artículos originales, los cuales listo a continuación. El primero de ellos ya se encuentra publicado y el segundo está en proceso de revisión por pares. Ambos fueron enviados a la revista *Astronomy & Astrophysics*.

1. Imaging the innermost gaseous layers of the M-type Mira star R Car with GRAVITY-VLTI

A. Rosales-Guzmán, J. Sanchez-Bermudez, C. Paladini, A. Alberdi, W. Brandner, E. Cannon, G. González-Torà, X. Haubois, Th. Henning, P. Kervella, M. Montarges, G. Perrin, R. Schödel, M. Wittkowski

Publicado en 2023 (A&A 674, A62)

2. A new dimension in the variability of AGB stars: convection patterns size changes with pulsation

A. Rosales-Guzmán, J. Sanchez-Bermudez, C. Paladini, B. Freytag, M. Wittkowski, A. Alberdi, F. Baron, J.-P. Berger, A. Chiavassa, S. Höfner, A. Jorissen, P. Kervella, J.-B. Le Bouquin, P. Marigo, M. Montargès, M. Trabucchi, S. Tsvetkova, R. Schödel, S. Van Eck

Enviado a A&A y en proceso de revisión por pares.

Artículos en colaboración

Además de los artículos previamente mencionados, durante mi doctorado tuve la oportunidad de colaborar en dos artículos y un proceeding. Estas contribuciones las listo a continuación junto con una descripción de mi participación en los proyectos.

1. The dusty circumstellar environment of Betelgeuse during the Great Dimming as seen by VLTI/MATISSE.

E. Cannon, M. Montargès, A. de Koter, A. Matter, J. Sanchez-Bermudez, R. Norris, C. Paladini, L. Decin, H. Sana, J.O. Sundqvist, E. Lagadec, P. Kervella, A. Chiavassa, A. K. Dupree, G. Perrin, P. Scicluna, P. Stee, S. Kraus, W. Danchi, B. Lopez, F. Millour, J. Drevon, P. Cruzalèbes, P. Berio, S. Robbe-Dubois, and **A. Rosales-Guzmán**

Publicado en 2023 (A&A, 675, A46)

En este artículo, liderado por Emily Cannon, se da una explicación a la disminución del brillo de la estrella gigante roja Betelgeuse, ocurrida a finales de 2019 e inicios de 2020, utilizando datos interferométricos en la banda N del infrarrojo medio. Mi participación en este proyecto consistió en revisar si era posible reconstruir una imagen de la estrella a partir de los datos interferométricos. Dada la calidad de estos datos no fue posible reconstruir la imagen pero se dieron condiciones para lograr esto con futuras observaciones.

2. An impressionist view of V Hydrae.

L. Planquart, C. Paladini, A. Jorissen, A. Escorza, E. Pantin, J. Drevon, B. Aringer, F. Baron, A. Chiavassa, P. Cruzalèbes, W. Danchi, E. De Beck, M.A.T. Groenewegen, S. , Höfner , J. Hron, T. Khouri, B. Lopez, F. Lykou, M. Montarges, N. Nardetto, K. Ohnaka, H. Olofsson, G. Rau, **A. Rosales-Guzmán**, J. Sanchez-Bermudez, P. Scicluna, L. Siess, F. Th'evenin, S. Van Eck, W.H.T. Vlemmings, G. Weigelt, M. Wittkowski

En segunda revisión por pares.

En este artículo, liderado por Lèa Planquart, se explora la posibilidad de que la estrella AGB V Hydrae tenga una compañera binaria en su región de formación de polvo, a menos de $10 R_*$. Se exploran además los posibles efectos de esta binariedad en

la pérdida de masa y en la forma de la envoltente circunestelar de V Hydrae. Para llevar acabo los objetivos mencionados, se analizaron datos interferométricos de V Hydrae en las bandas L , M y N en el infrarrojo medio. Estos datos fueron tomados con el instrumento MATISSE del VLTI (Ver Cap. 2 para una explicación del instrumento). Como coautor de este artículo, he tenido la oprtunidad de revisar el draft y las siguientes revisiones del referee y darle a Léa sugerencias para mejorar la discusión.

Proceedings

1. Compressed sensing for infrared interferometric imaging

Joel Sanchez-Bermudez, **A. Rosales-Guzmán**, Héctor Morales, Antxon Alberdi, Anand Sivaramakrishnan, Rainer Schödel, and Jörg-Uwe Pott

Publicado en 2020 (Proceedings Volume 11446, Optical and Infrared Interferometry and Imaging VII; 114461O)

En este proceeding, liderado por Joel Sánchez, se explora la técnica de compressed sensing para la reconstrucción de imágenes utilizando datos interferométricos tomados con el telescopio James Webb. Como coautor de este trabajo, obtuve las observables interferométricas y realicé las gráficas que se presentan a lo largo del escrito.

Contents

List of Figures	XVII
List of Tables	XIX
List of Acronyms	XXIII
Motivation and outlook of this thesis	1
1 AGB stars	5
1.1 Evolution from the MS to the early-AGB phase at $M = 1 M_{\odot}$	6
1.2 Evolution in the AGB phase	9
1.2.1 Stellar Variability	11
1.3 Mass loss during the AGB phase	15
1.3.1 Early indications of mass loss	15
1.3.2 Mass loss from a theoretical point of view	16
1.3.3 The role of convection in the mass-loss processes	21
2 Interferometry	31
2.1 Principles of interferometry	31
2.1.1 Visibility amplitude	33
2.1.2 Visibility phase	34
2.1.3 The effect of the atmosphere on the interferometric observations	35
2.2 Interferometric facilities around the World	39
2.2.1 CHARA	40
2.2.2 VLTI	40
2.3 Image reconstruction in optical interferometry	45
2.3.1 BSMEM	47

2.3.2	SQUEEZE	47
2.4	Studies of AGB stars through IR interferometric observations	49
2.4.1	Model fitting	50
2.4.2	Image reconstruction	50
2.4.3	Model Atmospheres	50
2.4.4	Radiative transfer modeling	51
2.4.5	The importance of observational evidence	51
3	Interferometric analysis of the M-type Mira star R Car with PIONIER-VLTI	57
3.1	Our source: R Car	57
3.2	Introduction to the problem of convection in AGB stars	59
3.3	Observations and data reduction	60
3.4	Analysis and results	61
3.4.1	Diameter estimation: parametric uniform-disk model	61
3.4.2	Asymmetries in the stellar disk: regularized image reconstruction	64
3.4.3	Power spectrum analysis	65
3.5	Discussion	68
3.5.1	Sizes of the stellar disk and of the surface structures	68
3.5.2	Convective pattern size(s) and their correlation with the stellar parameters	69
3.6	Appendix: Additional figures	72
4	Interferometric analysis of the M-type Mira star R Car with GRAVITY-VLTI	75
4.1	The problem of dust and wind formation in AGB stars	75
4.2	Observations and data reduction	78
4.2.1	GRAVITY observations and interferometric data reduction	78
4.2.2	GRAVITY spectrum calibration	78
4.3	Analysis and results	81
4.3.1	Geometrical model	81
4.3.2	Spherically thin layer: MOLsphere model	85
4.3.3	Image reconstruction	88
4.3.4	Pure-line CO images	96

4.4	Discussion	98
4.4.1	CO column densities from the single-layer model	98
4.4.2	Observational restrictions to the wind driving candidates for M-type Mira stars	99
4.4.3	The role of CO asymmetries on mass-loss estimates	102
4.5	Appendix: Additional figures	103
5	Conclusions and future work	111
5.1	Future work	115
5.2	Prospects for the following decade: the ngVLA	119
5.3	Closing remarks	121
A	Python codes	123

List of Figures

1.1	Overview of an AGB star	6
1.2	Evolution of a $1 M_{\odot}$ star	8
1.3	Examples of AGB stars with their CSE	10
1.4	The light curve of α Ceti	12
1.5	Curves of constant condensation distance as a function of the power law coefficient and the value of the condensation temperature	20
1.6	Best-reconstructed images of the stellar surface of the S-type AGB star π^1 Gru	23
1.7	Characteristic granule size of the convection cells in π^1 Gru	24
1.8	An illustration of the movement of a convective blob across the medium	27
2.1	Fringe pattern on a detector's screen	33
2.2	Example of a $u-v$ plane achievable with GRAVITY using three Telescope arrays	34
2.3	Comparison between single-dish and interferometric observables for two objects with different sizes.	35
2.4	Simulated images of three models with their corresponding visibility curves	36
2.5	Visibility curves of two binary systems	37
2.6	An illustration to define the closure phases	38
2.7	Footprints of modern O/IR interferometers	39
2.8	The CHARA array and its instruments	41
2.9	The Paranal Observatory	42
2.10	The three second-generation instruments at the VLTI	46

2.11	Reconstruction of the interferometric imaging contest data set of 2004. . .	50
2.12	Overview of the number of AGB stars studied with interferometric high-resolution observations	53
3.1	Visual light curves of R Car for our 2014 and 2020 data	64
3.2	PIONIER u-v coverages for our 2014 and 2020 data	65
3.3	Best reconstructed images for our 2014 and 2020 datasets	66
3.4	Radial averaged power spectra of the reconstructed images	67
3.5	Logarithmic scale of the convective patterns (x_g) versus effective temperature (T_{eff})	72
3.6	Comparison between the observables extracted from the 2014 mean reconstructed image and the data	73
3.7	Comparison between the observables extracted from the 2020 mean reconstructed image and the data	73
4.1	Visual light curve of R Car for our 2018 data	80
4.2	R Car calibrated spectra and V^2	81
4.3	GRAVITY calibrated interferometric observables	83
4.4	Best-fit UD models for the V^2 in the pseudo-continuum versus spatial frequencies for both epochs.	84
4.5	Best-fit Θ_{UD} as a function of wavelength for the two analyzed epochs . . .	85
4.6	Illustration of single-layer model	86
4.7	Best fit to spectra with the single-layer model for the two CO band heads and the two epochs	87
4.8	Best fit to V^2 from the best single-layer models across the first CO band head for our two epochs.	88
4.9	Best fit to V^2 from the best single-layer models across the second CO band head for our two epochs.	89
4.10	Best pseudo-continuum reconstructed images for the January and February epochs	92
4.11	Best reconstructed images per spectral channel for the January and February epochs across the first CO band head	93
4.12	Best reconstructed images per spectral channel for the January and February epochs across the second CO band head.	94

4.17	Pure-line CO images of the first CO band head for the January and February epochs	98
4.13	Principal components at the first CO band head for the January and February epochs	104
4.14	Principal components for the January and February epochs at the second CO band head	105
4.15	Representative example of CPs versus spatial frequencies of the data set that corresponds to the first CO band head	106
4.16	Two-dimensional photocenter offsets in mas	106
4.18	Condensation temperature as a function of the dust absorption coefficient for a constant levitation radius $R_l = 2.43 R_*$	107
4.19	Condensation temperature as a function of the dust absorption coefficient for a constant levitation radius obtained directly from the pure-line CO images	107
4.20	Fit to observed V^2 and CPs corresponding to the best reconstructed images across the pseudo-continuum for the January and February epochs	108
4.21	Fit to observed V^2 and CPs from the best reconstructed images across the first CO band head for the January and February epochs	109
4.22	Fit to observed V^2 and CPs from the best reconstructed images across the second CO band head for the January and February epochs.	110
5.1	ISO-SWS spectra of three AGB stars	115
5.2	The typical spectrum of an AGB star in the infrared from 0.5 to 25 μm	116
5.3	Calibrated V^2 and CPs of R Car in the L -band (3.0 - 4.0 μm) as a function of the spatial frequency	118
5.4	Calibrated V^2 and CPs of R Car in the M band (4.1 - 4.7 μm) as a function of the spatial frequency	118
5.5	Reconstruction tests performed on simulated data to test the capabilities of the ngVLA	120
5.6	uv-coverage of the simulated ngVLA observations	121

List of Tables

1.1	Early Discoveries of Intrinsic Stellar Variables	13
2.1	Angular resolution of telescopes with different diameters for three different band-passes	31
2.2	High-resolution observations of AGB stars	54
2.3	High-resolution observations of AGB stars (Continued)	55
3.1	Fundamental astrophysical parameters of R Car	59
3.2	Log of the observations for the 2014 interferometric data	62
3.3	Log of the observations for the 2020 interferometric data	63
3.4	Logarithm of the characteristic size of the patterns observed on the surface R Car.	71
4.1	Log of the observations for our GRAVITY R Car data	79
4.2	Best-fit parameters of the uniform disk geometrical model.	82
4.3	Parameters of the single-layer model for the two CO band heads and our two epochs.	90
4.4	Parameters of the single-layer model for other AGBs.	100

List of Acronyms

AAVSO American Association of Variable Star Observers

AFGL Air Force Geophysics Laboratory

AGB asymptotic giant branch

AGN active galactic nuclei

ALMA Atacama Large Millimeter/submillimeter Array

ATs Auxiliary Telescopes

AU Astronomical Unit

BCD Beam Commuting Device

BSMEM BiSpectrum Maximum Entropy Method

CEV Cumulative Explained Variance

CHARA Center for High Angular Resolution Astronomy

CP Closure Phase

CSE circumstellar envelope

DIT Detector Integration Time

E-ELT European Extremely Large Telescope

ESO European Southern Observatory

FITS Flexible Image Transport System

FWHM Full Width Half Maximum

HBB hot-bottom-burning

HR Hertzsprung–Russell

IR infrared

IRAM Institut de Radioastronomie Millimétrique

ISM Interstellar medium

JMMC Jean-Marie Mariotti Center

LPV Long Period Variables

mas milliarcseconds

MATISSE Multi AperTure mid-Infrared SpectroScopic Experiment

MCMC Markov Chain Monte Carlo

MIR mid infrared

MLT Mixing length theory

MS Main Sequence

NDIT Number of Detector InTegrations

ngVLA next-generation Very Large Array

NIR near infrared

OPD optical path difference

PIONIER Precision Integrated Optics Near Infrared ExpeRiment

PNe Planetary nebulae

RGB red giant branch

RSG red super giant

SED Spectral Energy Distribution

TMSS Two-Micron Sky Survey

UTs Unit Telescopes

VLA Karl G. Jansky Very Large Array

VLTI Very Large Telescope Interferometer

WDs white dwarfs

Motivation and outlook of this thesis

Although asymptotic giant branch stars are among the main contributors to the enrichment of the interstellar medium, our understanding of the processes that lead to the formation of winds and the subsequent mass loss is still limited. While current theoretical models have provided us with many insights of processes such as convection or wind formation in these stars, observational evidence to test these models is still scarce.

One of the main reasons for this is the angular resolution required to characterize phenomena such as those mentioned above, which occur in the regions closest to the stellar surface. This is where interferometry becomes a crucial tool to provide the observational evidence needed to improve our understanding of these astrophysical sources. We will see in the following chapters that interferometric studies of asymptotic giant branch stars are not very abundant, but each study offers different results that allow us to increasingly understand the processes taking place in these objects with better detail.

Motivated by the lack of observational evidence to confront the abundant mass-loss and convection models, this thesis focuses on the study of asymptotic giant branch stars using infrared interferometry. More specifically, I present a detailed analysis of the innermost regions ($1-3 R_*$) of the M-type Mira star R Car using interferometric data obtained with the Precision Integrated Optics Near Infrared ExpeRiment and GRAVITY instruments of the Very Large Telescope Interferometer in the H ($1.6 - 1.99 \mu\text{m}$) and K ($2.0 - 2.4 \mu\text{m}$) bands in the near infrared. The analysis of these data cover different wavelengths (multi-band analysis) and also different phases of the pulsation cycle of the star (multi-epoch analysis).

This thesis is structured as follows: In Chapter 1, I present an introduction about asymptotic giant branch stars in general and then I move to more specific topics: convection and the first interactions that lead to the subsequent mass loss in these types of stars. In Chapter 2 I introduce the basic concepts of infrared interferometry; the most common techniques used to interpret interferometric data; and the facilities around the world that can provide these kind of observations. Both chapters are aimed also to emphasize the need for high-angular resolution observations to shed light into the complex phenomena occurring in the innermost regions of asymptotic giant branch stars.

In Chapter 3, I introduce the M-type Mira star R Car, which is the subject of study in my thesis, then, I present an analysis of its surface using interferometric data in the H band, obtained with the instrument Precision Integrated Optics Near Infrared ExpeRiment of the Very Large Telescope Interferometer. The quality of these data and the angular resolution achieved, allowed us to detect bright structures on the surface of the star, whose size and position change over time. We compared these results with extrapolations from various convection models developed for different types of stars. Although specific convection models for asymptotic giant branch stars are absent, it is not entirely incorrect to think that the processes governing convection should be similar across all stars along the Hertzsprung–Russell diagram. Our results suggest that the observed bright structures on the surface of R Car are consistent with extrapolated sizes, potentially associated with convective cells. This observational evidence enhances our understanding of convection models, which, again, currently lack observational support despite their abundance.

The most widely accepted mechanism for mass loss in the asymptotic giant branch phase involves a two-step process: (i) stellar pulsations elevate gas to a distance where dust can begin to condense, and (ii) stellar radiation accelerates the gas and dust, allowing them to escape the gravitational potential. While this scheme works, an aspect not fully understood is the efficiency of different dust grains in transporting radiation, either through absorption or scattering. Shedding light on this issue requires the observation of gas layers closest to the stellar surface. In addition to high angular resolution, a spectral window with dust transparency is essential. This requirement is met in M-type asymptotic giant branch stars by observing in the K band. Hence, in Chapter 4 we characterize the gas layers closest to the stellar surface of R Car in this band during two separate epochs spaced approximately 1 month apart.

The importance of this study lies in the fact that the physical conditions of temperature and density in which the gas, primarily CO, is found, are consistent with the regions where the dust originates, giving rise to winds and mass loss in such stars. With the analysis of these data, we found that the distribution of the gaseous layers surrounding the star is asymmetric and undergoes shape variations over short periods. By successfully estimating the temperature, size, and density of the innermost gas layers, we were able to determine some types of dust grains as wind-drivers for M-type asymptotic giant branch stars.

Finally, in Chapter 5, I present the conclusions and future work, which includes the ongoing analysis of interferometric data for R Car in the L , M , and N bands in the mid infrared. This study aims to detect and characterize the innermost dusty layers around the star. I close this chapter presenting the future of interferometry for the next decade with the construction of the next-generation Very Large Array and the subsequent enhancements to the Very Large Telescope Interferometer.

AGB stars

This chapter gives an introduction to the asymptotic giant branch (AGB) phase, the different types of AGB stars, and their different mass-loss mechanisms. The contents in this chapter are based principally on the book by [Habing & Olofsson \(2013\)](#), on the review by [Höfner & Olofsson \(2018\)](#), and the article by [Bladh & Höfner \(2012\)](#). Other references will be cited throughout the chapter.

The AGB phase constitutes one of the the final stages in the life cycle of stars characterized by low-to-intermediate masses within the range of $0.5 - 8 M_{\odot}$. Following their departure from the Main Sequence (MS), these stars undergo an initial red giant branch (RGB) phase, transitioning from the subsequent central He-burning stage to harbor an inert C-O core where eventually the electron-degeneracy pressure dominates. At this stage, nuclear burning within the stellar core ceases to occur. Subsequently, the stars move through a second RSG phase, denoted as the AGB phase, sustained by the alternating burning of H and He in thin shells around the inert C-O core. This marks the concluding phase in their evolutionary trajectory before they transform into Planetary nebulae (PNe) and then white dwarfs (WDs).

An AGB star comprises distinct components: *(i)* a compact, very hot, and dense core, *(ii)* a large, hot, and comparatively less dense stellar envelope, *(iii)* a rarified, warm atmosphere, and *(iv)* a very large, extremely diluted, and cool circumstellar envelope (CSE) (see Fig. 1.1). So, the size scales span over more than 10 orders of magnitude, the density encompasses 30 orders of magnitude, and the temperature spans 7 orders of magnitude. To fully grasp the AGB star's evolution, it is crucial to explore the intricate dynamics of the diverse physical and chemical processes unfolding in its various segments. The following sections offer an exploration of the processes taking place as a $1 M_{\odot}$ star

embarks from its MS to the AGB phase. This discussion aims to elucidate fundamental attributes of such stars, shedding light on their preceding evolutionary stages.

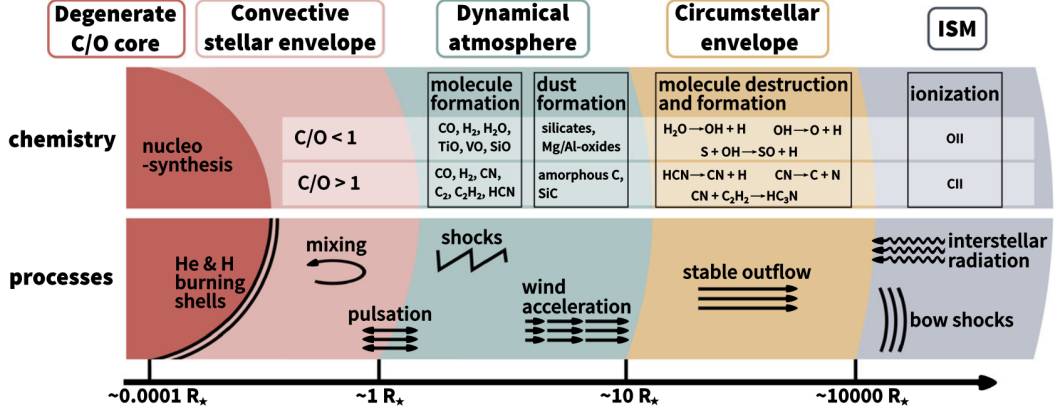


Figure 1.1: Overview of an AGB star (not drawn to scale). Some important physical/chemical processes are indicated. Image taken from Höfner & Olofsson (2018).

1.1 Evolution from the MS to the early-AGB phase at $M = 1 M_{\odot}$

The important features and schematic evolution of a $1 M_{\odot}$ star are presented in Fig. 1.2. For an easy identification in the figure, those features are indicated with numbers from 1 to 15. I will refer to these points along the section.

The initial stage in the life of a newly formed $1 M_{\odot}$ star is characterized by the onset of nuclear reactions in the core, marking the *main sequence*. During this phase, the only source of stellar energy is the burning of H in the core. The star's structure undergoes modifications primarily due to alterations in its chemical composition resulting from nuclear reactions. This phase has a duration of 10^9 years, constituting the longest part of the star's life and represents a stable period where the star maintains a balance between the gravitational force pulling it inward and the outward pressure generated by H fusion in the core.

As the amount of H in the core decreases, the star will slowly move upwards in the HR diagram, almost along the main sequence (points 1-4). The corresponding H abundance profiles are shown in inset (a) of Fig. 1.2. The star will experiment slight increases in brightness and temperature, with a relatively stable radius. Then, it will

1.1. EVOLUTION FROM THE MS TO THE EARLY-AGB PHASE AT $M = 1 M_{\odot}$ 7

move to the right in the HR diagram, as H in the core nears its end. Eventually, the core is almost pure degenerated He. H will continue to burn in a thick shell around the core. Inset (b) shows the advance of the H-burning shell during this evolution.

After the H exhaustion at the core, the star transitions from the main sequence to a state in which H starts burning in a shell surrounding the He-core, causing the core's mass to increase. As a consequence, the envelope of the star expands, moving it to the right in the HR diagram (points 5-7). Upon reaching the Hayashi limit (about point 7), convection extends inward (in mass) from the surface, and the convective envelope penetrates into the region where partial H burning has occurred in earlier evolution (see inset (c)). This phenomenon is known as *first dredge-up* and it enriches the surface with ^4He and products of CN (primarily ^{14}N and ^{13}C), which are mixed to the surface (point 8). The growing core eventually becomes degenerate, leading to a rise in temperature as the star ascends the giant branch until it reaches 100 million K, which is enough for He to burn into C in the triple-alpha process. Inset (d) shows how neutrino losses from the center cause the temperature maximum to move outward.

The He burning begins across the central region, causing a sudden temperature increase. Since the degenerate core cannot expand as a response to the temperature increase, the rate of nuclear reactions accelerates instead. At some point, the increasing temperature will remove the degeneracy of the gas in the core, and a violent expansion will occur. Shortly after the He ignition, an explosion occurs: the *He-core flash* or *He-flash* (point 9).

Post-He flash, the star moves to the horizontal branch, burning ^4He in a convective core and H in a shell (10-13). The position on the horizontal branch depends on the envelope mass, which is influenced by mass loss during the He-flash. While the luminosity does not vary much along the horizontal branch, the effective temperatures are higher for stars with less mass in the envelope.

After the He exhaustion (point 14) the star will ascend the giant branch for the second time. In the degenerated core there are two energy sources: (i) The He-burning shell above the C-O core and (ii) the H-burning shell above the He-shell. A deep convective shell is located above both the H and He shells.

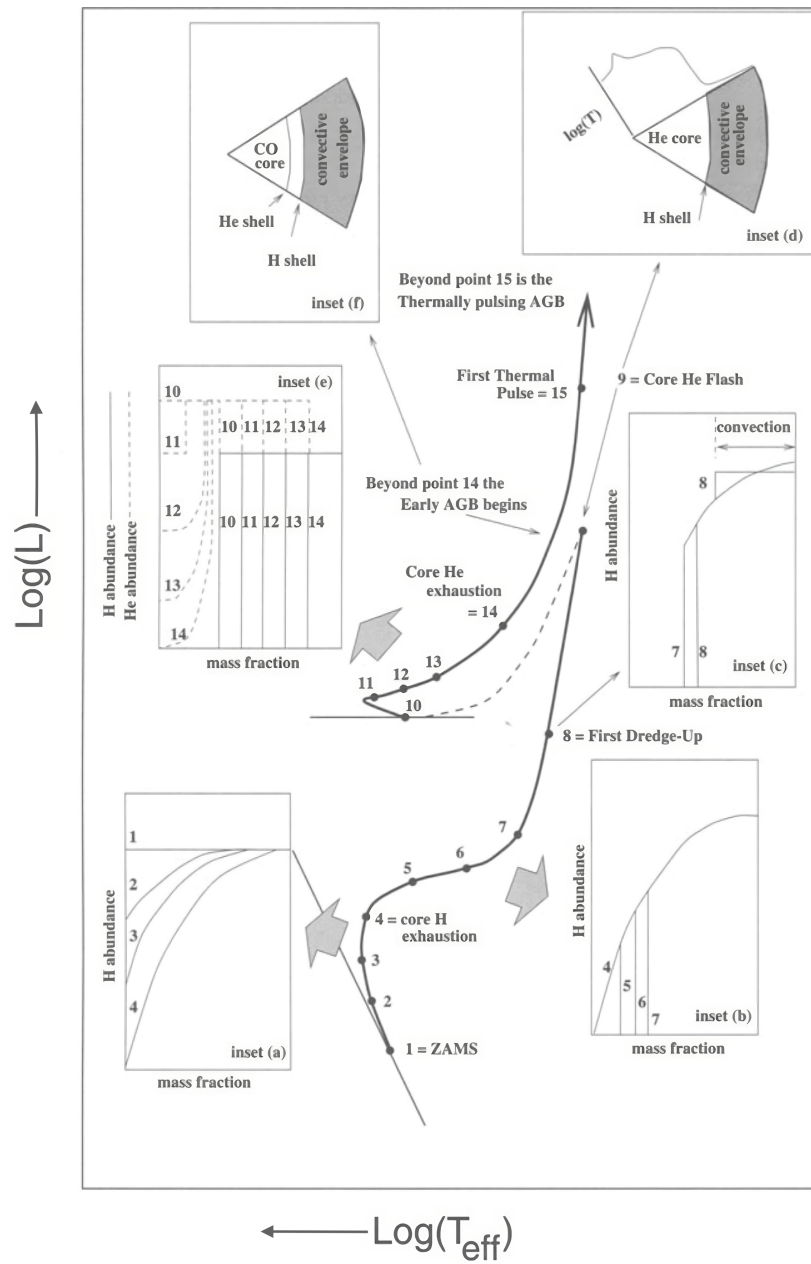


Figure 1.2: Schematic evolution of a $1 M_{\odot}$ star. Image taken from [Habing & Olofsson \(2013\)](#).

1.2 Evolution in the AGB phase

The core and stellar envelope: Following the conversion of He in the core into C and O, the He-burning zone shifts outward, causing the C-O core to contract to a size of approximately 10^3 km and a temperature of 10^8 K, akin to the characteristics of a white dwarf. This core contraction, coupled with the expansion of the envelope, results in a rapid increase in luminosity, marking the onset of the *E-AGB* (early asymptotic giant branch) phase. During this phase, He-burning in a shell becomes the primary source of energy. The stellar envelope expands to about 10^8 km, and the surface temperature is around 3000 K. At a certain point in the early evolution, the envelope becomes pulsationally unstable, exhibiting a characteristic time scale on the order of a hundred days (see Sec. 1.2.1).

Double-shell burning and thermal pulses: When a star reaches the luminosity of approximately the tip of the RGB, denoted by $M_{\text{bol}} = -4$ mag or $3000 L_{\odot}$, a new phase starts. The star becomes capable of burning both He and H in shells. Periodically, the thin He-layer surrounding the core undergoes rapid burning into C, which is primarily added to the core's mass. This brief episode, known as a *thermal pulse* or *He-shell flash* (point 15), induces a moderate luminosity modulation in the star. In the intervals between thermal pulses, the star resumes burning H. This intermittent phase of He and H burning is called the *TP-AGB phase*.

The dredge-up: During a thermal pulse, convection reaches layers undergoing nuclear processing, transporting enriched material to the stellar surface. This process results in the accumulation of products from nuclear burning, particularly "new" C. In some cases, this enrichment persists, causing the C abundance to surpass that of O. Consequently, the atmosphere undergoes a transition from O-rich (with $C/O \sim 0.5$, also known as M-type AGB stars) to C-rich conditions ($C/O > 1$, also known as C-type AGB stars)¹. This represents the second significant dredge-up for a low-mass star and the third for an intermediate-mass star. However, in certain cases, this transition is prevented by the hot-bottom-burning (HBB), particularly for AGB stars with initial masses above a specific limit (around $\sim 4 M_{\odot}$ for solar composition, less at lower metallicity). The HBB inhibits the formation of C stars by causing CNO-burning to destroy C produced

¹This transition may involve the formation of S-stars, covering spectral types MS, S, SC, with $0.5 \leq C/O \leq 1$ (Höfner & Olofsson 2018).

during He-burning, transforming it into N. Consequently, the most massive AGB stars are expected to retain their M-type classification throughout their evolution.

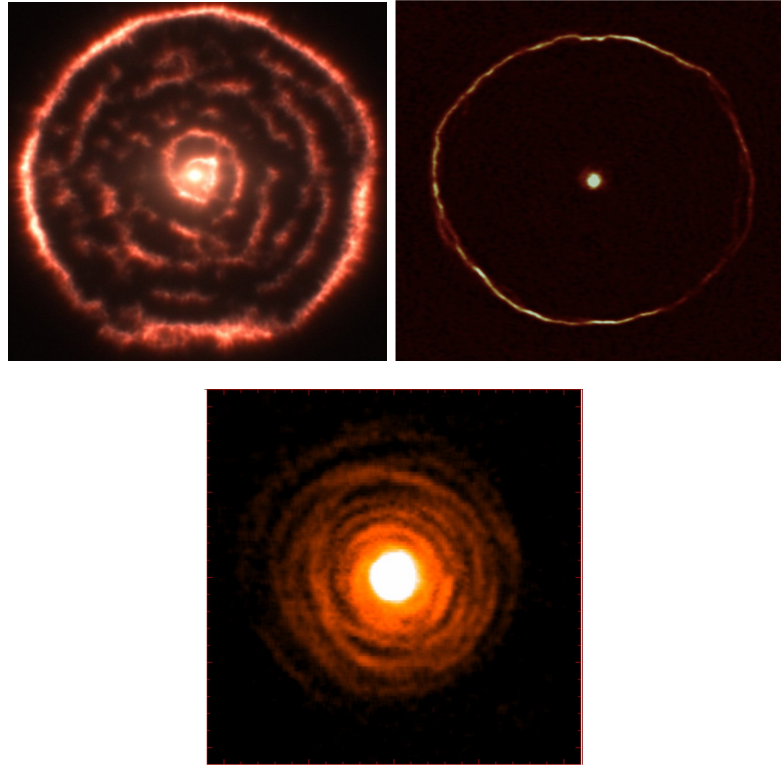


Figure 1.3: Examples of the CSE for different AGB stars. Top-left panel: Image of R Scl (Maercker et al. 2012), top-right panel: Image of U Ant (Kerschbaum et al. 2017). Both images were obtained with the Atacama Large Millimeter/submillimeter Array (ALMA). Bottom panel: Image of IRC+10216, obtained with the Institut de Radioastronomie Millimétrique (IRAM) 30 m telescope (Cernicharo et al. 2015). The different fields of view of these images range from 100 to 200 arcsec.

The atmosphere: The outer regions of the stellar envelope reach temperatures low enough to facilitate the formation of molecules, and their presence significantly influences the spectral characteristics of stars. This influence can vary considerably, particularly between C-type and M-type stars, at least within the near infrared (NIR) range. Additionally, the structure of the stellar atmosphere is affected to some extent. Pulsations of the star deposit mechanical energy into the weakly bound outer regions, causing the atmosphere to extend significantly beyond what a hydrostatic model would

predict. This extension leads to the development of shocks, and at sufficiently high altitudes, grain condensation occurs in the post-shock gas.

The CSE: An AGB star will eventually lose mass at a considerable rate in the form of a slow ($\sim 15 \text{ km s}^{-1}$) wind, and this forms a CSE of escaping gas and particles. The gas is to a large extent molecular with H_2 dominating. The molecules are located in envelopes of different sizes (being CO and H_2 the largest ones by far), or shells of different radii and widths, depending on their resistance to UV photons and their formation routes (see Fig. 1.3 for examples of AGB stars with CSE). The dust grains survive much further from the star than do the molecules. The molecular setup, as well as the grain properties, are a strong function of the C/O ratio. At some point, the CSE merges into the surrounding Interstellar medium (ISM). In this region the temperature is below 10 K, and the particle density is less than 10 cm^{-3} . This may occur at a distance of 10^{13} km or more from the star, and it defines the outer limit of the AGB star.

Termination of the AGB: Ultimately, the rate of ejection of the matter is higher than the growth rate of the core, and from this point on, the mass-loss process (see Sec. 1.3) determines the evolution. Eventually, all the matter around the core is dispersed into space, and this marks the endpoint of AGB evolution, and the beginning of the post-AGB evolution. In practice, this starts when the stellar envelope mass becomes less than about $0.01 M_{\odot}$. For a very short time (on the order of a few thousand years) the star becomes a *post-AGB star*, and then, for a time of a few tens of thousands of years, it becomes a Planetary Nebula. The nebula is expanding rapidly; it fades, and only the stellar core remains as a WD. Figure 1.1 shows a schematic view of the different parts of an AGB with the information of relevant processes occurring.

1.2.1 Stellar Variability

In the previous Section, I mentioned that at some point during the early evolution of an AGB star, its envelope becomes pulsationally unstable with a characteristic time scale on the order of hundred days. Here, I will describe how this variability was first observed and how this discovery influenced the posterior studies of stellar variability. Then, since the object of the study of this thesis is a Mira star, I will provide some characteristic properties of this kind of stars.

Like most astronomical discoveries, the first observations of stellar variability were

accidental. Fabricius² observed, in 1596, that the star *o* Ceti exhibited a range of variability from being invisible to reaching second magnitude (see Fig.1.4). As a tribute, he named the star *Mira*, meaning *the wonderful*. This discovery provided further evidence supporting the notion, advocated strongly by Tycho Brahe after the appearance of the *new star* in Cassiopeia in 1572, that the heavens are not static.

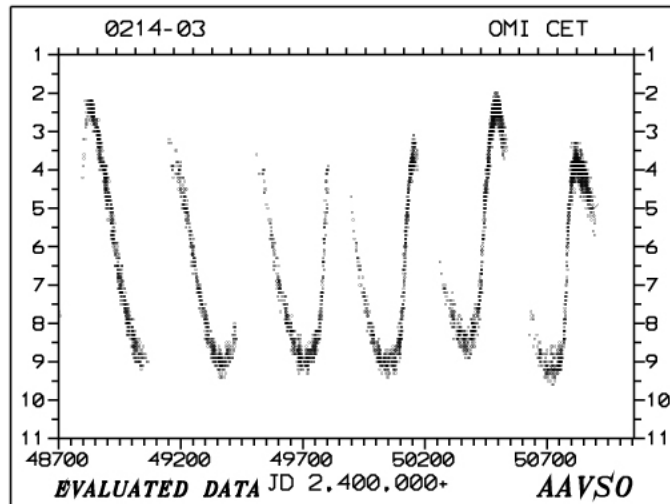


Figure 1.4: The visual light curve of *o* Ceti extracted from the American Association of Variable Star Observers (AAVSO) database.

A significant milestone occurred in the 18th century when Goodricke made a ground-breaking discovery. In 1782, he announced the variations of β Persei, also known as Algol. These variations were found to be periodic and stable. To explain these observations, Goodricke proposed a model of an eclipsing binary star system, where the stars are closely situated and unresolved. This was the first explanation for stellar variability and one that served as a stimulus to search for other binary star systems. The stimulus was such that, in 1784, Goodricke discovered the variability of δ Cephei (δ Cep), and in the same year, Piggot discovered the variability of η Aquilae (η Aql). Since the periods of these stars were found to be similar to that of Algol, a natural choice was to apply the eclipse model to explain their variability. Nowadays, both δ Cep and η Aql are

²David Fabricius (9 March 1564 – 7 May 1617) Born in Esens, Frisia (now Germany), he was a Lutheran pastor serving small communities in East Frisia, Germany. In addition to his pastoral duties he studied Astronomy. The study of sunspots, as well as the first variable star recorded by the modern Western world, are his two main notable contributions to the field of Astronomy

known to be pulsating variables unrelated to the Algol class of binaries, but the general explanation of the variations had to wait for more than 150 years after this discovery. To summarize, Table 1.1 shows a list of the earliest discoveries of what are now known to be intrinsically variable stars.

Star name	Discoverer	Year
ι Ceti	Fabricius	1596
ψ Leonis	Montanari	1667
κ Sagittarii	Halley	1676
χ Cygni	Kirch	1687
δ Cephei	Goodricke	1784
η Aquilae	Piggot	1784
R CrB	Piggot	1795
α Herculis	Wm. Herschel	1796

Table 1.1: Early Discoveries of Intrinsic Stellar Variables. Table adapted from (Shore 2003).

During the next century, the search for stellar variability grew in importance for Astronomy. The work of Argelander at Bamberg, the establishment of the *Bonner Durchmusterung* star atlas and the international efforts to construct the *Carte du Ciel*, a photographic all-sky atlas, motivated the discovery and cataloging of variable stars.

The most important discovery made during the 19th Century was connected with observations of variable stars in the Large and Small Magellanic Clouds, with most of the work being performed at Harvard by H. Levitt. Around 1905, she realized that these stars were generally of some type as the variable δ Cephei. The extraordinary discovery was the relationship between the period and the apparent brightness of the stars, the so-called period-luminosity relation.

Together with the observational discoveries, theoretical work on the cause of variability continued. Eddington suggested the pulsation model for stellar variability and derived the linearized, adiabatic pulsation equation (see Eddington 1918, 1919). Subsequent works by Cowling (1934) and Rosseland (1949) further clarified the instabilities. This epoch culminated with the encyclopedic review article by Ledoux & Walraven

(1958), which still serves as an important reference for all discussions of stellar variability.

Cox (1963) highlighted the importance of stellar convection zones in driving pulsation and producing the radial velocity variations in Cepheids. The first machine simulations of nonlinear, nonadiabatic pulsation models were accomplished in the mid-1960s. Around the same time, the first large-scale grids of stellar interior models were produced. Schwarzschild & Härm (1965) discovered the thermal instability of double shell sources.

Mira stars

As one may suspect at this time, intrinsic stellar variability can be found in all types of stars, from the MS to the RGB phase; even WDs have variability. Depending on the nature of the pulsations, the stars can be classified between radial and non-radial pulsators. Each category has sub-categories defined according to pulsation periods, luminosities, temperatures, etc. In the category of radial pulsators exist the Long Period Variables (LPV) with pulsation periods between 100 - 1000 days. Mira variables fall in this sub-category. Named after the discovery of *o* Ceti, Miras are emission-line cool giants generically arising from a population of low to intermediate mass ($1 - 2 M_{\odot}$) stars. Miras typically have luminosities around $10^3 L_{\odot}$ and temperatures less than 4000 K. These stars have some of the largest visual amplitudes observed among pulsating variables, ranging from 2.5 up to 11 mag, but generally considerably smaller in the infrared (at a wavelength of few microns, the amplitude is less than one magnitude). The periods range between 80 and 1000 days, although many of the longest period systems are quite irregular in their light curve behavior.

Miras are perhaps the best-studied examples of non-linear pulsators, having amplitudes large enough to produce the ejection of matter and non-adiabatic behavior of the envelopes. One interesting aspect of these stars is that their pulsation periods are sufficiently long, and their amplitudes large enough, that time-dependent convection may be important in modeling their internal structure. It is worth noting that considerable theoretical attention is currently being paid to these stars (see e.g, Chiavassa et al. 2024; Rees et al. 2024).

1.3 Mass loss during the AGB phase

I mentioned in previous sections that during the AGB phase the stars will lose most of their mass in the form of a slow and dense wind. As a consequence, all the processed material will be returned to the ISM, contributing to its enrichment. Understanding the wind formation and mass loss mechanisms in AGB stars is then of prime importance to study the cycle of matter in the Universe. In this section, I will describe our current knowledge of the mass-loss processes that take place during the AGB phase.

1.3.1 Early indications of mass loss

The first evidence of (substantial) post-main-sequence mass loss came through observations of the binary system α Her by [Deutsch \(1956\)](#). Circumstellar absorption lines were seen in the spectrum of the companion star, suggesting circumstellar gas as far away as $10^5 R_{\odot}$ from the giant. With an estimated outflow velocity of 10 km s^{-1} , the gas velocity is well above the escape velocity at this point. The estimated mass-loss rate was $3 \times 10^{-8} M_{\odot} \text{ yr}^{-1}$. In a study of similar systems, [Reimers \(1975\)](#) derived an empirical relation between mass-loss rate and stellar parameters (luminosity, mass, and radius; Eq. 1.1) that bears his name:

$$\frac{dM}{dt} = 4 \times 10^{-13} \frac{(L/L_{\odot})(R/R_{\odot})}{(M/M_{\odot})} M_{\odot} \text{ yr}^{-1}, \quad (1.1)$$

where L is the luminosity, M the mass, and R the stellar radius.

There were also indirect indications. [Auer & Woolf \(1965\)](#) found that the Hyades cluster contains about a dozen WDs; each one must have a mass below the Chandrasekhar limit of $1.4 M_{\odot}$. But, the Hyades cluster has stars with a mass of $2 M_{\odot}$ that are still on the MS. Consequently, the WDs progenitors must have lost at least $0.6 M_{\odot}$ during their post-MS evolution. The advent of infrared observations led to considerable progress, e.g., the Two-Micron Sky Survey (TMSS) by [Neugebauer & Leighton \(1969\)](#) and the Air Force Geophysics Laboratory (AFGL) catalog of [Price & Walker \(1976\)](#).

It was shown that late M-giants often have an excess of radiation at infrared wavelengths, an effect of dust in a CSE. In some objects, the dust optical depth is so high that most of the stellar energy is emitted at wavelengths longer than $2 \mu\text{m}$. [Gillett et al. \(1968\)](#) and [Woolf & Ney \(1969\)](#) attributed an emission band around $10 \mu\text{m}$ to small silicate particles and [Gehrz & Woolf \(1971\)](#) estimated circumstellar dust masses

and mass-loss rates of M giants. Similar results were found for Carbon stars (Woolf & Ney 1969). The appearance of different dust compositions around M- and C-type giants was explained by Gilman (1969) to be a consequence of the high binding energy of the CO molecule, which prevents the less abundant of the two elements from forming other molecules and solids.

Wickramasinghe et al. (1966) showed that light pressure on graphite grains can push both the grains and the surrounding gas out of the stellar gravitational field due to momentum transfer between dust and gas. Circumstellar OH (in maser emission) was first detected in 1968 (Wilson & Barrett 1968), and circumstellar CO rotational lines were observed a few years later towards the carbon star IRC+10216 (CW Leo) (Solomon et al. 1971). The first detailed physical/chemical model of a CSE was presented by Goldreich & Scoville (1976). The OH masers were explained as due to infrared pumping of OH molecules in a shell where they formed through the dissociation of H₂O by the interstellar radiation field.

In the decades following these early findings, significant progress has been made thanks to both space- and ground-based instrumentation (see e.g., Höfner & Olofsson 2018). These developments have enabled the study of spectral energy distributions with a wide wavelength coverage, high spectral resolution data on circumstellar atomic/molecular lines, and structural information on CSEs via interferometry of nearby objects, complemented by large-scale surveys and photometric monitoring of large samples of stars. In recent years, high-angular resolution techniques, covering wavelengths from the visual to the radio regime, have started to give direct insights into the dynamical atmospheres and wind acceleration regions of AGB stars which is essential for understanding the mass-loss mechanisms.

1.3.2 Mass loss from a theoretical point of view

Given the high luminosities of AGB stars, it is intuitive to consider radiation pressure as a driving force for their winds. To initiate a wind, the outward force exerted by radiation must surpass the inward force from gravitational potential. Radiative acceleration, involving the transfer of momentum from photons to matter through absorption and scattering, depends critically on the total radiative cross section per mass of stellar material. Estimating the required opacity to initiate a stellar wind via radiative pressure involves comparing the strength of radiative acceleration relative to the inward gravi-

tational acceleration acting on a material layer. This comparison can be expressed as follows:

$$\frac{a_{\text{rad}}}{a_{\text{grav}}} = \frac{\langle \kappa \rangle L_*}{4\pi c G M_*}, \quad (1.2)$$

where $\langle \kappa \rangle$ is the flux mean opacity (total cross-section per unit mass), G is the gravitational constant, M_* and L_* are the mass and luminosity of the star in consideration, respectively. The previous equation defines three regimes; (i) where radiative acceleration dominates over gravitational attraction ($a_{\text{rad}}/a_{\text{grav}} > 1$), (ii) where gravitational attraction dominates over radiative acceleration ($a_{\text{rad}}/a_{\text{grav}} < 1$), and (iii) where both forces are equal in magnitude. This situation corresponds to a critical value of the flux-mean opacity, given by:

$$\langle \kappa \rangle_{\text{crit}} = \frac{4\pi c G M_*}{L_*} \approx 2.6 \left(\frac{M_*}{M_\odot} \right) \left(\frac{L_*}{5000 L_\odot} \right)^{-1} [\text{cm}^2 \text{g}^{-1}]. \quad (1.3)$$

It is worth noting that wind driving might be a cumulative process, which means that radiative pressure is acting on material that is temporarily moving upwards on a ballistic trajectory due to the effect of shock waves. In that case, a value of $a_{\text{rad}}/a_{\text{grav}}$ that is above one may be sufficient to lift material out of the potential well of the star. Nevertheless, $\langle \kappa \rangle_{\text{crit}}$ from Eq. 1.3 provides us with a good estimate for the flux-mean opacity required to drive and outflow.

The previous discussion raises one important question: What are the sources of opacity around AGB stars? In the atmospheres of cool giant stars, most of the gas is in molecular form, and certain species may condense into solid particles in the upper atmospheric layers. In principle, both gas and dust opacities contribute to the radiative pressure. In practice, however, the flux-mean opacity will be dominated by species that are more efficient at absorbing or scattering photons in the NIR wavelength region around the maximum stellar flux.

Opacity of molecules

The rich spectrum of vibro-rotational band heads³ from abundant molecules coincides with the stellar flux maximum in the NIR wavelength region, and their influence on ra-

³In the context of molecular spectroscopy, a vibro-rotational spectrum refers to the spectrum of a molecule that arises from its vibrational and rotational motion. In such spectra, a "band head" refers to the most intense or prominent peak within a spectral band.

diative pressure has been explored in the literature (see, e.g., [Jorgensen & Johnson 1992](#); [Elitzur et al. 1989](#)). Despite molecules playing a significant role in shaping the thermal structures of AGB stellar atmospheres, their collective flux-mean opacity remains insufficient to impact atmospheric and wind dynamics significantly (see, e.g., [Liljegren et al. 2016](#)). Hence, the observed mass loss rates in outflows cannot be solely attributed to molecules.

Opacity of dust grains

In contrast to molecules, dust grains are good candidates for driving winds of AGB stars, as they can be very efficient at absorbing and/or scattering the stellar photons, depending on their chemical composition and size. Certain materials, which are ingredients of circumstellar dust around AGB stars (e.g., amorphous carbon, or magnesium-iron silicates) are also efficient absorbers in the NIR range around the stellar flux maximum. Moreover, if the abundance of dust particles with the right properties is large enough in the outer atmospheric layers, their collective opacity can easily exceed $\langle\kappa\rangle_{\text{crit}}$ and trigger an outflow.

Dust species that are commonly associated with wind driving (amorphous carbon or silicates) will typically condense at temperatures between 1000 - 1500 K, or below. We can estimate the temperature, $T_{\text{d}}(r)$, of such dust species as a function of the distance from the center of the star if we assume that (i) the condition of radiative equilibrium sets the grain temperature, (ii) the radiation field follows a Planck function corresponding to an effective temperature T_* , geometrically diluted with distance, and (iii) the grain absorption coefficient can be approximated with a power law of the form $\kappa_{\text{abs}} \propto \lambda^{-p}$ in the relevant wavelength region around the stellar flux maximum, where λ is the wavelength and p is a material-dependent constant (see, e.g., [Bladh & Höfner 2012](#), for an example of such fits). $T_{\text{d}}(r)$ is then given by:

$$T_{\text{d}}(r) \approx T_* \left(\frac{2r}{R_*} \right)^{-\frac{2}{4+p}}, \quad (1.4)$$

where R_* is the stellar radius. On the other hand, we can define R_c as the minimum distance at which dust grains of a given material can form (without evaporating due to radiative heating), i.e., where the grain temperature is equal to the dust condensation temperature of the material. According to Eq. 1.4, when setting $T_{\text{d}}(R_c) = T_c$ we obtain

for R_c :

$$\frac{R_c}{R_*} \approx 0.5 \left(\frac{T_c}{T_*} \right)^{-\frac{4+p}{2}}. \quad (1.5)$$

The absorption coefficient's wavelength dependence, denoted by the value of p , results in distinct reactions of various condensates to the proximity of a star. A grain material with a positive p tends to heat up when exposed to the stellar radiation field. It excels in absorbing radiation, being more effective in absorption than emission, consequently pushing the condensation distance farther away from the star. Conversely, a grain material with a negative p exhibits the opposite behavior. Therefore, the survivability of a particular grain type close to a star is dictated by the combination of its condensation temperature and the slope of the absorption coefficient, p . An example of this trend is shown by [Bladh & Höfner \(2012\)](#) (Fig. 1.5), where the authors plotted curves of constant condensation distances as a function of p and T_c using Eq. 1.5.

To gain more feeling about condensation distances, let's take two examples. For Fe-bearing silicates with a condensation temperature of 1100 K and $p \approx 2.3$, $R_c \approx 10 R_*$ for a star with a temperature of 2800 K. The corresponding value for Fe-free silicates ($T_c = 1100$ K, $p \approx -0.9$), present in the atmospheres of O-rich AGB stars, is $R_c \approx 2 R_*$ for a star with an effective temperature of 2800 K. As we see, for Fe-free silicates, the gas condenses into dust at $\sim 2 R_*$, but if the gas is initially located on the surface of the star, how does it reach these distances? What is the mechanism responsible for lifting the gas from the surface of the star beyond the condensation radius? The answer is: pulsation.

The most accepted theory establishes that when the stars pulsate, the induced shock waves levitate the gas in the atmosphere to a distance known as levitation distance R_l , which is defined as follows:

$$\frac{R_l}{R_*} = \frac{R_0}{R_*} \left[1 - \frac{R_0}{R_*} \left(\frac{u_0}{u_{\text{esc}}} \right)^2 \right]^{-1}, \quad (1.6)$$

where u_0 is the initial velocity of the gas at a distance, R_0 , and $u_{\text{esc}} = (2GM_*/R_*)^{1/2}$ is the escape velocity. The combination of pulsation-induced shock waves and radiation pressure on dust grains is the most promising mechanism to explain atmospheric levitation and wind driving. In this scenario, the mechanisms for driving dust differ depending on the dust properties. I will discuss these differences in the following section.

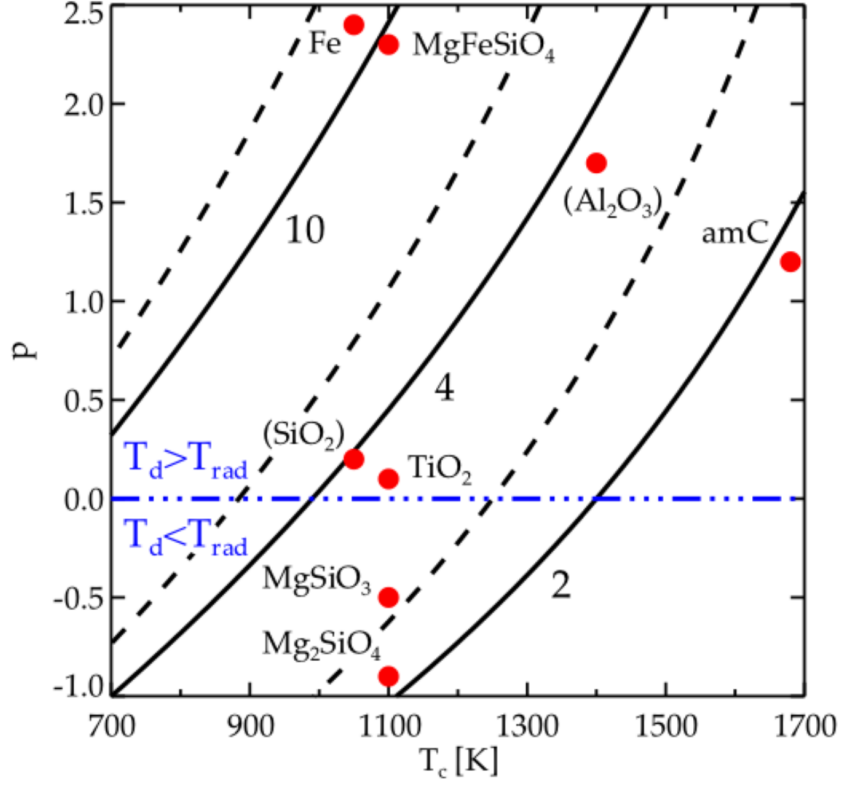


Figure 1.5: Curves of constant condensation distance ($R_c/R_* = 2, 4, \text{ and } 10$) as a function of the power law coefficient p and the value of the condensation temperature T_c , using Eq. 1.5 for two stars, one with $T_* = 2800$ K (solid lines) and the other with $T_* = 2500$ K (dashed lines). The filled red circles mark where the selected set of dust species are situated in the p/T_c -plane. The dust species in parenthesis have uncertain or interpolated optical data in the NIR. The blue dashed-dotted line marks a limit that indicates whether certain dust particles are more efficient at absorbing or emitting the radiation from the star. The image and its description were taken from (Bladh & Höfner 2012).

The mass loss scenario for C- and M-type AGB stars

Theoretical and observational studies support that C-type AGB stars form amorphous C grains with large opacities that can be accelerated by radiation pressure (see e.g., Gautschy-Loidl et al. 2004; Sacuto et al. 2011; Rau et al. 2015, 2017). The mass-loss rates, wind velocities, spectral energy distributions, and photometric variations resulting

from the time-dependent atmosphere and wind models are in good agreement with observations (see, e.g., [Nowotny et al. 2011, 2013](#); [Eriksson et al. 2014](#)). However, due to the strong absorption by C-dust, the stellar photospheres and their inner atmospheres may be severely obscured, making detailed comparisons with spatially resolved observations difficult ([Sacuto et al. 2011](#); [Wittkowski et al. 2017](#)).

For M-type AGB stars, the high chemical complexity around them makes identifying the dust grains driving the dusty winds more complex (see Fig. 1.1). [Höfner \(2008\)](#) suggested a scenario where the radiative pressure that triggers the outflows is caused by photon scattering on Fe-free silicate grains. These silicates are highly transparent at visual and NIR wavelengths, resulting in significantly less radiative heating and smaller condensation distances than for Fe-bearing silicates. In order to create sufficient radiative pressure by scattering, the grains need to be typically of a size comparable to the wavelengths where the stellar flux reaches its maximum, which means that the grain size has to be in the range 0.1 - 1 μm . Recent observational studies report the presence of dust grains with radii of about 0.1 - 0.5 μm in AGB stars at distances below 2 - 3 stellar radii (see, e.g., [Norris et al. 2012](#); [Ohnaka et al. 2016](#); [Ohnaka et al. 2017](#)). Despite these results, the evidence to support or discard these models is still scarce, and even when the theory agrees with these observations, more evidence is needed in order to better constrain the mass loss models of O-rich AGB stars in different environments.

1.3.3 The role of convection in the mass-loss processes

Convection is a complex process in stellar astrophysics with important physical implications, such as heat transfer, mixing, and generation of magnetic fields, but also in pulsation and winds on evolved stars (see, e.g., [Montargès et al. 2021](#); [Ohnaka et al. 2016](#); [Ohnaka et al. 2017](#)). These effects, in turn, significantly impact the structure and evolution of stars, particularly during the AGB phase ([Kupka 2004](#)). In fact, in the mass-loss scenario described in the previous section, non-stationary convective flows also contribute to the generation of the pulsation-induced shock waves responsible for lifting the gas beyond the condensation distance (Eq. 1.5). Furthermore, asymmetries observed in AGB stars and other evolved stars could be caused by the underlying irregular global convective flows even if they are not visible in the stellar surface ([Freytag et al. 2017](#)).

Given its importance, there is a necessity of increasing our current knowledge of stellar convection both from the theoretical and observational sides. The first source

in which the convection models are calibrated is our Sun. According to [Schwarzschild \(1975\)](#), the Sun has around 2 million convective cells on its surface with typical sizes around 1000 - 2000 km across. Extrapolating this result would imply that on the surface of giant and supergiant stars, there should be only a few large (several thousand larger than those of the Sun) convective cells.

Studying and characterizing stellar convection has its difficulties, both from theoretical and observational points of view. From the observational point of view, one of the main challenges of studying convection in evolved stars is that their atmosphere is composed of gas and dust, which obscures the surface and makes it challenging to observe the convective patterns ([Wittkowski et al. 2017](#)). Furthermore, the resolution of current telescopes is limited, which restricts our ability to observe small-scale features on the surface of stars. Nevertheless, with increasing angular resolution, interferometric measurements at IR wavelengths offer a significant advantage for observing the surface of evolved stars. In fact, [Paladini et al. \(2018\)](#) used the Precision Integrated Optics Near Infrared ExpeRiment (PIONIER) at the Very Large Telescope Interferometer (VLTI) to observe the surface of the AGB star π^1 Gru, and presented reconstructed images that reveal the presence of complex patterns that were associated with giant convection cells (see Fig. 1.6). Those authors also characterized these structures by obtaining their contrast and size and compared these quantities with existing theoretical models that relate the convective structure with the stellar parameters (see Fig.1.7). Their results provided an observational test that served as motivation for studying the surfaces of other evolved stars with high-angular resolution techniques.

From the theoretical point of view, realistic modeling of the underlying physical processes involved in convection is a notoriously tricky problem, and theoretical studies found in the literature are usually restricted to 1D simulations (see Sec. 1.3.3). Still, these dynamical 1D atmospheres and wind models have been used successfully to explore the basic dust-driven mass-loss processes, relying on a parameterized description of sub-photospheric velocities due to radial pulsations (the so-called piston models; see, e.g., [Höfner 2008](#); [Jeong et al. 2003](#)). The combination of star-in-a-box models such as CO5BOLD ([Freytag et al. 2003](#)) with wind models such as Darwin ([Höfner et al. 2016](#)) can bring new descriptions of the asymmetric distributions of dust and gas observed in evolved stars. Those models can be confronted with high-angular resolution observations and analyses of the surface and the innermost CSE's of AGB stars.

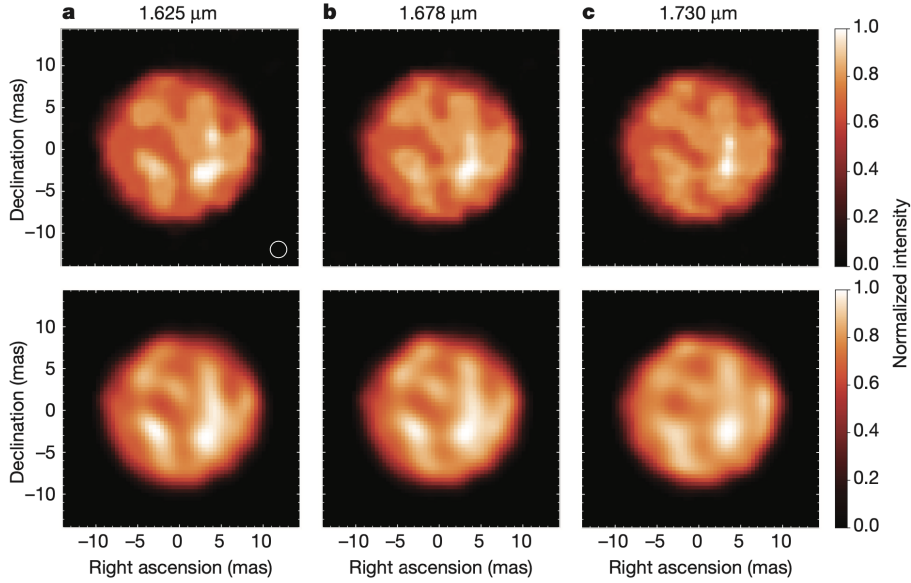


Figure 1.6: Best-reconstructed images of the stellar surface of the S-type AGB star π^1 Gru using interferometric data from the instrument PIONIER/VLTI in the H -band. These images were obtained using two different image reconstruction algorithms: SQUEEZE (upper panels) and MiRa (lower panels). The images reveal the presence of complex structures associated with giant convection cells. The white circle at the bottom right of the top panel in **a**, corresponds to the angular resolution of the observations ($\lambda/2B \sim 2$ mas). This image was taken from (Paladini et al. 2018).

1D convection and the Mixing Length Theory (MLT)

The following subsections are based on *A Review of the Mixing Length Theory of Convection in 1D Stellar Modeling* by Joyce & Tayar (2023) and are intended to provide a general description on how is the convection described in a 1D model, its limitations and the different approaches that can be employed to avoid those limitations.

Understanding and simulating energy transport in stars poses a complex challenge, especially due to the intricate nature of convection within stellar interiors. Direct observations struggle to unveil the details of convection, introducing significant uncertainties into stellar models. A reliable stellar evolution code must not only capture the diverse behaviors of stars over enormous ranges of temperature, density, and pressure but also span evolutionary timescales, from fractions of milliseconds for nuclear processes to billions of years. Considering spatial scales ranging from nuclear cross-sections to thou-

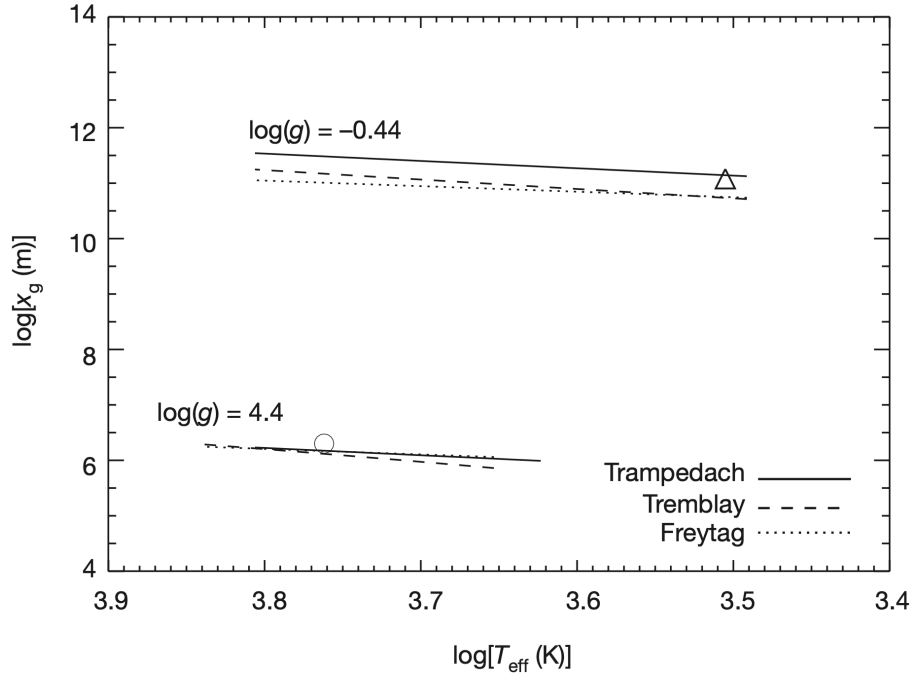


Figure 1.7: The characteristic granule size x_g obtained from the PIONIER images of π^1 Gru (triangle; $\log(g) = 0.44$) is quite different from the solar value (circle; $\log(g) = 4.4$). As it can be seen, the extrapolations of theoretical predictions (dotted line, dashed line, and solid line) to lower effective temperatures ($T_{\text{eff}} = 3200$ K, $\log(g) = 0.44$) are in good agreement with the observations. The image and its description were taken from [Paladini et al. \(2018\)](#).

sands of solar radii, simultaneous inclusion of all scales in evolutionary codes becomes computationally unfeasible. To address this, especially in the context of convection—a 3D, turbulent, non-linear, and time-dependent process—parametrizations are essential. The Mixing length theory (MLT) serves as a practical solution by offering a static 1D approach for the convenience of stellar modeling in such situations.

The MLT provides a simplified description of the bulk movement of fluids in analogy to molecular heat transfer. It considers the packets within a convection zone as discrete “parcels” of fluid, each with local uniform physical characteristics. These parcels are in pressure equilibrium with their surroundings but not in thermal equilibrium. Consequently, hotter parcels will move towards cooler regions, and cooler parcels will move towards hotter regions. The buoyancy force, driven by the under-density of hot parcels,

causes them to rise and expand, while cooler ones sink and compress. The characteristic distance a parcel can travel before losing its locally homogeneous characteristics is associated to its mean-free path, measured in terms of the pressure scale height $d \ln(P)/d \ln(T)$, of the stratified fluid.

In this section, I will formulate the mixing length theory by reproducing the standard derivation of the amount of flux carried by convection. This derivation is based on a framework presented in a review of the Mixing Length Theory of Convection in 1D Stellar Modeling by [Joyce & Tayar \(2023\)](#) which, at the same time, is based on derivations by Cox & Giuli's principles of stellar structure ([Cox 1968](#)), Kippenhan and Wiegert's Stellar Structure and Evolution ([Kippenhahn et al. 1990](#)), and Cassisi & Salari's Stars and Stellar Populations ([Salaris & Cassisi 2005](#)).

We first introduce the concept of pressure scale height H_p as a measure of the distance over which the total pressure, $P = P_{\text{gas}} + P_{\text{rad}}$, changes by a factor $1/e$. The following definition is valid under the assumption of hydrostatic equilibrium:

$$\frac{-d \ln P}{dr} \equiv \frac{\rho g}{P} = \frac{1}{H_p}. \quad (1.7)$$

In the MLT the "parcel of fluid" is considered to be in pressure, but not in thermal equilibrium with its surroundings. We next define, at a given radius r , (1) the average (ambient) temperature gradient of the fluid, with respect to the pressure of all matter, and (2) a temperature gradient of the fluid parcel itself, also taken with respect to the total pressure. We define (1) by:

$$\nabla \equiv \frac{d \ln T}{d \ln P}, \quad (1.8)$$

and (2) by

$$\nabla_{\text{parcel}} \equiv \frac{d \ln T_{\text{parcel}}}{d \ln P}, \quad (1.9)$$

where T and T_{parcel} are the average (ambient) and the parcel temperature, respectively. [Fig 1.8](#) shows a schematic representation of the previous scenario. The difference between the parcel's temperature and the ambient temperature at some radial shift Δr , in terms of a first-order Taylor expansion, can be expressed as

$$\Delta T(\Delta r) = T_{\text{parcel}}(r + \Delta r) - T(r + \Delta r) \simeq \Delta r \left[\frac{dT_{\text{parcel}}}{dr} - \frac{dT}{dr} \right], \quad (1.10)$$

Assuming that the temperature change over Δr is small, $T \simeq T_{\text{parcel}}$, and so

$$\Delta r \left[\frac{dT_{\text{parcel}}}{dr} - \frac{dT}{dr} \right] \rightarrow \Delta r T \left[-\frac{d \ln T}{dr} - \left(-\frac{d \ln T_{\text{parcel}}}{dr} \right) \right]. \quad (1.11)$$

Using the chain rule and the definition from Eq. 1.7, we can rewrite

$$\frac{d \ln T}{d \ln P} = \frac{d \ln T}{dr} \frac{dr}{d \ln P} = \frac{d \ln T}{dr} (-H_p). \quad (1.12)$$

By substituting Eqs. 1.8 and 1.9 into Eq. 1.11 we obtain

$$\Delta T(\Delta r) = \Delta r \frac{T}{H_p} (\nabla - \nabla_{\text{parcel}}). \quad (1.13)$$

We note here that the moving parcel can exchange heat with its environment, and so ∇_{parcel} is a function of the rate at which this exchange takes place. However, the assumption that the parcel does not change heat with its surroundings, i.e., that it is moving adiabatically is a reasonable and simplifying assumption for stellar conditions. In this case,

$$\nabla_{\text{parcel}} \rightarrow \nabla_{\text{ad}} = \left. \frac{d \ln T}{d \ln P} \right|_{\text{ad}}. \quad (1.14)$$

In the derivation of the MLT, it is important to note that the previous equation (Eq. 1.14) is not interchangeable with Eq. 1.8. The adiabatic temperature gradient, ∇_{ad} , and the average or ambient temperature gradient, ∇ , are not, in general, the same. We also do not know the definition of ∇ in a convective region. Substituting ∇_{parcel} for ∇_{ad} and combining with Eq. 1.13 yields

$$\Delta T(\Delta r) = \Delta r \frac{T}{H_p} (\nabla - \nabla_{\text{ad}}). \quad (1.15)$$

Now, the convective flux transported by a parcel of fluid moving upwards with velocity v over some distance λ is given by

$$F_{\text{conv}} = \frac{1}{2} \rho v c_p \left[\left(\frac{dT}{dr} \right)_{\text{ad}} - \left(\frac{dT}{dr} \right) \right] \lambda, \quad (1.16)$$

where ρ is density, c_p is specific heat, and the factor of 1/2 emerges from the assumption that half of the material in a given layer is rising while half is falling. Given the following relation

$$\frac{dT}{dr} = -\frac{T}{H_p} \frac{d \ln T}{d \ln P} = -\frac{T}{H_p} \nabla \quad (1.17)$$

and Eq. 1.13, we have

$$F_{\text{conv}} = \frac{1}{2} \rho v c_p \left[\left(-\frac{T}{H_p} \nabla_{\text{ad}} \right) - \left(-\frac{T}{H_p} \nabla \right) \right] \lambda. \quad (1.18)$$

Finally, by rearranging the previous equation, we have

$$F_{\text{conv}} = \frac{1}{2} \rho v c_p T \frac{\lambda}{H_p} (\nabla_{\text{T}} - \nabla_{\text{ad}}), \quad (1.19)$$

with

$$\alpha_{\text{MLT}} \equiv \frac{\lambda}{H_{\text{P}}}. \quad (1.20)$$

The previous definition is that of the *mixing length parameter*. This is a dimensionless parameter, characterizing the "distance", measured in terms of the pressure scale height (Eq. 1.7), that a parcel of convective material can travel.

This α_{MLT} can be thought of in many ways, including as the convective mean-free path, as a measure of the *convective efficiency*, or as a pseudo-physical quantity that captures the change in entropy from the base to the top of the convection zone. As can be seen, Eq. 1.19 is determined according to two things: (i) the difference in the temperature gradients and (ii) the value of α_{MLT} . In other words, α_{MLT} modulates the suppression or enhancement of the surface convective flux so that larger values mean that more flux is carried by convection.

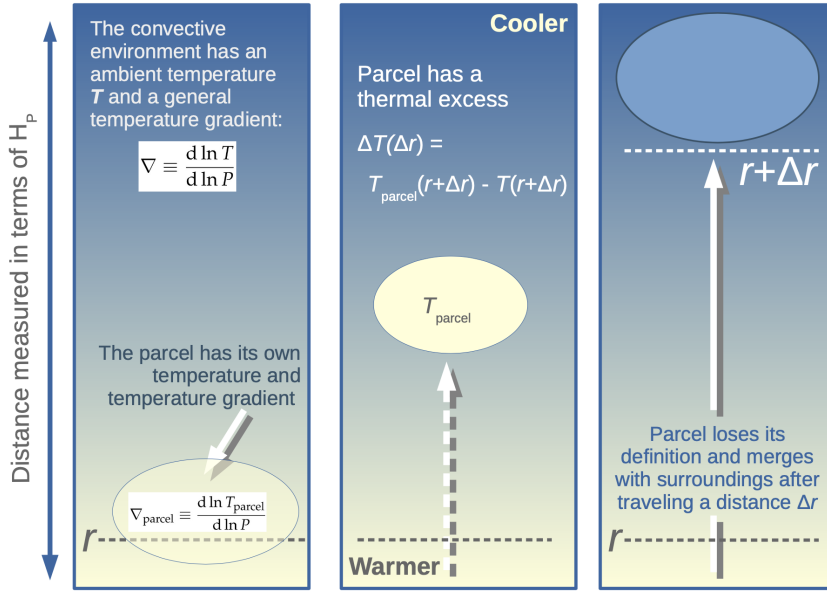


Figure 1.8: An illustration of the movement of a convective blob across the medium. The distance a convective parcel can travel is measured in multiples of the pressure scale height, H_{p} . A larger mixing length implies that the parcel travels over a larger pressure differential before mixing with its surroundings, which corresponds to more efficient transport of the flux by convection. Image taken from [Joyce & Tayar \(2023\)](#).

Limitations of the MLT

Although MLT has proven to be useful in describing convection, sometimes it requires to make naive and outright incorrect physical assumptions. In this section, I will briefly describe some of these assumptions and contrast them with the real physical phenomena taking place inside the stars.

Advective processes involve the transportation of material or energy through the bulk motion of fluids. Models employing a diffusive approximation represent particle-like fluid parcels diffusing through the region to redistribute heat. However, in reality, the notion of a homogeneous convective material unit sustained over a considerable distance is invalid. Convection operates through a continuum of constantly-changing up-flow and down-flow channels.

The MLT supposes **rigid convective boundaries**. However, in the real life, convective boundaries are permeable, flexible and are subject by the inertia of convective motions carrying convective plumes across the convective-radiative boundary. In these regions, the local mixing occurs and MLT cannot account for this.

The MLT introduces the simplification of **strictly vertical paths** due to its 1D formulation. This limitation arises because physical convection involves shearing, fragmentation, reorientation, and deletion of flow channels, features that a formulation relying solely on radial displacements cannot capture.

Time dependency in the MLT is not taken into account. This means that the formulation cannot capture any physics happening faster than the convective turnover time. In standard treatments, convective regions are assumed to be instantaneously mixed over one evolutionary time step.

Flow channels. In physical convection, there is an asymmetry between upflows (hot material rising) and downflows (cool material falling). The MLT falls to account for this effect.

The mixing length parameter, α_{MLT} , in many MLT formulations is often considered a free, numerical parameter with loose connections to any physical property of the star. However, it is linked to the entropy jump between zones of efficient and less efficient convection, specifically, the asymptotically adiabatic portion of the convection zone and the top of the convective envelope. Although characteristics like entropy jump, density gradient, and convective envelope properties are not directly observable, asteroseismology provides an indirect method for investigating these attributes. Direct calibration

of α_{MLT} is crucial, and observations of our nearest star offer the most straightforward means for this calibration.

Extensions to 3D

Scientific efforts in utilizing 3D simulations of convection are on the rise, aiming to refine the representation of mixing length in a manner that aligns more realistically with convection physics. Recent advancements in 3D simulations enable consideration of not only local and static mixing length but also global derivatives, asymmetries between upflows and downflows, larger-scale star properties, and transverse versus radial differences. These simulations generally indicate a slight variation in the mixing length concerning the star's composition, luminosity, and surface gravity, likely attributed to the physics of turbulent dissipation (Trampedach et al. 2014; Magic et al. 2015; Sonoi et al. 2018).

In terms of trends observed in 3D simulations between α_{MLT} and global properties such as metallicity, they often align directionally with trends implied by 1D stellar model calibrations to match observational data (Bonaca et al. 2012; Creevey et al. 2015; Tayar et al. 2017; Joyce & Chaboyer 2018a,b; Viani et al. 2018). However, quantitative agreement is rare. In some cases, 1D-to-observational calibrations suggest a need for a α_{MLT} variation about ten times larger than indicated by 3D simulations (see e.g., Joyce & Chaboyer 2018a; Trampedach et al. 2014). This points to a potential need for further refinement in three-dimensional simulations or additional corrections to the physics of 1D stellar evolution calculations impacting the inferred mixing length.

Interferometry

This chapter gives an introduction to the terminology and the basic concepts of optical/infrared long baseline interferometry. It is based mainly on the books by [Lawson \(2000\)](#), [Monnier \(2003\)](#), and [Buscher \(2015\)](#).

2.1 Principles of interferometry

A telescope's angular resolution ($\Delta\theta$) is its capacity to discern between two separate close objects in the sky. It depends on the wavelength of interest, λ , and on the size of the telescope, usually quantified by the diameter D , of its primary mirror. The Rayleigh criterion establishes the diffraction-limited resolution of a circular telescope as:

$$\Delta\theta_{\text{tel}} = 1.22 \frac{\lambda}{D} \text{ rad.} \quad (2.1)$$

According to this relation, a telescope cannot distinguish objects separated by an angular distance smaller than $\Delta\theta_{\text{tel}}$. Table 2.1 shows typical angular resolutions in milliarcseconds for three wavelength regimes, considering Eq. 2.1.

	Visible 0.4 - 1 μm	NIR 1 - 5 μm	MIR 10 - 20 μm
$D = 8 \text{ m}$	12.5 - 31.5 mas	31.5 - 157 mas	315 - 630 mas
$D = 100 \text{ m}$	1 - 2.5 mas	2.5 - 12.5 mas	25 - 50 mas

Table 2.1: Angular resolution of telescopes with different diameters (8 and 100m) for three different band-passes.

Let's take an example to illustrate the angular resolution. AGB stars are very bright in the infrared (see Chapter 1); therefore, NIR or mid infrared (MIR) wavelength observations are well suited to study these kinds of objects. If the typical size of the dust shell at 11 μm is ~ 50 mas (50 AU at a distance of 1 kpc), we would need a telescope of approximately 45 m to resolve it. However, this is more than the size of the European Extremely Large Telescope (E-ELT; 38 m) that the European Southern Observatory (ESO) is currently building.

Another example includes active galactic nuclei (AGN), whose nucleus is about one mas in the MIR (5 μm). To properly resolve this part of the AGN, a 100 m telescope would be needed. However, such kinds of instruments are too expensive, so astronomers have to adopt a different technique to resolve astronomical objects: interferometry.

In this technique, the light of a source is collected through two (or more) spatially separated apertures and then is combined coherently. Instead of observing the brightness distribution of the object directly, we observe an interference pattern (see Fig. 2.1). The interferometric observable derived from these fringes is the so-called *complex visibility*, V . Using this technique, we gain angular resolution at the cost of having a lower sensitivity and no direct imaging.

The angular resolution achieved by a two-station interferometer, considering the full constructive interference, is:

$$\Delta\theta_{\text{int}} = \frac{\lambda}{B} \text{rad}, \quad (2.2)$$

where B is the projected separation in the plane of the sky between the two telescopes, called the baseline length. This criterion can be relaxed when considering a partial-constructive interference up to a limit of $\Delta\theta_{\text{int}} > \frac{\lambda}{2B}$, where the interference is completely destructive (Monnier 2003).

The link between the intensity distribution of a source projected in the plane of the sky and the complex visibility is given by the Van-Cittert-Zernicke theorem:

The complex visibility is the Fourier transform of the source intensity distribution on the sky at the spatial frequency corresponding to the projected baseline on the sky per observing wavelength

This theorem can be expressed by the following equation:

$$I(\alpha, \beta) = \int_{-\infty}^{+\infty} \int_{-\infty}^{+\infty} V(u, v) e^{2\pi i(\alpha u + \beta v)} du dv, \quad (2.3)$$

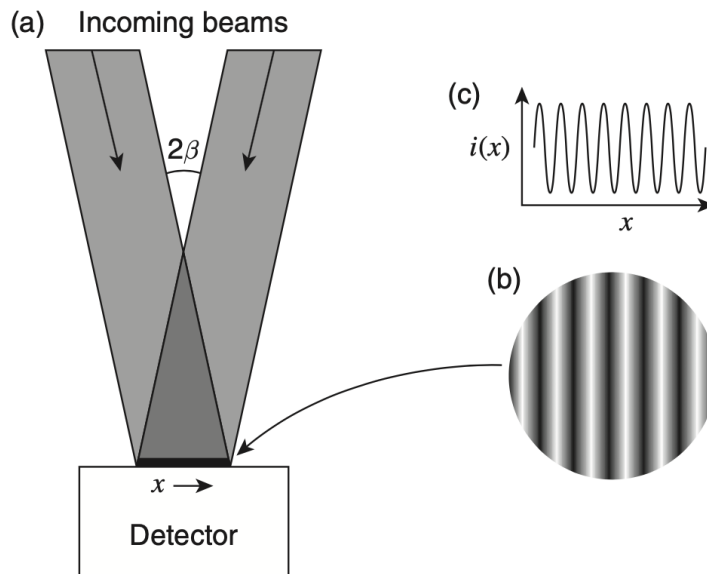


Figure 2.1: (a) Beams of light from a source arriving at angles of $\pm\beta$ on a detector. (b) The fringe pattern on the detector. (c) A one-dimensional cut through the fringe pattern. Image taken from [Buscher \(2015\)](#).

where I is the intensity distribution of the observed source, (α, β) are the angular coordinates of the source in the sky (in radians), V is the so-called complex visibility, and u, v are the spatial frequencies that describe the brightness distribution. The spatial frequencies are related to the baseline, B , through the following expressions:

$$u = \frac{B\alpha}{\lambda}; v = \frac{B\beta}{\lambda}. \quad (2.4)$$

In interferometry, the term $u - v$ plane is used frequently. This is the complex plane sampled with the interferometric observations. For instance, a two-aperture telescope configuration will give one point in the $u - v$ plane, meaning one visibility. Ideally, in order to reconstruct an image of a given source, one should fill the $u - v$ plane with several interferometric observations (see, e.g., Fig 2.2).

2.1.1 Visibility amplitude

The visibility is a measurement of the contrast between the fringes in the interference pattern (Fig. 2.1 and Eq. 2.5). Usually, this quantity is normalized, meaning that it takes values between 0 and 1. For instance, an unresolved point source will have

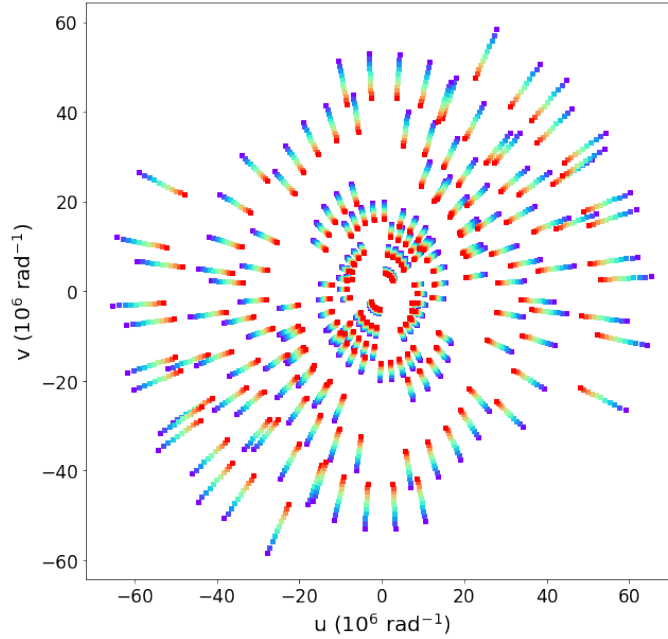


Figure 2.2: Example of the u - v plane achievable with GRAVITY using three Telescope arrays: short ($B_{\max} \sim 30$ m), medium ($B_{\max} \sim 100$ m) and large ($B_{\max} \sim 140$ m), each color corresponds to a different wavelength between 2 and $2.4 \mu\text{m}$ (K band).

high contrast fringes (see the upper row in Fig. 2.3) and a normalized visibility of 1. For a spatially resolved star, light from across the stellar surface combines incoherently, causing a decrease in the fringe contrast and, therefore, a drop in the visibility amplitude. Thus, the normalized visibility amplitude for a resolved source will be less than 1. The bigger the star, the lower the fringe amplitude (see Fig. 2.3 for an illustration of this effect). By measuring the visibility, one can determine a star's size, shape, and surface features. This can be done, for example, through modeling the brightness distribution of the source (see Fig. 2.4).

$$V = \frac{I_{\max} - I_{\min}}{I_{\max} + I_{\min}}. \quad (2.5)$$

2.1.2 Visibility phase

The phase is related to the fringe location with respect to a reference (called phase center or phase reference). This quantity carries information about the geometry, i.e., symmetry of the object. For instance, an object is called asymmetric when the shape

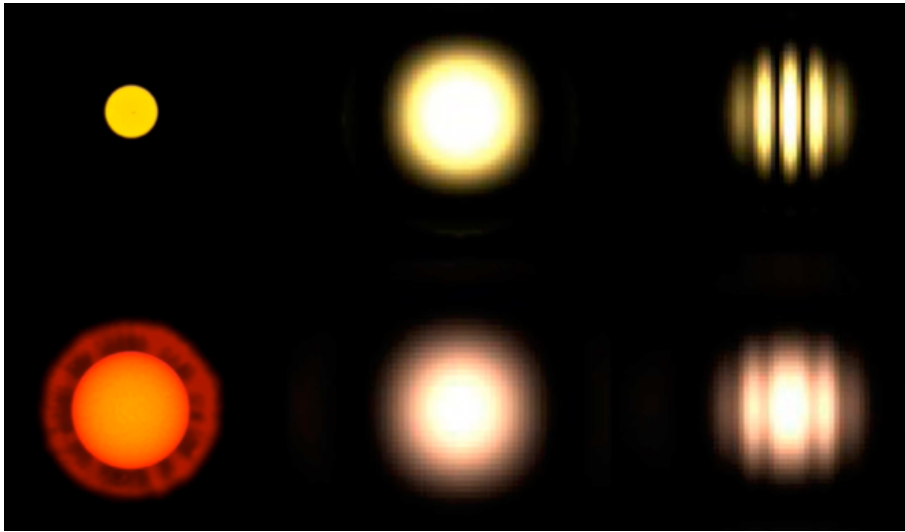


Figure 2.3: Comparison between single-dish and interferometric observables for two objects with different sizes. Left: two simulated stars of different sizes. Center: the same objects as seen by a single-dish telescope. Right: the interference patterns produced by the two objects. It is worth noting that the contrast between fringes is smaller for more extended objects. This image was taken from the [ESO web page](#).

is not centrally-symmetric; an ellipse is symmetric, but an ellipse with a spot inside is not ¹. Talking about astrophysical objects, a binary whose components have the same brightness is symmetric, but if the brightness is different, then the binary is asymmetric. These asymmetries in the binary can also be observed in the visibility curves (see Fig 2.5).

2.1.3 The effect of the atmosphere on the interferometric observations

When performing optical interferometry from the ground, one must remember that quantities like the phase of the complex visibility are very sensitive to atmospheric turbulence. In fact, many of the critical design parameters of an interferometer, such as site selection, operating wavelength, aperture size, and inclusion of adaptive optics, are driven by the boundary conditions set by the atmosphere. The sensitivity of interferometers, and the

¹An ellipse is centrally symmetric because it has an axis of symmetry passing through its center. If we add a spot away from the center of the ellipse, the symmetry breaks because there is no longer a corresponding point on the opposite side of the ellipse that mirror's the spot position.

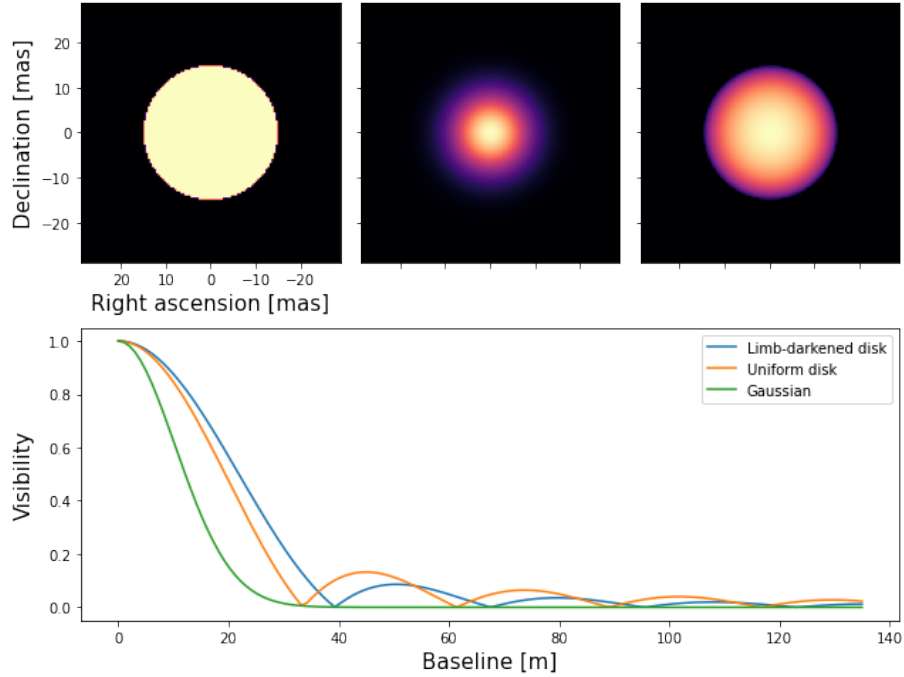


Figure 2.4: Top panel: Simulated images of three models (From left to right: Uniform, Gaussian, and Limb-darkened disk). All the models have a diameter (or Full Width Half Maximum (FWHM) in the case of the Gaussian model) of 15 mas. Bottom panel: Visibility curves for the three models versus baseline length at $2 \mu\text{m}$ (see the labels on the plot). The "first lobe" of the visibility curve (before the visibility amplitude reaches the first zero) contains information about the size and shape of the star. The second and higher-order lobes of the visibility curve also encode information about the surface features of the star, including limb-darkening, starspots, and convection cells.

precision of astrometric measurements, depend strongly on the seeing (Lawson 2000).

When taking interferometric observations, the atmospheric path length above each telescope generates phase shifts, η , in the recorded fringes. These phase shifts vary in proportion to the phase shift differences between the two telescopes forming a baseline. Hence, the phase of the measured visibilities, $\arg[V(u, v)]$, is affected as follows:

$$\arg[V(u, v)] = \Phi_{\text{real}} + (\eta_j - \eta_i). \quad (2.6)$$

The existence of phase delays, η , modifies the visibility phase so that it can no longer be associated with the Fourier phase of the source's brightness distribution. A new

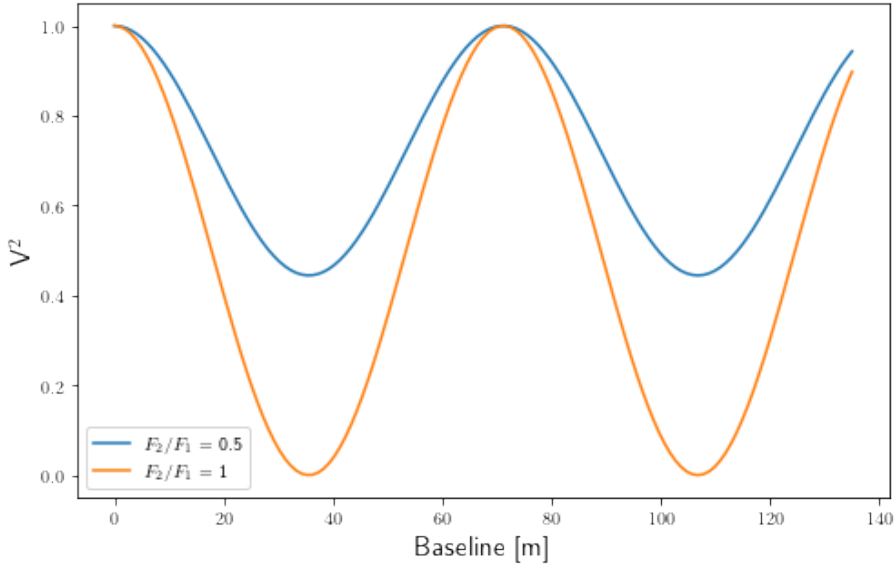


Figure 2.5: Visibility curves of two binary systems. The separation between the peaks in the visibility curve provides a measurement of the binary separation, while the minimum visibility reflects the flux ratio (F_2/F_1) between the components.

interferometric observable is then introduced to correct for this effect: the Closure Phase (CP) (Baldwin et al. 1986; Jennison 1958). This quantity is obtained by multiplying the visibility functions of three different baselines that form a closed triangle (see Fig. 2.6). By doing this, the telescope-dependent errors are canceled:

$$\begin{aligned}
 \Phi_{b_{12},\text{meas}} &= \Phi_{b_{12},\text{real}} + (\eta_1 - \eta_2) \\
 \Phi_{b_{23},\text{meas}} &= \Phi_{b_{23},\text{real}} + (\eta_2 - \eta_3) \\
 \Phi_{b_{31},\text{meas}} &= \Phi_{b_{31},\text{real}} + (\eta_3 - \eta_1) \\
 \Phi_{b_{12},\text{meas}} + \Phi_{b_{23},\text{meas}} + \Phi_{b_{31},\text{meas}} &= \Phi_{b_{12},\text{real}} + \Phi_{b_{23},\text{real}} + \Phi_{b_{31},\text{real}}. \quad (2.7)
 \end{aligned}$$

For instance, a point-symmetric object will have CPs equal to zero, while variations in the closure phases between -180 and 180 degrees will be observed for asymmetric objects. Given an interferometric array of N elements (telescopes), the total number of independent visibilities is equal to $N(N-1)/2$, and the number of independent closure phases is equal to $(N-1)(N-2)/2$. Since we need three phases to construct a CP, the number of CPs is smaller than the number of interferometric phases.

Apart from the atmospheric fluctuations, the detector noise can also affect the sen-

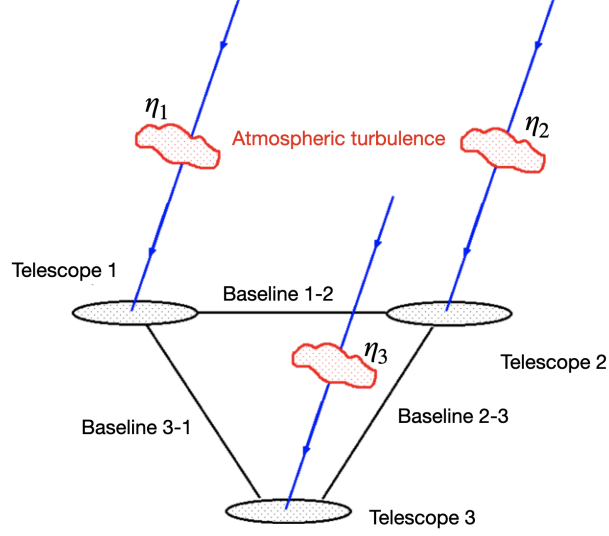


Figure 2.6: Phase shifts in the recorded fringes are introduced by the atmospheric turbulence. These phase shifts vary in proportion to the phase shift differences between the two telescopes that form a baseline and cancel out when we calculate the closure phase. This image was taken from the [University of Arizona](#).

sitivity of an interferometer. In the case of optical interferometry, this noise is produced by random arrivals of photons so, it follows a Poisson statistics. Variations of the average number of photons N_p arriving to the detector at a given time are given by: $\Delta N_p = \sqrt{N_p}$. Thus, the total number of photons recorded in a given interval of time is expressed as:

$$N_p = \eta \frac{P_\nu \Delta\nu}{h\nu} \tau, \quad (2.8)$$

where η is the total efficiency of the optical transmission system, P_ν is the power spectral density, τ is the time interval, ν is the frequency of the observation, h is the Planck constant and $\Delta\nu$ the bandwidth used. Since the coherence time is very small at IR wavelengths compared to radio (e.g., at $2.2 \mu\text{m}$: $\tau_c = 25 \text{ ns}$ and at 1 mm : $\tau_c = 14 \text{ fs}$), the number of photons recorded is considerably lower in a single exposure. To mitigate this problem, a series of short exposures are taken and the final detected signal, over which the fringe contrast (Eq. 2.5) is measured, corresponds to the average of the total power in the recorded exposures. Since the signal-to-noise-ratio (SNR) for optical interferometers scales as NV^2 , the total power of the visibility V^2 is a better observable than the amplitude V .

2.2 Interferometric facilities around the World

This section is intended to give an overview of the facilities around the world that can provide IR interferometric observations. Figure 2.7 shows the two big interferometers and others that are currently offered to the international community. In particular, I will only describe the CHARA and VLTI (Fig. 2.9) and give more emphasis to the VLTI instruments GRAVITY, PIONIER, and MATISSE (Fig. 2.10). I will briefly describe the reduction and calibration processes of these instruments, as the analyses reported in this thesis are based on observations taken with these three instruments. Finally, most of the information has been adopted from the websites of the instruments as well as the instrument's user manuals.

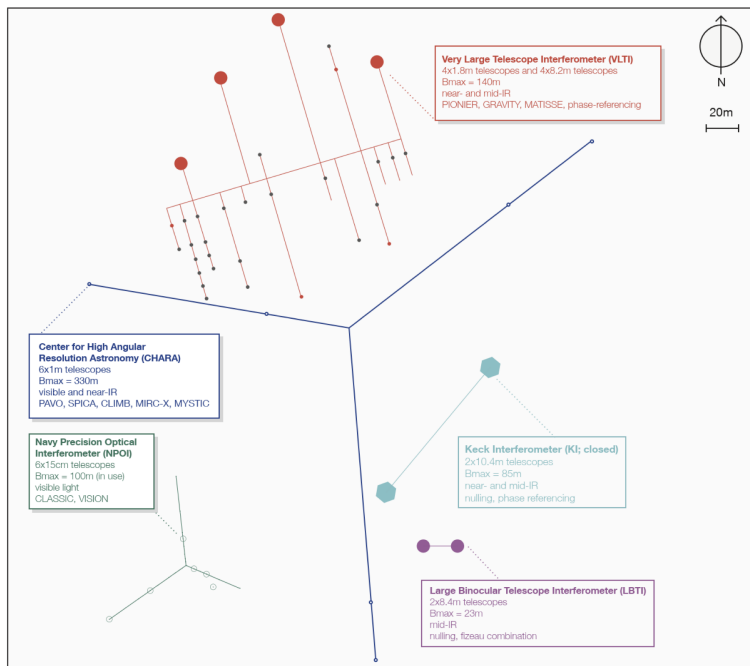


Figure 2.7: This sketch shows the footprints of modern O/IR interferometers, with telescopes and baselines to scale. The telescopes for LBTI (purple), CHARA (blue), and VLTI-UTs (red large circles) are fixed, while the NPOI (green) and VLTI-ATs (red small circles) telescopes are mobile and can be re-positioned. Image taken from Eisenhauer et al. (2023).

2.2.1 CHARA

The Center for High Angular Resolution Astronomy (CHARA)² is an optical interferometric array of six telescopes located in Mount Wilson, California. The array consists of six 1 m telescopes that are arranged in a Y-shape configuration providing 15 baselines ranging from 34 to 331 m (see Fig. 2.8). With the maximum baseline (331 m), CHARA can resolve objects as small as 0.2 mas at visible wavelengths and 0.5 mas in the near-infrared.

This instrument is particularly suited for stellar astrophysics, where it is used to measure the diameters and temperatures of stars, image features such as spots and flares on their surfaces (e.g., Norris et al. 2021), and map the orbits of close binary companions (e.g., Anugu et al. 2023). Other projects range from detecting other planetary systems (e.g., Martin et al. 2023), imaging stars in the process of formation (e.g., Labdon et al. 2023), and studies of bright transient phenomena like novae (e.g., Schaefer et al. 2014).

2.2.2 VLTI

The VLTI³ (Lena 1979; Beckers et al. 1990; Schöller 2007) is an interferometric array consisting of the four VLT 8 m Unit Telescopes (UTs) or the four movable 1.8 m Auxiliary Telescopes (ATs). It provides milli-arcsec angular resolution in low and intermediate ($R=4000$) spectral resolution at NIR and MIR wavelengths.

The four 8.2-m UTs and the four 1.8-m ATs are the light-collecting elements of the VLTI. The UTs are set on fixed locations while the ATs can be relocated on more than 10 different stations covering a baseline range between 30 and 130 m. All of the VLTI instruments recombine the light from four telescopes simultaneously. After the light beams have passed through a complex system of mirrors and the light paths have been equalized by the delay line system, the light re-combination is performed by the PIONIER and GRAVITY instruments in the near-infrared and by MATISSE in the mid-infrared part of the spectrum.

Due to its unique characteristics, the VLTI has become a very attractive means for scientific research on various objects like young pre-main sequence stars and their protoplanetary disks (see e.g., Ibrahim et al. 2023), post-main sequence mass-losing stars (Rosales-Guzmán et al. 2023), binary objects and their orbits (see e.g., Chauvin et al.

²<https://www.chara.gsu.edu/public/tour-overview>

³<https://www.eso.org/sci/facilities/paranal/telescopes/vlti.html>

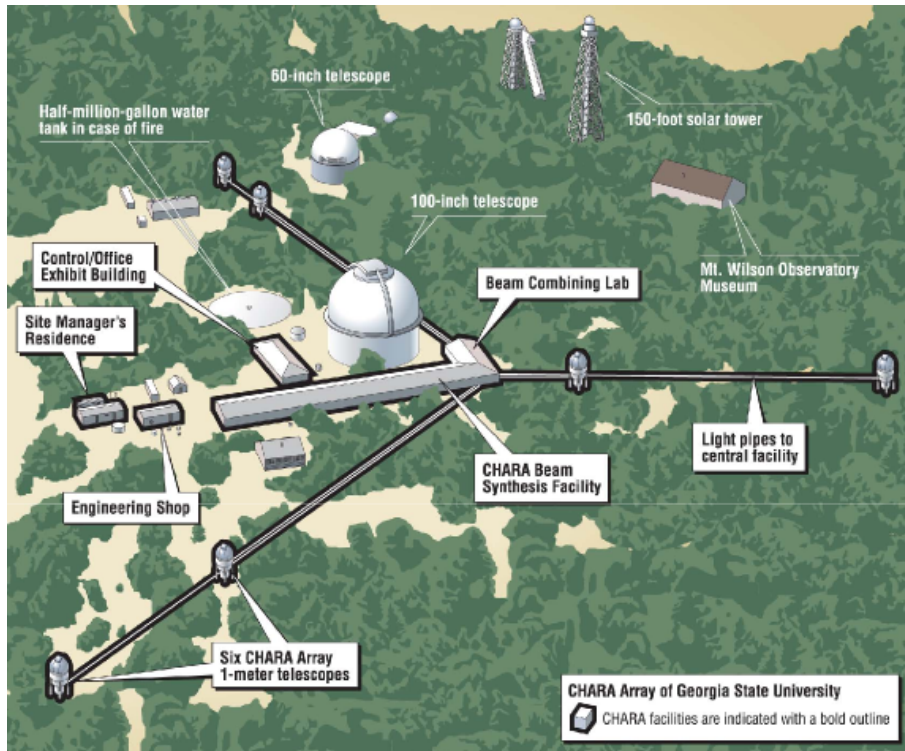


Figure 2.8: The CHARA array telescopes and its instruments (see the labels in the image). The image was taken from the [CHARA web page](#).

2023), and extragalactic objects such as active galactic nuclei (see e.g., [Isbell et al. 2023](#)).

PIONIER

PIONIER ([Le Bouquin et al. 2011](#)) is a four-telescope interferometric combiner at the VLTI operating in the H band ($1.6 - 1.99 \mu\text{m}$). It has a limited spectral capability of one spectral channel (bandwidth $\sim 0.3 \mu\text{m}$) or six spectral channels (spectral resolution $R \sim 40$). It measures simultaneously six squared visibilities and four closure phase values in order to characterize the spatial structure of a source at an angular scale as small as one mas at the longest baselines available. Its main characteristics are high efficiency making it suitable for interferometric imaging, and high accuracy of the measured quantities making it suitable for high contrast observations.

A typical PIONIER observation is composed of:

- A telescope preset



Figure 2.9: The Paranal Observatory telescopes. The instruments listed in italics are not yet in operation. The year in brackets indicates the start of operations. Image taken from the [ESO webpage](#).

- An instrumental setup
- An instrumental acquisition which requires
 - next exposures of nscan interferograms (typical 5 exp or 100 scans)
 - One dark exposure
 - A kappa matrix (measuring each beam individually = 4 exposures)

The observation of calibration stars is interleaved with the observations of the science star, all with the same instrumental setup. For instance, a typical sequence would be CAL1-SCI-CAL2-SCI-CAL1.

GRAVITY

GRAVITY ([Abuter et al. 2017](#)) is a four-telescope beam combiner operating in K band (1.9 - 2.4 μm). The instrument provides a spatial resolution $\lambda/2B = 1.58$ mas for a

baseline of 130 m at a wavelength $\lambda = 2\mu\text{m}$. It comes with multiple subsystems designed to accurately adjust and manage the incoming wavefront from the astronomical source as it travels from the telescopes to the beam combiner. These sub-systems include a fringe tracker, an IR wavefront sensor, a polarization control system, a pupil-guide, and a field-guide system.

GRAVITY forms spectrally dispersed interference fringes of either a single astronomical source (single-field) or of two sources simultaneously (dual-field and dual-field wide). The interferometric quantities provided by this instrument are the absolute and differential visibility, spectral differential phase, and closure phase. These quantities allow reconstructing images at a spatial resolution of two mas (when choosing the maximum baselines), as well as time-resolved differential astrometry per spectral bin at the accuracy of few tens of μas .

A full observation with GRAVITY is composed of different steps. The first one is the instrument calibration, necessary to know the characteristics of the detector, the beam combiner's transfer matrix (pixel to visibility matrix), and some characteristics of the optics (spectrograph calibration, fiber dispersion, polarization). Once the instrument is calibrated, the observations of a science target can be performed either in single-field or dual-field mode.

Closest to the science observation, a calibrator star in single field mode, or a binary calibrator star in dual field mode has to be observed. Knowing the diameter of the calibrator is necessary to calibrate the two transfer functions of the instrument: the one of the fringe tracker channel and the one of the science spectrometer channel. In the dual field mode, two sets of observations are acquired by swapping the two targets in order to calibrate the zero point of the metrology. The pipeline reduces the data coming from the calibrator observation templates and generates visibilities and phases.

The calibration process can be started once the visibilities of the calibrator and science targets are recorded. During this process, the transfer function is computed from Eqs. 2.9 and 2.10, which is used to calibrate the science visibilities according to Eqs. 2.11 and 2.12.

$$V_{\text{inst}}^2 = (V_{\text{measured}}^2 / V_{\text{expected}}^2)_{\text{CAL}}, \quad (2.9)$$

$$CP_{\text{inst}} = (CP_{\text{measured}} - CP_{\text{expected}})_{\text{CAL}}, \quad (2.10)$$

$$V_{\text{calib}}^2 = (V_{\text{measured}}^2)_{\text{SCI}} / V_{\text{inst}}^2, \quad (2.11)$$

$$CP_{\text{calib}} = (CP_{\text{measured}})_{\text{SCI}} - CP_{\text{inst}}, \quad (2.12)$$

where CAL stands for the calibrator star and SCI for the science target.

MATISSE

The Multi AperTure mid-Infrared SpectroScopic Experiment (MATISSE) (Lopez et al. 2022) is a four-telescope beam combiner operating in the L (3 - 4 μm), M (4.5 - 5 μm), and N (8 - 13 μm) bands. The instrument provides spatial resolution $\lambda/2B = 2.25$ mas, and $\lambda/2B = 7.25$ mas for a baseline of 140 m and for wavelengths $\lambda = 3\mu\text{m}$ and $\lambda = 10\mu\text{m}$ respectively. It can provide data separated in many wavelengths at different spectral resolutions, low, medium, high, and very high ($R \sim 30, 500, 1000, \text{ and } 3500$) in the $L - M$ bands, and low and high ($R \sim 30, 220$) in the N band.

In each of the L , M , and N bands, MATISSE uses a multi-axial all-in-one beam combination, that is the four separated telescope beams are focused onto the detector by a common lens and produce six dispersed fringe patterns that are mixed into one single focal spot (an airy disc), representing the so-called interferometric channel. In the L and M bands, the total incoming flux is split between the interferometric channel and the four photometric channels (SiPhot mode). This mode allows us to simultaneously perform the source photometry and thus to properly calibrate the visibilities. In the N band, the source photometry is obtained after the fringes recording by closing alternatively the MATISSE shutters to feed the four photometric channels. This allows to improve the sensitivity by sending 100% of the total incoming flux in the different channels (HiSens mode).

To account for the thermal background emission, which is significant in the mid-infrared, two additional modulation steps have to be added to calibrate the data: the first one is chopping modulation which consists of observing the target and an empty area of the sky alternatively. The second modulation is an optical path difference (OPD) modulation, aimed at removing the low-frequency peak contamination, containing the contribution from the thermal background, to the fringe peaks (in the Fourier transform of the interferograms). The instrument's different modes (telescope chopping, detector integrations, OPD modulation) are synchronized all together to ensure minimum overheads when observing. Finally, a beam modulation (or beam commutation) is applied to the observations by swapping two-by-two beams in a four-step sequence. This feature is aimed at removing detection artifacts in the phases measured by the instrument (differential phases and closure phases). These artifacts are instrument phase residuals

located in the optical train between the Beam Commuting Device (BCD) and the detector (Lopez et al. 2022). The BCD is a module used to calibrate closure and differential phases.

A MATISSE observational sequence is composed of twelve one-minute-long exposures with simultaneous interferometric and photometric data in the L and M bands and four interferometric exposures followed by eight photometric exposures in the N band. The first four exposures are taken without chopping while the following eight exposures are taken with chopping. Each exposure is taken in one of the four configurations of the BCD. Overall this leads to four reduced OIFITS2⁴ (Duvert et al. 2017) files per pointed target (one for each BCD configuration) containing, per exposure, six dispersed squared visibilities, differential visibilities phases, and three independent dispersed closure phases (out of four in total). Then, the interferometric calibration is applied to the data: the targets used as calibrators (CAL) are corrected from their expected observables given the predicted value of their angular diameters, and each science target (SCI) is corrected from the transfer function estimated. The calibrated OIFITS2 files of the four BCD configurations are merged to produce a single calibrated OIFITS2 file for each CAL-SCI pair.

2.3 Image reconstruction in optical interferometry

As mentioned in previous sections, one of the caveats of performing interferometric observations is that we are not able to obtain a direct image of an observed object, but instead, we have its visibilities and phases (closure phases). Hence, interferometric data are challenging to interpret, and we must rely on different techniques to understand our observations. Perhaps, the most illustrative method of interpreting interferometric information is to perform image reconstruction. However, owing to the sparse $u - v$ coverage, the image reconstruction process is *ill-posed* as there are more *unknowns* (pixels in the image) than measurements. To sort out these effects, the problem of image reconstruction is approached using a regularized minimization of the form:

$$\mathbf{x}^+ = \operatorname{argmin}_x f(x), \quad (2.13)$$

⁴The Optical Interferometry exchange format (OIFITS) is a standard for exchanging calibrated data from optical (visible/infrared) interferometers. The standard is based on the Flexible Image Transport System (FITS).

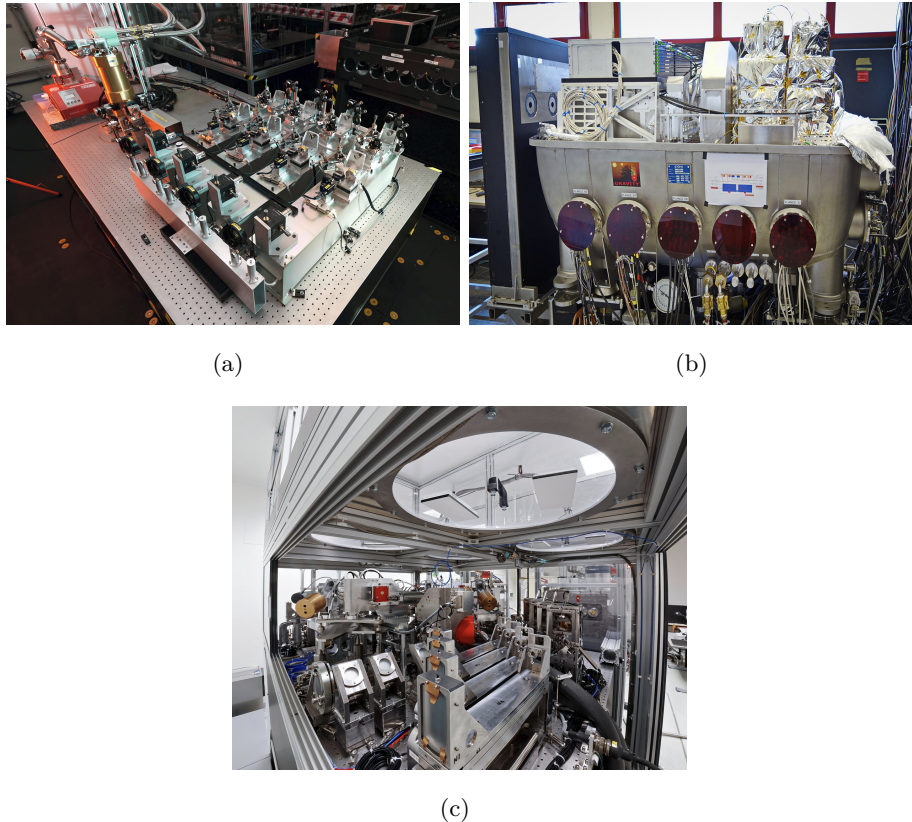


Figure 2.10: The three second-generation instruments at the VLTI: (a) PIONIER, (b) GRAVITY, and (c) MATISSE. The images were taken from the respective [ESO instrument web pages](#).

where \mathbf{x}^+ represents the solution we are looking for and

$$f(\mathbf{x}) = f_{\text{data}}(\mathbf{x}) + \mu f_{\text{prior}}, \quad (2.14)$$

where the *likelihood* term $f_{\text{data}}(\mathbf{x})$ measures the discrepancy between the model and the available data, while the *regularization* term $f_{\text{prior}}(\mathbf{x})$ measures the discrepancy with the *prior* information. The hyperparameter μ is used to adjust the relative weight of the constraints set by the measurements and the ones set by the priors (Renard et al. 2011; Sanchez-Bermudez et al. 2018).

There are many image reconstruction packages. The most commonly used are: BSMEM (Baron & Young 2008), SPARCO (Kluska et al. 2014), MiRA (Thiébaud 2009) and SQUEEZE (Baron et al. 2010). They mainly differ on how they minimize the

function f (Eq. 2.14). The reconstructed images reported in this thesis were obtained using BSMEM (which uses a gradient descent algorithm) and SQUEEZE (which uses a Markov Chain Montecarlo; MCMC). In the following sections, I will describe the capabilities of each one of these two algorithms. These sections are based on the article by [Sanchez-Bermudez et al. \(2016b\)](#), available at the Jean-Marie Mariotti Center ([JMJC](#)) page.

2.3.1 BSMEM

The BiSpectrum Maximum Entropy Method (BSMEM) was introduced in 1992 to demonstrate image reconstruction from aperture synthesis data, and it has been extensively enhanced since then ([Baron & Young 2008](#)). The algorithm employs a fully Bayesian approach to the inverse problem of finding the most probable image given the evidence, using the Maximum Entropy approach to maximize the posterior probability of an image. BSMEM uses a trust region method with non-linear conjugate gradient steps to minimize the sum of the log[likelihood] (χ^2) of the data given the image and a regularization term expressed as the Guy-Skilling entropy ([Gull & Skilling 1999](#)):

$$f_{\text{prior}}(\mathbf{x}) = \sum_n [x_n \log(x_n/\bar{x}) - x_n + \bar{x}_n], \quad (2.15)$$

with \mathbf{x} being the default image, which is the one that would be recovered in the absence of any data. The likelihood term used by BSMEM assumes independent Gaussian noise statistics for the amplitude and phase of the measured data. The optimization engine is MemSys created by Maximum Data Consultants Ltd., which implements the strategy proposed by [Skilling & Bryan \(1984\)](#) and automatically finds the most likely value of the hyperparameter μ that weights f_{prior} with respect to f_{data} .

The user can choose the default image (or model image) \mathbf{x} between a Gaussian, a Lorentzian, a uniform disk, or a delta function centered in the field of view, which conveniently fixes the location of the reconstructed object. It is worth noting that the bispectra and power spectra are invariant to translations. We will come back to this point in Chapter 4.

2.3.2 SQUEEZE

The primary engine of SQUEEZE is a MCMC algorithm. In interferometry, MCMC was first successfully implemented in image reconstruction in the radio by [Sutton & Wandelt](#)

(2006) then in the optical/IR by the MACIM software (Ireland et al. 2006). Like its predecessors, SQUEEZE uses the simulated annealing technique to converge to a global minimum of the posterior probability. An $N \times N$ pixel image is described by a collection of M elements, which may be pixel fluxes, wavelet coefficients, or model parameters. Defined steps, such as changing the flux of elements or moving them, are potentially taken on these elements in order to modify the image.

Regularization functions in SQUEEZE

Compared to BSMEM, SQUEEZE allows different regularization functions, either using them individually or combined. Some of the regularization functions allowed by SQUEEZE are the following (Sanchez-Bermudez et al. 2016b):

- **Entropy:** With this regularizer, one ensures that the image that best fits the data is the one with the minimum information. It is implemented in SQUEEZE as the sum of the natural logarithm of the Γ function for each one of the non-zero pixels in the image:

$$R(x) = \sum \log |\Gamma(x)|, \forall x \neq 0 \quad (2.16)$$

- **Dark Energy:** This counts all the zero elements in the image. The function implemented in SQUEEZE also adds values to the edges of the image. The equation of this regularizer is the following one:

$$R(x) = \sum x, \forall x = 0 \quad (2.17)$$

- **Uniform disk:** corresponds to the squared sum of the Lp-norm, with $p=0.5$, of the local gradient of the pixels (x_l) in the image. The SQUEEZE implementation ignores the image borders. The general formula of this regularizer is:

$$R(x) = (\sum \sqrt{\|\nabla x\|_{l,s}})^2, \quad (2.18)$$

$$\text{with } \|\nabla x\|_{l,s} = \sqrt{(x_{l+1,s} - x_{l,s})^2 + (x_{l,s+1} - x_{l,s})^2} \quad (2.19)$$

- **Total variation:** Instead of quantifying the intensity distribution in the image, this regularizer quantifies its spatial gradient distribution, helping us to describe uniform areas in the sought image with steep but localized changes (Strong & Chan 2003).

$$R(x) = (\Sigma \|\nabla x\|_{l,s})^2, \quad (2.20)$$

with $\|\nabla x\|_{l,s}$ as defined by Eq. 2.19.

- **L0 sparsity norm:** If an image is reconstructed using this regularizer, it will be forced to be the sparsest solution. Unlike other algorithms, SQUEEZE has the advantage of being able to optimize non-convex functions like the L0 norm. The mathematical formula of this regularizer is:

$$R(x) = \Sigma L0 \quad (2.21)$$

with $L0 = 1, \forall x > 1$

- **L2-norm:** This regularization function is part of the ℓ -p norm functions (with $p = 1.5, 2,$ and 3), which tend to produce smooth images as they reduce the variance in the pixels. The expression of the L2 norm is the following:

$$R(x) = \Sigma x^2 \quad (2.22)$$

- **Transpectral L2 regularization:** This regularization function is used for polychromatic image reconstructions. The function computes the L2-norm of the pixels across the different spectral channels in the data sets. The expression of this regularizer is:

$$R(x) = \Sigma_n \sqrt{\Sigma_l \Sigma_s (x_{l,s}^{\lambda_0})^2 + (x_{l,s}^{\lambda_1})^2 + \dots + (x_{l,s}^{\lambda_n})^2} \quad (2.23)$$

Figure 2.11 shows a reconstructed image using BSMEM and SQUEEZE. The (simulated) image corresponds to the "2004 interferometric imaging contest" and is always used for testing the algorithms once installed.

2.4 Studies of AGB stars through IR interferometric observations

In this section, I will give a brief review of some of the more common analyses that are performed on interferometric data. These analyses have provided important clues for our understanding of the physics around AGB stars and include: Model fitting, image reconstruction, model atmospheres and radiative transfer modeling. The works referenced in the text can be found also in Tables 2.2 and 2.3.

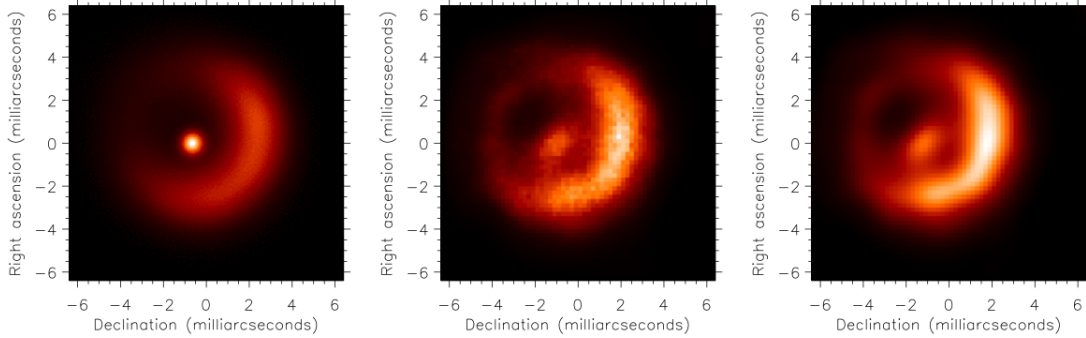


Figure 2.11: Reconstruction of the interferometric imaging contest data set of 2004. The “true” image is shown in the left panel, while the SQUEEZE and BSMEM reconstructed images are shown in the center and right panels, respectively. As can be seen, the BSMEM image is smoother due to the maximum entropy regularizer employed. The image was taken from [Baron et al. \(2010\)](#).

2.4.1 Model fitting

Early in this chapter, I mentioned that the estimation of the angular size of observed objects relies on geometric modeling of the V^2 . This method is widely utilized by various authors for estimating the angular size of their sources, as evidenced in works such as [Ireland et al. \(2004b\)](#), [Lacour et al. \(2009\)](#), [Rau et al. \(2015\)](#), [Ohnaka et al. \(2016\)](#), [Wittkowski et al. \(2016\)](#), [Ohnaka et al. \(2019\)](#), [Chiavassa et al. \(2020\)](#), [Perrin et al. \(2020\)](#), and [Rosales-Guzmán et al. \(2023\)](#).

2.4.2 Image reconstruction

When the interferometric observables are good enough, it is possible to perform an image reconstruction. Various algorithms can be applied for this task, and the quality of the reconstructed images is contingent upon factors such as data quality, the selection of regularizers, among others.

2.4.3 Model Atmospheres

The atmosphere of an AGB star is intricate, revealing evidence of diverse atoms and molecules through observed spectral transitions. Estimating the physical conditions responsible for these transitions involves atmospheric modeling. Models like PHOENIX

(Hauschildt & Baron 1999) can generate synthetic spectra and reproduce several spectral transitions at different wavelength ranges for comparison with observed spectra and interferometric observables (V^2), allowing the determination of fundamental stellar parameters such as temperatures, gravities, size in both continuum and molecular transitions, optical thickness, and more. Atmospheric modeling has been widely used to determine properties of AGBs (see e.g. Wittkowski et al. 2008, 2011, 2016; Rau et al. 2017; Wittkowski et al. 2018). However, it should be noted that these models are spherically symmetric, so they can only be used with V^2 data, meaning that information about asymmetries contained in the CPs is not taken into account.

2.4.4 Radiative transfer modeling

In radiative transfer modeling, a star with a temperature (T_{eff}) and a radius (R_*) emitting photons in a specified distribution (usually a blackbody distribution) is simulated. The photons emitted at the star's surface are free to travel through the CSE, and this interaction results in an intensity I_ν that can be calculated and then compared with observational data. In this type of model, the measured intensity will depend on the composition and distribution of the dust, making it possible to determine dust properties such as temperature, distribution, and optical thickness as a function of wavelength, among other properties. These models provide the user with a Spectral Energy Distribution (SED), but it is also possible to obtain synthetic images, from which interferometric observables can be extracted and compared with observational data (see e.g., Karovicova et al. 2011, 2013; Rosales-Guzmán et al. 2023).

2.4.5 The importance of observational evidence

Recent high-angular resolution interferometric observations of nearby AGB stars, conducted in both visual and infrared wavelengths, have unveiled intricate, non-spherical distributions of gas and dust in the close CSE (see, e.g., Wittkowski et al. 2017; Paladini et al. 2018). Temporal monitoring further indicates changes in atmospheric morphology and grain sizes over weeks and months, as demonstrated by studies like Ohnaka et al. (2017) and Norris et al. (2012). Spherically symmetric atmosphere and wind models prove to be inadequate for investigating such dynamic phenomena.

The development of a predictive mass loss theory requires realistic models encompassing stellar convection and pulsation, both of which significantly impact the stellar

atmosphere and wind. However, a well-elaborated mass loss theory remains ineffective without observations for comparison or to establish boundary conditions for these models. Hence, there is a growing interest in providing analyses of the innermost parts of AGB stars through high-angular resolution observations. These observations often involve multi-epoch and multi-band analyses of various sources, enabling the monitoring of gas and dust distributions over time and the tracking of chromatic changes across different wavelength bands. In addition to traditional analyses of high-resolution interferometric data, chromatic image reconstruction has emerged as a crucial tool for comprehending the morphology of AGB stars at various scales—from the surface to the CSE (see, e.g., Wittkowski et al. 2017; Paladini et al. 2018; Rosales-Guzmán et al. 2023).

In Sec. 2.3, I highlighted the numerous challenges associated with reconstructing images from interferometric data. When these challenges are mixed with the intrinsic variable nature of AGB stars, conducting multi-epoch and multi-band analyses through image reconstruction becomes a titanic task. To illustrate this fact, I performed a search into the ESO Telescope Bibliography webpage⁵ with the objective of finding the bulk of interferometric studies performed on AGB stars since 2004. Tables 2.2 and 2.3, and Figs. 2.12(a) to 2.12(c) show those findings. In all the plots, I present the effective temperature (T_{eff}) of the stars versus their log luminosity in solar luminosities $\log(L/L_{\odot})$.

An overview of the total number of AGB stars (including M-, S- and C-types) with interferometric analyses is presented in Fig. 2.12(a). Figure 2.12(b) contains a subsample including only M-type AGB stars. I selected the stars considering whether they were analyzed through image reconstruction (either in combination with model fitting or other analysis techniques) or analyzed through model fitting only. Finally, in Fig. 2.12(c), I show all the M-type AGB stars that include a multi-epoch and multi-band image reconstruction.

The sample size significantly decreases as more stringent requirements are imposed on the analyses conducted on the complete sample of stars. Ultimately, only a handful of sources undergo multi-epoch and multi-band interferometric image reconstructions. This highlights the need to expand the number of interferometric observations of nearby AGB stars. Such efforts are indispensable for acquiring additional information that will enhance our understanding of these intricate phenomena.

⁵<https://telbib.eso.org>

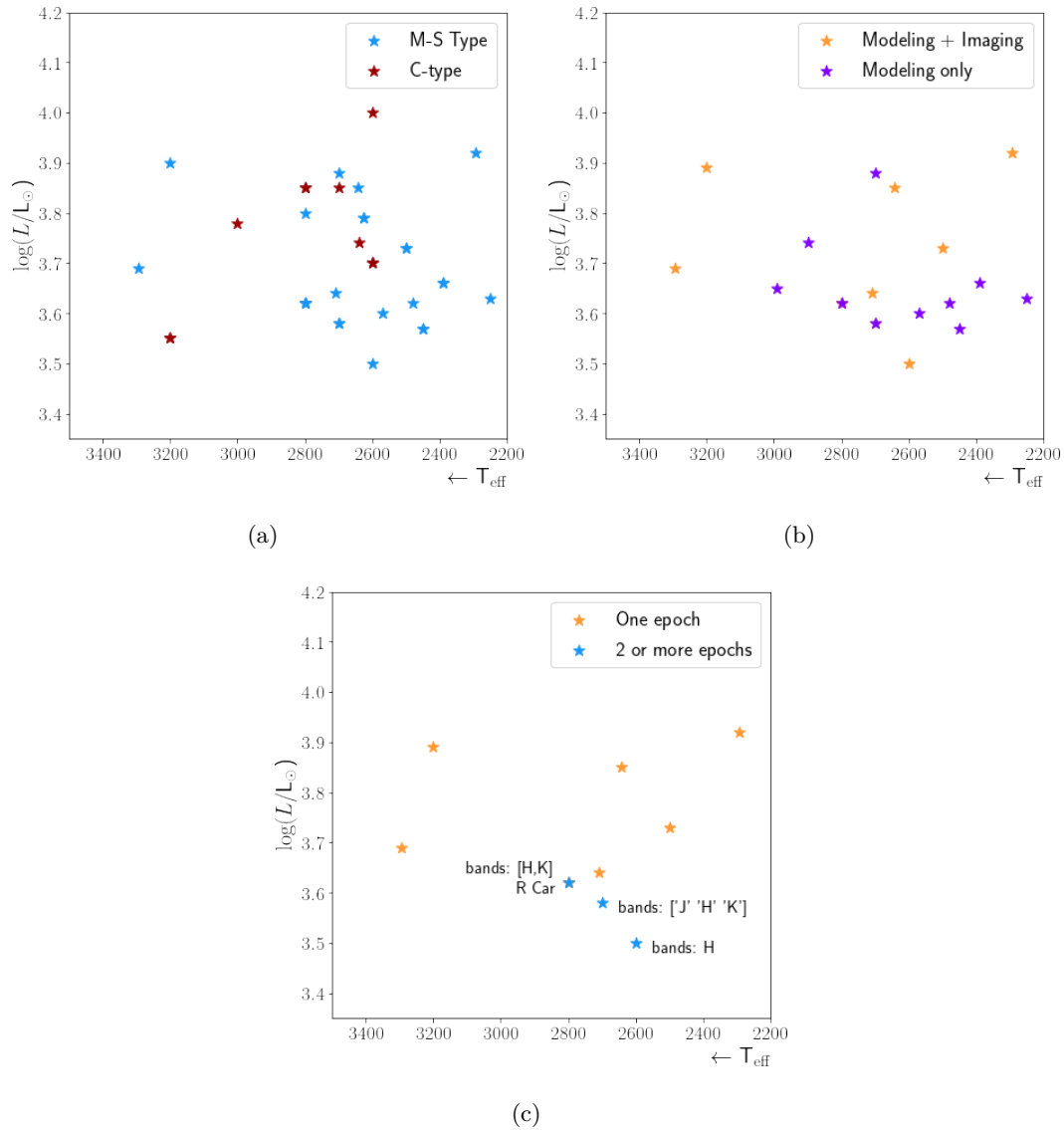


Figure 2.12: Overview of the total number of AGB stars studied with interferometric high-resolution observations. The panel a) shows both M- and C-type AGB stars (see the labels in the plot). The panel b) shows a sub-sample containing only M-type AGBs. The colors indicate whether image reconstruction was performed or not. Finally, the panel c) shows only M-type AGB stars where the main analysis is conducted through image reconstruction. The colors indicate whether a multi-epoch and/or multi-band analysis was performed. Note here that the source analysed in this thesis is labeled in the plot. In all the plots we present the effective temperature, T_{eff} versus $\log(L/L_{\odot})$ for the different sources.

Name	Sp. Type	T_{eff} [K]	$\log(L/L_{\odot})$	Bands	Analyses	Epochs	Instrument	Reference
AQ Sgr	C-type	2600	3.7	N	ModAtm	1	MIDI	Rau et al. (2017)
Chi Cyg	S-type	2600	3.5	H	ModFit, PI	4	IOTA	Lacour et al. (2009)
CL Lac	M-type	3293	3.69	H	ImRec, ModFit	1	CHARA	Chiavassa et al. (2020)
IK Tauri	M-type	2294	3.92	K	PolarIm, ModFit	1	AMBER	Ohnaka et al. (2016)
O Cet	M-type	2450	3.57	K	1D, 3D ModAtm	2	AMBER	Wittkowski et al. (2016)
O Cet	M-type	2450	3.57	H	ImRec, ModFit	1	IOTA	Perrin et al. (2020)
Pi Gru	S-type	3200	3.9	H	ImRec	1	PIONIER	Paladini et al. (2018)
R Aqr	M-type	2250	3.63	K	1D, 3D ModAtm	1	AMBER	Wittkowski et al. (2016)
R Car	M-type	2800	3.62	H	ImRec	1	PIONIER	Monnier (2003)
R Car	M-type	2800	3.62	H	ImRec	2	PIONIER	Rosales et al., (in prep)
R Car	M-type	2800	3.62	K	ImRec, ModFit	1	Gravity	Rosales-Guzmán et al. (2023)
R Car	M-type	2800	3.62	Vis	ModFit	1	SUSI	Ireland et al. (2004b)
R Cnc	M-type	2390	3.66	K	1D, 3D ModAtm	3	AMBER	Wittkowski et al. (2016)
R Cnc	M-type	2390	3.66	N	RadTransMod	2	MIDI	Karovicova et al. (2013)
R Dor	M-type	2710	3.64	K	ImRec, ModFit	1	AMBER	Ohnaka et al. (2019)
R Leo	M-type	2570	3.6	K	1D, 3D ModAtm	1	AMBER	Wittkowski et al. (2016)
R Lep	C-type	2800	3.85	N	ModAtm	1	MIDI	Rau et al. (2017)
R Peg	M-type	2480	3.62	K	ModAtm	4	Gravity	Wittkowski et al. (2018)

Table 2.2: High-resolution observations of AGB stars. All the references were retrieved from a search conducted on the [Telbib](#) web page and include studies from 2004 to 2023. The letters stand for ModAtm = Model atmospheres, ImRec = Image reconstruction, ModFit = Model fitting, PI = Parametric imaging, RadTransMod = Radiative transfer modeling, and PolarIm = Polarimetric imaging.

Name	Sp. Type	T_{eff} [K]	$\log(L/L_{sun})$	Bands	Analyses	Epochs	Instrument	Reference
RR Aql	M-type	2127	3.53	N	RadTransfMod	13	MIDI	Karovicova et al. (2011)
R Scl	C-type	2640	3.74	H, K	ImRec, ModFit	3	AMBER, PIONIER	Wittkowski et al. (2016)
R Scl	C-type	2700	3.85	K, N	Sed Modeling	4	MIDI, VINCI	Sacuto et al. (2011)
R Vol	C-type	2800	3.85	N	ModAtm	1	MIDI	Rau et al. (2017)
RU Vir	C-type	3000	3.78	N	ModFit	1	MIDI	Rau et al. (2015)
S Ori	M-type	2627	3.79	J, H, K	ModAtm, ModFit	1	AMBER	Wittkowski et al. (2008)
S Ori	M-type	2627	3.79	N	RadTransfMod	13	MIDI	Karovicova et al. (2013)
T Lep	M-type	2800	NA	J, H	ImRec, ModFit	1	AMBER	Le Bouquin et al. (2009)
U Hya	C-type	3200	3.55	N	ModAtm	1	MIDI	Rau et al. (2017)
U Ori	M-type	2641	3.85	H	ImRec	1	IOTA	Pluzhnik et al. (2009)
W Hya	M-type	2500	3.73	K	PolarIm, ModFit	1	AMBER	Ohnaka et al. (2016)
W Hya	M-type	2500	3.73	K	ModFit	2	AMBER	Hadjara et al. (2019)
W vel	M-type	2700	3.88	K	1D, 3D ModAtm	2	AMBER	Wittkowski et al. (2016)
X Hya	M-type	2700	3.58	K	1D, 3D ModAtm	2	AMBER	Wittkowski et al. (2016)
X Hya	M-type	2700	3.58	J, H, K	Image, modeling of V2	1	AMBER	Haubois et al. (2015)
X TrA	C-type	2600	4.00	N	ModAtm	1	MIDI	Rau et al. (2017)
Y Pav	C-type	3200	3.55	N	ModAtm	1	MIDI	Rau et al. (2017)

Table 2.3: High-resolution observations of AGB stars (Continued).

Interferometric analysis of the M-type Mira star R Car with PIONIER-VLTI

This chapter is based on the paper:

A new dimension in the variability of AGB stars: convection patterns size changes with pulsation recently sent to the A&A journal and which is in the review process.

A. Rosales-Guzmán, J. Sanchez-Bermudez, C. Paladini, B. Freytag, M. Wittkowski, A. Alberdi, F. Baron, J.-P. Berger, A. Chiavassa, S. Höfner, A. Jorissen, P. Kervella, J.-B. Le Bouquin, P. Marigo, M. Montargès, M. Trabucchi, S. Tsvetkova, R. Schödel, S. Van Eck

3.1 Our source: R Car

In this thesis, we analyze interferometric data of a prototypical M-type Mira star: R Car. This source exhibits variations in the V band from +3.9 to +10.5 mag. The proximity and brightness in the NIR and MIR of this source make it an ideal candidate for observation with infrared interferometry. In the following section I will provide relevant fundamental parameters of this star and a brief description on how they were obtained. All the parameters are gathered in Table 3.1.

One of the first estimates of the angular size of R Car was carried out by [Ireland et al. \(2004b\)](#). These authors obtained interferometric observations of the star in the V band (between 700-900 nm), using the Masked Aperture-Plane Interference Telescope (MAPFIT) system at the Anglo-Austrian Telescope (AAT). By fitting the V^2 using a Gaussian function, the authors derived an average FWHM of 20 mas in this band, with a size increase to 40 mas around 712 nm, corresponding to the location of a TiO band.

[McDonald et al. \(2012\)](#) derived an effective temperature, $T_{\text{eff}} = 2800$ K, luminosity, $L = 4164 L_{\odot}$, and period $P = 314$ days for R Car by comparing BT-Settl model atmospheres ([Allard et al. 2003](#)) to SEDs created from different surveys such as Hipparcos Tycho, Sloan Digital Sky Survey (SDSS), among others.

The radius of a pulsating star can be used to estimate the stellar mass when the characteristic period, the pulsation constant, Q , is obtained from theoretical considerations ([Kamezaki et al. 2012](#)). For instance, [Xiong & Deng \(2007\)](#) performed a detailed theoretical study on the radial pulsation of red giants and provided the period ratio and the characteristic period, Q for various models of giants. According to the authors, the relation between the period ratio and the pulsation constant has the form:

$$Q_{\text{F}} = -0.178(Q_{10}/Q_{\text{F}}) + 0.171, \quad (3.1)$$

where Q_{F} and Q_{10} are the pulsation constants for the fundamental and the 1st overtone modes, respectively. The relation between the period and the mean density of a pulsating star can be written in the following form (e.g., [Cox 2017](#)):

$$P(\rho/\rho_{\odot})^{1/2} = Q, \quad (3.2)$$

where P is the period of the star, ρ its mean density, $\rho_{\odot} = 1.41 \text{ g cm}^{-3}$ is the mean density of the sun, and Q is the pulsation constant ¹. Using Eqs. 3.1 and 3.2, [Takeuti et al. \(2013\)](#), estimated a mass $M = 0.87 M_{\odot}$ for R Car.

[Groenewegen et al. \(1999\)](#) found a mass loss rate $< 1.6 \times 10^{-9}$ for R Car through model fitting of the SED in the NIR and from the observed CO (3-2) line intensities. The observations that lead to these estimations were carried out with the IRAM 30 m telescope in September 1996.

¹Strictly speaking, Q is not constant. However, compared with other quantities that appear in pulsation theory, it remains in a relatively narrow range, making it useful for deriving the mean density of stars based on the pulsation period ([Takeuti et al. 2013](#); [Cox 2017](#)).

Parameter	Value	Ref.
Distance [Pc]	182 ± 16	Brown et al. (2021)
Period [Days]	314 ± 1 days	Lebzelter et al. (2005); McDonald et al. (2012)
M [M_{\odot}]	0.87	Takeuti et al. (2013)
T_{eff} [K]	2800	McDonald et al. (2012)
Luminosity [L_{\odot}]	4164	McDonald et al. (2012)
\dot{M} [$M_{\odot} \text{ yr}^{-1}$]	$< 1.6 \times 10^{-9}$	Groenewegen et al. (1999)
V band FWHM	15-20 mas	Ireland et al. (2004b)
H, K band magnitudes	-0.77, -1.23	Ducati (2002)

Table 3.1: Fundamental astrophysical parameters of R Car.

The photosphere of R Car was imaged with PIONIER, as part of the “*Interferometric Imaging Contest*” (Monnier et al. 2014). The data were obtained in January 2014 at the pulsation phase² $\phi = 0.78 \pm 0.02$. The reconstructed image shows a disk with an angular diameter of about 10 mas (~ 1.9 AU), and a couple of bright spots interpreted as convective cells. No further analysis has been carried out on those images until now.

3.2 Introduction to the problem of convection in AGB stars

The late phases of stellar evolution are largely affected by mass loss due to convection and pulsation processes, which in turn, significantly affect the structure and evolution of stars (Kupka 2004). In the case of convection, despite its importance, our current knowledge is still limited. Observationally, we mainly rely on studying the convective cells on the surface of the Sun. Schwarzschild (1975) suggested that the convection length scale is proportional to the pressure scale height of a stellar atmosphere. Hence, while the Sun has a couple of million cells on its surface, AGB stars will have (up to) a few tens of them. However, testing this hypothesis directly on resolved stellar surfaces has not been possible until very recently.

²Throughout the text we will refer to the pulsation phases of R Car obtained from the Visual light-curve of the object (see Fig.3.1), and they are defined as $\phi = (t - t_0)/T$ where t is the observing epoch, t_0 is a reference epoch, and T the period of the star.

High-angular resolution techniques are necessary to resolve those structures and IR interferometers played an important role in the last decade measuring the diameters of stellar disks and later on resolving smaller scale structures, which were related to convection (see e.g., [Le Bouquin et al. 2011](#); [Wittkowski et al. 2017](#); [Perrin et al. 2020](#)). One of the main challenges of studying convection in AGB stars is that their atmospheres are composed of molecular gases (e.g., H₂O, CO, HCN, etc.) and dust, obscuring the photosphere and making it difficult to observe the convective patterns. This is particularly important for carbon-rich AGB stars as shown in the *H* band images by [Wittkowski et al. \(2017\)](#). Oxygen-rich AGB stars are therefore better-suited targets to study convection because the dust is mostly transparent at the *H* ($\lambda_0 = 1.76 \mu\text{m}$) and *K* ($\lambda_0 = 2.2 \mu\text{m}$) bands, thus, allowing us to probe the photosphere observationally.

[Paladini et al. \(2018\)](#) used the PIONIER (Precision Integrated-Optics Near-infrared Imaging Experiment; [Le Bouquin et al. 2011](#)) instrument to image in the *H* band the stellar disk of the AGB star π^1 Gru. The interferometric images revealed the presence of bright spots that were associated with convective patterns. Those authors characterized their size to compare it, for the first time, with predictions from mixing-length theoretical models (e. g., [Freytag et al. 1997](#); [Trampedach et al. 2013](#); [Tremblay et al. 2013](#)). This reveals that the observational size of the convective structures agrees with a scale proportional to ~ 10 times the pressure scale height of the atmosphere. [Climent et al. \(2020\)](#) and [Norris et al. \(2021\)](#) conducted similar comparisons for a couple of red supergiant (RSG) stars. However, the estimated size of the convective patterns in RSG stars did not follow the theoretical predictions extrapolated from the Sun’s convection.

In this work, we analyze the 2014 PIONIER R Car data together with more recent data obtained in 2020. Our goal is to further characterize the structures on R Car’s surface to connect them with the pulsation of the star. Sect. 3.3 describes our observations and data reduction process. Sect. 3.4 presents our image analyses and results. In Sect. 3.5, we discuss our results in terms of the physical parameters of the star and the angular scales obtained for the convective elements. Finally, we present our conclusions in Chapter 5.

3.3 Observations and data reduction

Two datasets of observations were considered for our analysis. Both of them were taken using the 4-telescope beam combiner PIONIER. The first one consists of archival data

from February of 2014; the second one corresponds to observations taken between January and March of 2020³ (see Tables 3.2 and 3.3). The observations were taken at pulsation phases $\phi = 0.78 \pm 0.02$ and $\phi = 1.01 \pm 0.10$ for 2014 and 2020, respectively.

All data were taken with the 4 Auxiliary Telescopes (ATs). The baselines used reached a minimum and maximum resolution of 23.5 and 1.2 mas (at $\lambda_0=1.67 \mu\text{m}$ and in the super-resolution regime of $\lambda/2B_{\text{max}}$; being B the baseline length), respectively. The observations provided 6 spectral channels across the H band between 1.516 and 1.760 μm . The scientific data of R Car were interleaved with interferometric calibrators (i.e., point-like sources with similar brightness as the science target and within a few degrees of distance) to estimate the atmospheric and instrumental response function (the calibrators are listed in Tables 3.2 and 3.3).

The calibrated interferometric observables, squared visibilities (V^2), and closure phases (CPs), were obtained using the `pndrs` package (Le Bouquin et al. 2011). The final calibrated observables are the average of five consecutive five-minute object observations. Considering the calibration error in the observables, the V^2 and CPs reached a precision of $\sigma_{V^2} \sim 0.0025$ and $\sigma_{\text{CP}} \sim 1$ deg, respectively. The 2014 calibrated data were obtained from the archive "Optical Interferometry Data Base" (OiDB) supported by the JMMC. The interferometric observables and the uv-coverage(s) of both epochs are included in Fig 3.2.

3.4 Analysis and results

3.4.1 Diameter estimation: parametric uniform-disk model

To obtain the H band angular size of R Car, we applied the geometrical model of a uniform disk (UD) to the V^2 data. The visibility function of this model is defined by the following equation (Berger & Segransan 2007):

$$V_{\text{UD}}(u, v) = 2F_r \frac{J_1(\pi\rho\Theta_{\text{UD}})}{\pi\rho\Theta_{\text{UD}}}, \quad (3.3)$$

where J_1 is the first-order Bessel function; $\rho = \sqrt{u^2 + v^2}$ where u and v are the spatial frequencies sampled by the interferometric observations; Θ_{UD} is the angular diameter of

³More data were obtained for the star in 2019, however such data cover only one array configuration and are too far from the 2020 data in terms of pulsation phase to be combined with.

Table 3.2: Log of the observations for the 2014 data. HD 80603 (Diameter = 0.94 mas) and HD 81502 (Diameter = 1.23 mas) were selected as calibrator stars.

No.	Date	Target	Sta. Conf.	$\tau_0^{min} - \tau_0^{max}$ [ms]	N. Obs.
		HD 80603			
1	2014-01-22	R Car	D0-A1-C1-B2	2.18 - 8.8	98
		HD 81502			
		HD 80603			
2	2014-01-24	R Car	D0-H0-G1	3.77 - 5.03	12
		HD 81502			
		HD 80603			
3	2014-01-27	R Car	D0-G1-H0-I1	0.78 - 4.31	80
		HD 81502			
		HD 80603			
4	2014-01-28	R Car	D0-G1-H0-I1	1.83 - 14.92	82
		HD 81502			
		HD 80603			
5	2014-01-29	R Car	A1-G1-I1	2.58 - 10.33	52
		HD 81502			
		HD 80603			
6	2014-01-30	R Car	A1-G1-J3	1.97 - 11.88	56
		HD 81502			
		HD 80603			
7	2014-02-02	R Car	K0-A1-G1-J3	3.85 - 8.47	18
		HD 81502			

Table 3.3: Log of the observations for the 2020 data. HD 80404 (Diameter = 1.866 mas) and HD 71878 (Diameter = 2.949 mas) were selected as calibrator stars.

No.	Date	Target	Sta. Conf.	$\tau_0^{min} - \tau_0^{max}$ [ms]	N. Obs.
		HD71878			
1	2020-01-20	R Car	A0-G1-J2-K0	17.0 - 21.1	10
		HD 80404			
		HD71878			
2	2020-01-21	R Car	A0-G1-J2-K0	9.3 - 15.2	10
		HD 80404			
		HD71878			
3	2020-02-05	R Car	A0-B2-D0-C1	3.2 - 3.8	20
		HD 80404			
		HD71878			
4	2020-02-14	R Car	A0-B2-D0-C1	5.3 - 7.5	10
		HD 80404			
		HD71878			
5	2020-02-20	R Car	K0-G2-D0-J3	9.0 - 14.5	10
		HD 80404			
		HD71878			
6	2020-03-20	R Car	A0-B2-D0-C1	5.4 - 5.8	10
		HD 80404			

the uniform disk profile; and F_r is the scaling factor that accounts for the over-resolved flux in the observations. To fit the data, we used a MCMC algorithm based on the Python package `emcee` (Foreman-Mackey et al. 2013). We let 250 independent chains evolve for 1000 steps using the data of each one of the spectral bins independently. Finally, we averaged the best-fit UD diameters. This gave us an estimate of $\Theta_{UD}^{2014} = 10.23 \pm 0.05$ mas (1.86 ± 0.01 AU) for the 2014 epoch and $\Theta_{UD}^{2020} = 13.77 \pm 0.14$ mas (2.51 ± 0.23 AU) for the 2020 epoch. For instance, the diameter of the Sun is 9.35×10^{-3} AU so, the derived sizes are approximately 270 times the diameter of the Sun!

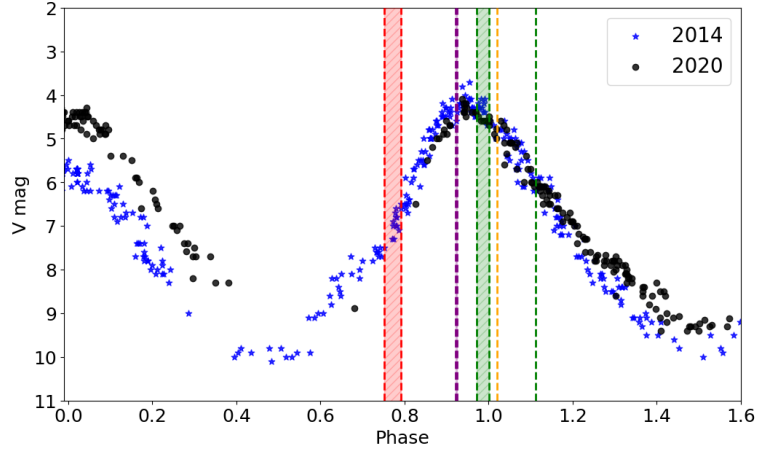


Figure 3.1: Visual light curves of R Car obtained from the [AAVSO](#) database as function of the pulsation phase around the dates of our interferometric observations. The blue stars and the black circles correspond to the data of the 2014 and 2020 epochs, respectively. The vertical-red shaded area indicates the phase of the 2014 interferometric observations, while the green line and the green, orange, and purple areas correspond to the 2020 ones at different station configurations: short, long, and astrometric, respectively (see Tables [3.2](#) and [3.3](#)).

3.4.2 Asymmetries in the stellar disk: regularized image reconstruction

To characterize the asymmetric structure of R Car observed in the large CP variations, we reconstructed aperture-synthesis images. For the 2014 image, we used the same setup used by J. Sanchez-Bermudez and described in [Monnier et al. \(2014\)](#). Since this image was already compared with other methods and reconstructions, confirming the validity of the structures observed, we did not made any further changes to the imaging setup.

For the 2020 data, we recovered images using a combination of SQUEEZE ([Baron et al. 2010](#)) and BSMEM ([Baron & Young 2008](#)). We recovered the images using a pixel sampling of 0.3 mas/pixel, with a pixel grid of 256×256 pixels (which encloses a field-of-view of ~ 77 mas). First, we ran SQUEEZE using 17000 iterations over 1000 independent chains. The images were recovered independently at each of the six wavelength channels. Two regularization functions were used: Total Variation, and Compactness with hyperparameter values of one and twenty, respectively (see [Sanchez-](#)

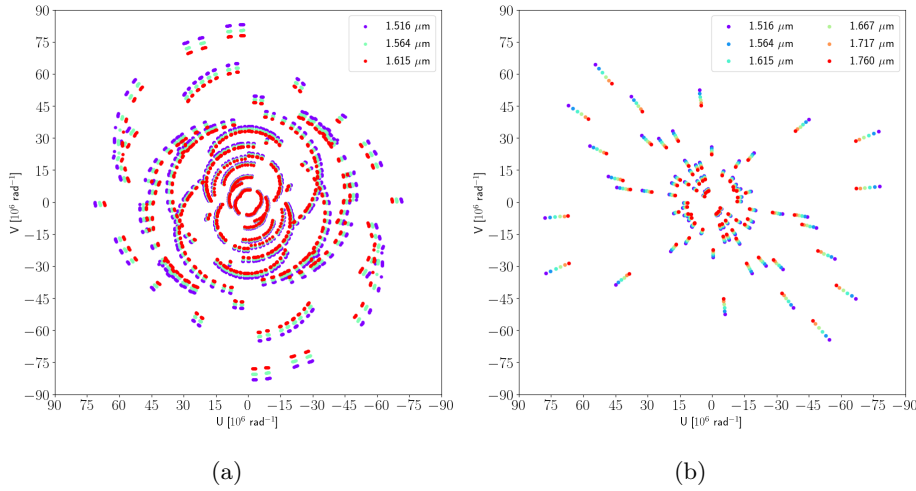


Figure 3.2: PIONIER u-v coverages of the data sets used in this study. The left panel corresponds to the 2014 data set, and the right one corresponds to the 2020 epoch. The colors in the panels show the different wavelengths covered with the band-pass of the instrument (see the labels on the plot).

Bermudez et al. 2018, for a more complete description of each regularizer). With this setup, we ensure the convergence of most of the chains with reduced $\chi^2 < 4$. We averaged the chains that converged into a single image. Finally, that mean image was used as starting point for BSMEM (which uses entropy as regularizer), to smooth it without increasing the residuals in the fitting of the observables. BSMEM converged in less than 100 iterations. Figure 3.3 shows our mean best-fit images from the 2014 and 2020 data and Figs. 3.6 and 3.7 show the comparison between the observables extracted from the reconstructed images and the data.

3.4.3 Power spectrum analysis

The H band images of R Car’s surface shown in Fig. 3.3 reveal the presence of several large bright spots. The comparison between the two images shows that those features change with time. We performed the analysis of the images’ power spectral density (PSD) to estimate the characteristic size of the structures (Paladini et al. 2018). The first step is to calculate the squared modulus of the Fourier Transform of the reconstructed images. The power spectrum of an image shows the flux distribution per spatial scale or spatial frequency, the smallest frequency being the one that encloses all the normalized intensity

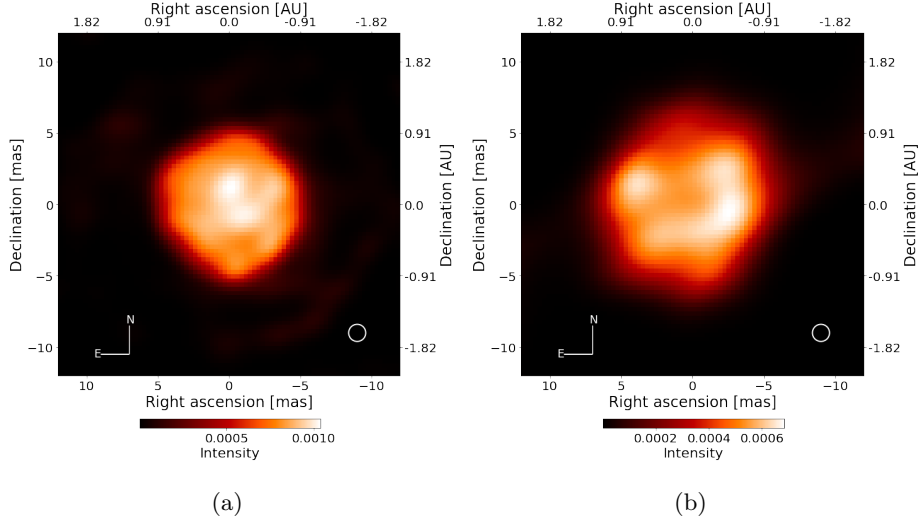


Figure 3.3: Best reconstructed images for the 2014 (left) and 2020 (right) datasets. The white circle located in the right corner of the images corresponds to the maximum resolution of the interferometer.

in the image; and the highest frequency is the one that maps the normalized intensity of the most compact features. To remove the stellar disk contribution from the PSD, we set the images' pixel values below 70% and 90% of the intensity's peak (for the 2014 and 2020 epochs, respectively) to the median flux of the pixels above the mentioned threshold values. To characterize the weight of the power, $P(k)$, at a given frequency, k , we computed the momentum of the power-spectrum $PSD(k) = k \times P(k)/P_{tot}$.

In order to estimate the loci of the spatial frequencies that dominate the PSDs, we averaged them radially. Fig. 3.4 shows the resulting radial averaged PSDs for both epochs. We fitted a Gaussian to the PSDs' peaks to determine the dominant spatial frequencies that trace the characteristic sizes of the structures in the surface of our object. For the Gaussian fitting, we used the Python tool `lmfit` (Newville et al. 2016). Since we only have a single image from the 2014 epoch, the reported uncertainties correspond to the standard deviation of the Gaussian fit. For the 2020 data, the model fitting was performed individually per spectral channel and, the reported errors correspond to the mean of the standard deviation of the best-fit peak positions across the wavelengths. The Gaussian center was limited within the range of $-0.6 < \log(k) < -0.2$ for the 2014 epoch and $-0.7 < \log(k) < -0.3$ for the 2020 epoch, respectively. The measured maxima in the PSDs trace sizes of 1.82 ± 0.16 mas ($4.94 \times 10^{10} \pm 4.89 \times 10^9$ m) and 2.51 ± 0.32

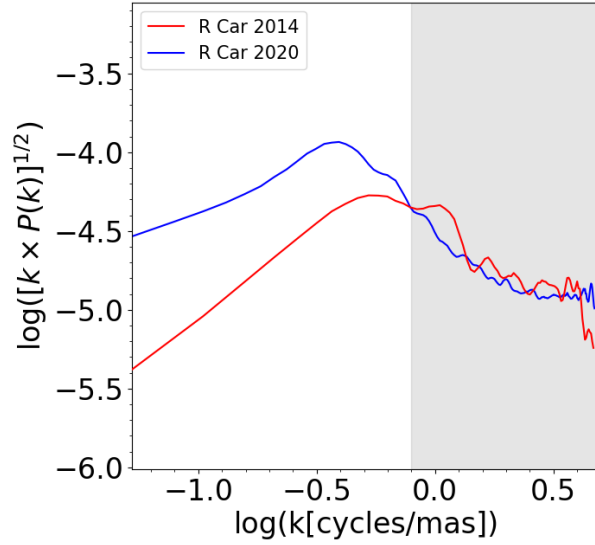


Figure 3.4: Radial averaged power spectra of the reconstructed images. The red and blue lines show the logarithm of the radial averaged power spectrum versus the logarithm of the spatial frequencies (in cycles/mas) of the 2014 and 2020 data, respectively. We applied a vertical shift of 0.5 to the 2020 powerspectra for better visualization. The gray shaded area corresponds to spatial frequencies higher than the best resolution element of the interferometer.

mas ($6.82 \times 10^{10} \pm 9.59 \times 10^9$ m) for the 2014 and 2020 epochs, respectively.

The derived sizes are bigger than the effective resolution elements of both epochs. However, since the PSD of our images can be affected by the interferometer resolution and the image reconstruction process, we quantify their impact on the determination of the measured sizes of the structures. For that purpose, we simulated two models with the following setups: (i) in the first one, we created two Uniform-Disk spots with a diameter equal to the maximum angular resolution of the interferometer (1.2 mas); (ii) in the second one, we generated two Uniform-Disk spots with a diameter equal to the size of the surface structures derived from the 2020 image (1.8 mas).

We extracted the interferometric observables from these two models using the interferometric u-v coverage from the 2020 epoch. We used this epoch because those data are sparser than the 2014 one, hence, we expect bigger u-v plane systematics on the reconstructed images. We performed the reconstructions following the same process as the original data. After convolving our images with the resolution of the interferometer,

and extracting the characteristic (dominant) size of the structures in the images using the PSD analysis, we found that the sizes of the reconstructed spots were quite similar to the original diameters used in the models: 1.30 ± 0.01 mas and 1.81 ± 0.03 mas for the first and second simulated reconstructed images, respectively. The biggest effect is observed in the reconstructed image of the first model, with a difference $\Delta \sim 0.1$ mas, when the simulated spot diameter is at the maximum resolution of the interferometer. However, when the simulated spot diameter equals the minimum sizes of the structures measured, the size is properly recovered with the PSD analysis. Hence, with those tests, we confirmed that the effect of the interferometer resolution and u-v coverage do not appear to have a significant effect on the measured sizes of the bright spots in the surface of R Car with the used analysis.

3.5 Discussion

3.5.1 Sizes of the stellar disk and of the surface structures

The epochs analyzed were obtained on a time baseline larger than the pulsation period of the star, hence, are part of different pulsation cycles. However, because of the stable nature of the light-curve it is reasonable to assume that the star's properties have not changed fundamentally between the two observing epochs. In fact, the photometry of the star is remarkably similar (see Figure. 3.1). This assumption will underlie our interpretation and for the rest of the text we will speak in terms of pulsation phase rather than years of observation.

The PSD analysis shows that the diameter of the star is smaller in phase 0.78, and larger after the photometric maximum at phase 1.01. Ireland et al. (2005) made predictions of diameter variations with pulsation for the broad *H* band. The model predicts a shift between the size variation and the light-curve. The phase shift depends on the band of observation. In *H* band, the object is expected to be smaller around phase 0.8, and larger before the minimum of the pulsation phase. The computed diameters agree with this trend.

It is even more remarkable that the surface patterns are changing in size between the two pulsation phases. On average, they are smaller when the star is smaller, and larger when the star is larger. While this effect is expected from basic physics, to our knowledge, this is the first time that it is shown for the same star using images and with

a quantitative analysis such as the PSD. These recovered PIONIER-VLTI images are, thus, opening a new dimension in the study of the pulsation of stars. After several years when optical interferometry measured diameter changes through the pulsation of the AGB stars, the time and technology seems mature to measure the change in diameter of surface structures throughout the pulsation cycle.

3.5.2 Convective pattern size(s) and their correlation with the stellar parameters

Paladini et al. (2018) used interferometric observations to compare the structures on the surface of the S-type AGB star π^1 Gru with theoretical predictions derived from the mixing-length theory of convection (Ulrich 1970). Those authors used empirical relations of convective cell sizes obtained from 2D and 3D convective models calibrated with Solar cell sizes and applied to different stellar types (Freytag et al. 1997; Trampedach et al. 2013; Tremblay et al. 2013). These authors found that the convective structures on the surface of π^1 Gru were consistent with the extrapolations of those convection models, suggesting that the convective process could be similar for different stellar types across the HR diagram.

To uncover the nature of the observed bright structures on the surface of R Car, we conducted the same experiment and compared our measurements described in Sect. 3.4.3 with the extrapolations of the models used by Paladini et al. (2018). First, according to Freytag et al. (1997) (FR97 from now on), the horizontal granulation size, x_g , is related to the characteristic pressure scale height, H_p , by the following expression:

$$x_g = 10H_p, \quad (3.4)$$

where $H_p = R_{\text{gas}}T_{\text{eff}}/\mu g$, being T_{eff} the effective temperature of the star; μ the mean-molecular weight; g is the surface gravity of the star, and R_{gas} is the ideal gas constant. Eq. (3.4) could be rewritten using the following logarithmic form:

$$\log(x_{g,\text{Freytag}}) = \log(T_{\text{eff}}) - \log(\mu) - \log(g) + 0.92. \quad (3.5)$$

We calculated the predicted convective cell size of R Car using $T_{\text{eff}} = 2800$ K (McDonald et al. 2012), $R_{\text{gas}} = 8.314 \times 10^7$ erg K⁻¹ mol⁻¹ and $\mu = 1.3$ g mol⁻¹ for a non-ionized solar mixture with 70% Hydrogen, 28% Helium and 2% heavier elements

(Carroll & Ostlie 2017). To estimate $\log(g)$, we used the mass reported in Takeuti et al. (2013) of $0.87 M_{\odot}$. Considering the radii derived in Sect. 3.4.1, we estimated $\log(g)$ values of -0.241 and -0.498 for the 2014 and 2020 epochs, respectively⁴.

Second, Trampedach et al. (2013) (TRA13 from now on) define the following expression to calculate the cell size:

$$\begin{aligned} \log(x_{g,\text{Trampedach}}) &= (1.321 \pm 0.004) \log(T_{\text{eff}}) \\ &\quad - (1.0970 \pm 0.0003) \log(g) \\ &\quad + (0.031 \pm 0.036). \end{aligned} \tag{3.6}$$

The same T_{eff} and $\log(g)$ values used in Eq. 3.5 were employed for this prescription. Third, using the CIFIST grid, Ludwig et al. (2009) and Tremblay et al. (2013) (TRE13 from now on) derived the following equation for x_g :

$$\begin{aligned} \log(x_{g,\text{Tremblay}}) &= 1.75 \log[T_{\text{eff}} - 300 \log(g)] \\ &\quad - \log(g) + 0.05[\text{Fe}/\text{H}] - 1.87. \end{aligned} \tag{3.7}$$

In the latter formula we assumed for R Car solar metallicity $[\text{Fe}/\text{H}]=0$. The logarithm of the previously derived values of x_g is reported in Table 3.4. Figure 3.5 also displays the logarithm of the derived x_g for the two reconstructed images (i.e. at different pulsation phases) as well as the three prescriptions. For comparison, we plot the value of x_g reported by Paladini et al. (2018) for $\pi^1\text{Gru}$. In angular scales, the x_g from the models vary from 1 to 5 mas, being the lower and upper boundaries set by the TRE13 and TRA13 prescriptions, respectively. The x_g derived from our reconstructed images have sizes of 1.82 ± 0.16 mas and 2.51 ± 0.32 mas for the 2014 and 2020 data, respectively. This poses them in between the boundaries predicted by the models. Our highly precise measurements are only possible due to our interferometric data. It is important to highlight that the derived sizes are larger than the minimum resolution of our interferometer (1.3 mas), including the effects introduced by the image reconstruction process.

⁴Notice that we also expect a change in temperature as a function of the radius for the two phases. This effect should not be large given that the maximum variability in the H band is around 0.5 mag (Ireland et al. 2004a). However, with the actual data, we could not quantify this change, so we used the same effective temperature for the two data sets.

Table 3.4: Logarithm of the characteristic size of the patterns observed on the surface R Car.

Model	2014	2020
	$\phi \sim 0.78$	$\phi \sim 1.01$
$\log(x_{g,\text{Freytag}})$	10.49	10.75
$\log(x_{g,\text{Trampedach}})$	10.85	11.13
$\log(x_{g,\text{Tremblay}})$	10.42	10.70
$\log(x_{g,\text{PSD}})$	10.69 ± 0.04	10.83 ± 0.06

Our estimations of the characteristic size of the bright structures on the surface of R Car also follow the predicted pattern from different pulsation phases, being smaller when the star is contracted and larger when the star expands. Despite this agreement with theoretical predictions, recent 3D convection models for AGB stars suggest that convection acts in a more complex way than the FR97, TRA13, and TRE13 scale relationships suggest (see e.g., [Colom i Bernadich 2020](#)). For example, lower surface gravity implies low densities both in the atmosphere and in the outer layers of the convection zone. This effect leads to large convective velocities, which imply much more violent convection when compared with, for example, the Sun. Then, large convective velocities cause large amounts of material to overshoot above the top of the convective-unstable layers. This causes the material to cool down and become optically thick due to molecular opacities. In this case, what could be observed as bright structures on the surface of the star are not the characteristic cell sizes but the material through the gaps created between the elevated optically thick material.

This effect appears to be more important in more massive objects. For example, [Chiavassa et al. \(2011\)](#) already suggested that the radiative energy transport in RSGs is more efficient than in the Sun. RSGs are prone to higher pressure fluctuations than AGBs. As a consequence, two kinds of surface structures might appear in those kinds of stars: (i) small-scale, short-living convective features whose sizes are consistent with the models used in [Paladini et al. \(2018\)](#) and in this work, but that the interferometers can not resolve due to the (on average) more distant location of RSGs (as highlighted by [Climent et al. 2020](#)) and; (ii) large-scale, long-living features whose sizes are consistent with modified scale relationships predictions for which turbulent motions are included ([Norris et al. 2021](#); [Chiavassa et al. 2011](#)).

Still, the fact that for R Car and π^1 Gru the measured bright spot sizes are consistent with the extrapolations from the FR97, TRA13, and TRA13 scale relationships suggests that we are observing the typical convective cell sizes, probably, because both AGB stars have similar surface gravities and progenitor masses close to solar. Thus, their convective processes are more similar to the ones of the Sun, which appears not to be the case for more massive objects.

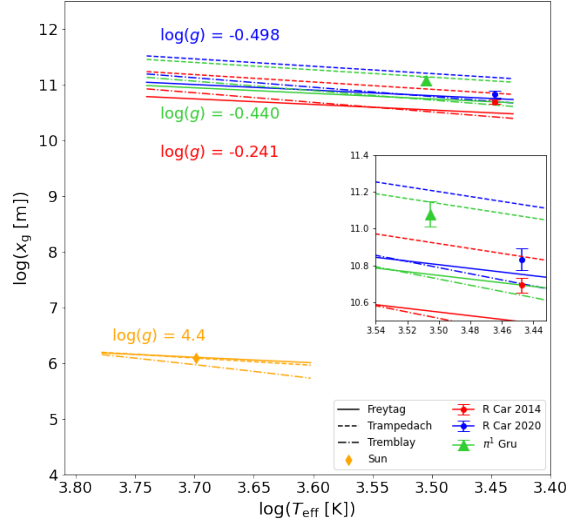


Figure 3.5: Logarithmic scale of the convective patterns (x_g) versus effective temperature (T_{eff}). The different lines correspond to the predictions of convective cell sizes from Freytag et al. (1997), Trampedach et al. (2013) and Tremblay et al. (2013) (see the labels on the plot). The blue and red circles correspond to the characteristic scale of the surface structures obtained directly from the reconstructed images of R Car, and the green triangle shows the logarithmic value of x_g reported by Paladini et al. (2018) for π^1 Gru.

3.6 Appendix: Additional figures

In this section, we show the comparison between the synthetic and observed V^2 and CPs for our 2014 and 2020 epochs (see Sect. 3.4.2). In all figures, the red dots correspond to the synthetic V^2 and CPs extracted from the reconstructed images, while the data are shown with grey dots.

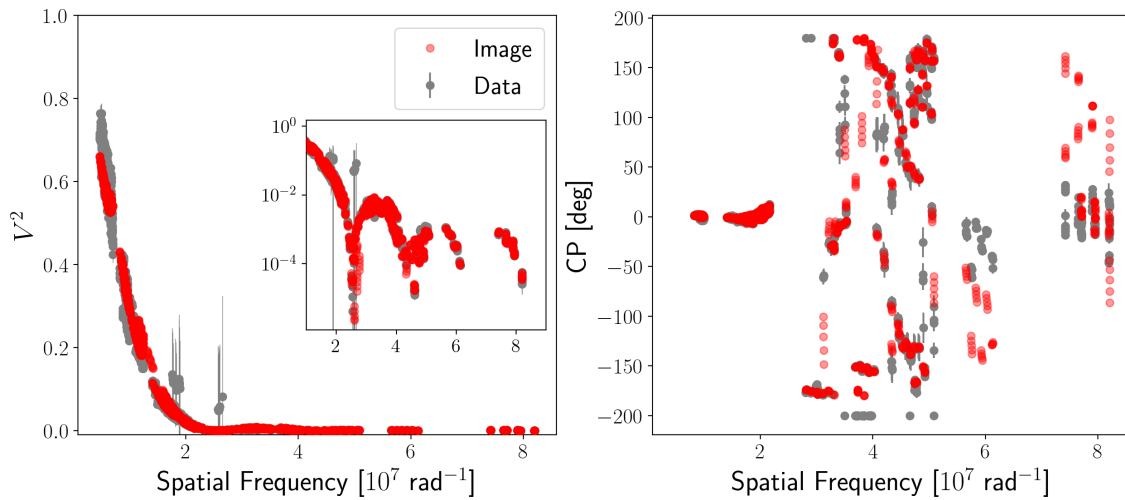


Figure 3.6: Comparison between the observables extracted from the 2014 mean reconstructed image and the V^2 (left panel) and CPs (right panel) data versus spatial frequencies. The red dots correspond to the synthetic V^2 and CPs extracted from the reconstructed images, while the data are shown with gray dots.

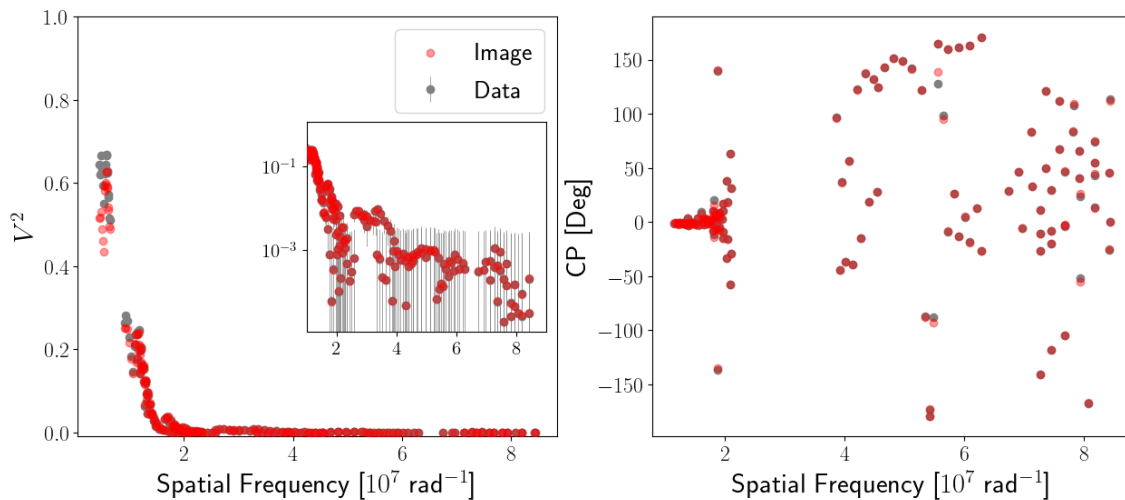


Figure 3.7: Comparison between the observables from the 2020 reconstructed image to the V^2 (left panel) and CPs (right panel) data versus spatial frequencies. The red dots correspond to the synthetic V^2 and CPs extracted from the reconstructed images, while the data are shown with gray dots.

Interferometric analysis of the M-type Mira star R Car with GRAVITY-VLTI

This chapter is based on the paper:

Imaging the innermost gaseous layers of the M-type Mira star R Car with GRAVITY-VLTI

A. Rosales-Guzmán, J. Sanchez-Bermudez, C. Paladini, A. Alberdi, W. Brandner, E. Cannon, G. González-Torà, X. Haubois, Th. Henning, P. Kervella, M. Montarges, G. Perrin, R. Schödel, M. Wittkowski, 2023, A&A 674, A62

4.1 The problem of dust and wind formation in AGB stars

When¹ low-to-intermediate-mass stars reach the AGB phase they are characterized by an inert C and O nucleus surrounded by He and H burning shells (Höfner 2008). The early-AGB phase begins with He-shell burning and subsequently evolves to a thermal pulse

¹The calibrated GRAVITY data used in this work are available at the Optical Interferometric Database of the Jean-Marie Mariotti Center (JMMC). Examples of the Python code used for optimizing the uniform disk model described in Sect. 4.3.1, the MOLsphere model in Sect. 4.3.2, the bootstrapping method described in Sect. 4.3.3, and the PCA analysis described in Sect. 4.3.3 are available to the reader in [this](#) Github repository and in the appendix of this thesis.

AGB phase where the H-shell burns. At the beginning of this phase, the atmosphere of the star is dominated by O-rich molecules (such as CO, TiO, SiO, H₂O, and VO; Wittkowski & Paladini 2014), but eventually (and depending on the mass of the star) the third dredge-up takes place, transporting the C formed in the He burning shell to the atmosphere. Depending on the efficiency of this dredge-up, the star will be of M-type ($C/O \sim 0.5$), C-type ($C/O > 1$), or an intermediate star ($0.5 < C/O < 1$) (Höfner & Olofsson 2018).

Models of dust formation in AGBs suggest that pulsations are not sufficient to form the observed outflows and mass-loss rates. However, it is believed that there is a momentum transfer due to propagating shock-waves in the atmosphere that lift gas creating density-enhanced layers around the star where the nucleation of dust can occur (Jeong et al. 2003).

The models suggest that the mechanisms for driving dust differ depending on the dust composition. C-type AGBs form amorphous carbon grains with large opacities that can be accelerated by radiation pressure (Gautschy-Loidl et al. 2004; Sacuto et al. 2011; Rau et al. 2015, 2017). For M-type AGB stars, the high chemical complexity around them makes identifying the dust grains driving the dusty winds more complex. Theoretical models of the formation of dust-driven winds in M-type AGBs suggest that the distance(s) from the photosphere to the innermost molecular layers (located at a few stellar radii) determine how far the shock waves can levitate the gas. This is strongly coupled with the condensation region that the dust of a given chemistry must be formed to produce the observed winds (Nowotny et al. 2005a; Bladh & Höfner 2012; Liljegren et al. 2016). Therefore, high-angular-resolution observations of the innermost molecular layers are particularly important to constrain the gas-dust coupling and the dust chemistry (see, e.g., Norris et al. 2012).

During the last decade, due to the enhanced spectral and spatial resolution made available, near-infrared interferometry has become an important technique to map the innermost structure of AGBs' wind in order to link the observed morphology with the mass-loss models. Most of the analyses based on interferometric data consist of model fitting the observables directly (squared visibilities - V^2 - and closure phases -CPs-) with parametric models of the star's atmosphere and/or more sophisticated radiative transfer and hydrodynamic simulations with codes like CODEX (Ireland et al. 2008, 2011) or CO5BOLD (Freytag et al. 2002, 2003). Some examples of these studies include Ireland

et al. (2004b), Wittkowski et al. (2008, 2011, 2016), and Hauboiss et al. (2015). However, due to the complexity of the environment, it is still difficult to fully reproduce the asymmetries traced by the CPs of the interferometric data with those models. Therefore, complementary techniques, such as aperture-synthesis image reconstruction can be used to better depict the inner circumstellar layers of AGB stars. Examples of interferometric imaging applied to AGB stars include the analysis presented by Wittkowski et al. (2017) on the C-rich AGB star R Sculptoris using the H band ($\lambda_0 \sim 1.76 \mu\text{m}$) beam combiner PIONIER (Le Bouquin et al. 2011) at the Very Large Telescope Interferometer (VLTI). In that study, the reconstructed images are consistent with a dynamic atmosphere and a stellar disk dominated by giant convection cells, which has a strong impact on the distribution of the molecular layers and the formation of dust at a few stellar radii.

A further example includes interferometric imaging applied to the long period variable (LPV) Mira using the Interferometric Optical Telescope Array (IOTA) in the H band, as reported by Perrin et al. (2020). In that study, a large localized absorbing patch is observed in the images. This patch is interpreted as a local dust formation zone, and it is consistent with the combined effect of pulsation and convection in the mass-loss process of AGBs (see also Paladini et al. 2018). These examples highlight the importance of interferometric imaging to confront the observed morphologies with theoretical models of dust-driven winds and mass-loss processes in AGBs. However, there is still limited observational information, in particular for the case of M-type AGBs.

In this work, we aim to characterize the innermost environment of R Car using infrared interferometry in order to link its morphology with models of the formation of dust-driven winds. For that purpose, we present new K band ($\lambda_0 = 2.2\mu\text{m}$) interferometric data obtained in 2018 with the instrument GRAVITY (Abuter et al. 2017) at the VLTI. These data were analyzed to depict the innermost structure of R Car at two phases within one pulsation cycle. Our analyses include: (i) parametric model fitting of the squared visibilities (V^2); (ii) image reconstruction of both the pseudo-continuum and across the first ($\lambda_0 \sim 2.29 \mu\text{m}$) and second ($\lambda_0 \sim 2.32 \mu\text{m}$) CO band heads; and (iii) an estimation of the CO layer(s) physical parameters such as temperature, size, and optical thickness by using a single-layer model. This chapter is structured as follows: observations and data reduction are presented in Sec. 4.2; in Section 4.3, we describe the results of our geometrical model fitting, our image reconstruction procedure, and our single-layer model. Our results are discussed in Section 4.4. Finally, we present our

conclusions in Chapter 5.

4.2 Observations and data reduction

4.2.1 GRAVITY observations and interferometric data reduction

R Car was observed in January and February², 2018 for a total of eight hours, with the beam-combiner GRAVITY. The data were collected using six baselines with the Auxiliary Telescopes (ATs) configuration A0-B2-C1-D0, which provides minimum and maximum baselines of 7.67 m (equivalent to an angular resolution of $\Delta\theta \sim 59$ mas in this wavelength range) and 32 m ($\Delta\theta \sim 15$ mas), respectively. The data cover a wavelength range between 2.0 μm and 2.4 μm with a spectral resolution of $R \sim 4000$. The complete log of observations is reported in Table 4.1.

We reduced and calibrated our data using the latest release of the GRAVITY pipeline (version: 1.5.0). Detailed descriptions of the recipes are available in the ESO pipeline [manual](#) and in (Lapeyrere et al. 2014). The same standard data reduction procedures were applied to the scientific target and the calibrator star (HD 80404; which has an angular size of 1.8 mas) to correct for the DARK, FLAT, and BAD calibrations, as well as to extract the interferometric observables. The calibrated V^2 of the target were obtained following the standard procedure described in the ESO Gravity pipeline manual, which consists of dividing the raw observables by the ones of the calibrator star. Calibrated CPs were obtained by subtracting the raw CPs of the calibrator from the ones of the source. Due to the observed changes in the observables at similar baselines, the data were split into two epochs (January and February, with equivalent pulsation phases of 0.56 and 0.66, respectively, see Fig. 4.1). The calibrated R Car data files can be downloaded directly from the Optical Interferometric Data Base (OiDB) archive hosted at the Jean-Marie Mariotti Center³.

4.2.2 GRAVITY spectrum calibration

GRAVITY data provide us with *K* band spectra ($R \sim 4000$) of the target and calibrator. For the posterior analysis of the CO band heads observed in the R Car spectrum, we calibrated and normalized it to remove the telluric contribution from the Earth's

²We also have one observation night in March but we combined it with our February data.

³<https://oidb.jmmc.fr/index.html>

Table 4.1: Log of the observations for our GRAVITY R Car data. HD80404 was selected as a calibrator star. DIT and NDIT are the Detector Integration Time in seconds and Number of Detector InTegrations, respectively. The coherence time (τ_0) was taken from the Paranal Astronomical Site Monitoring (ASM).

No.	Date	Time (UT)	Target	DIT	NDIT	Seeing (")	τ_0 (ms)
1	2018-01-27	05:30:21	R Car	3	100	0.76	5.4
2		05:42:30	R Car	3	100	0.63	5.5
3		06:25:34	R Car	3	100	0.81	5.2
4		06:37:45	R Car	3	100	0.89	6.0
5		06:51:46	HD80404	30	10	0.76	6.1
6		07:03:09	HD80404	30	10	0.99	5.8
7		07:29:58	R Car	3	100	0.73	6.3
8		07:42:04	R Car	3	100	0.67	5.0
9		07:56:18	HD80404	30	10	0.85	5.0
10		08:07:34	HD80404	30	10	0.90	4.3
11		08:22:08	R Car	3	100	0.50	4.5
12		08:34:15	R Car	3	100	0.58	4.4
13	2018-02-22	05:48:54	R Car	3	100	0.47	12.3
14		06:01:00	R Car	3	100	0.63	9.8
15		06:17:41	HD80404	30	10	0.52	8.6
16		06:29:02	HD80404	30	10	0.65	11.8
17	2018-02-25	05:35:44	R Car	3	100	0.33	11.6
18		05:47:51	R Car	3	100	0.49	10.8
19		06:02:42	HD80404	30	10	0.45	7.7
20		06:14:04	HD80404	30	10	0.55	6.2
21	2018-03-12	00:51:56	R Car	3	100	0.79	4.3
22		01:04:06	R Car	3	100	0.74	5.4
23		01:10:39	R Car	3	100	0.76	5.4
24		01:25:50	HD80404	30	10	0.74	6.0
25		01:37:13	HD80404	30	10	0.78	6.4

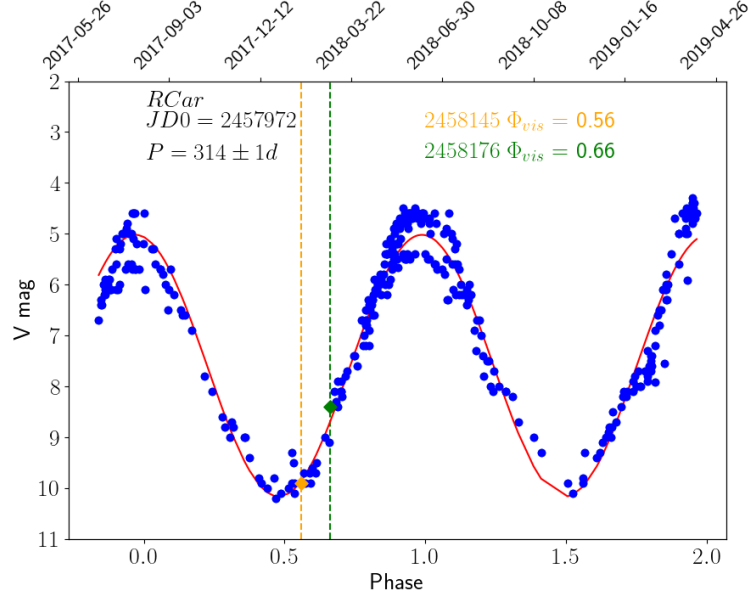


Figure 4.1: Visual light curve of R Car based on AAVSO database (blue points). The red line represents the best fit of a sine function to the curve which results in a period of $P = 314 \pm 1$ days. The dashed vertical lines and the colored diamonds show the epochs of our 2018 GRAVITY observations (see the labels on the plot).

atmosphere using the following procedure. First, we averaged the R Car and calibrator spectra to obtain the high signal-to-noise spectra $F_{\text{avg}}^{\text{RCar}}$ and $F_{\text{avg}}^{\text{HD 80404}}$, respectively. To remove the telluric lines from the averaged R Car spectrum, we used the following expression:

$$F_{\lambda}^{\text{RCar}} = \frac{F_{\text{avg}}^{\text{RCar}}}{F_{\text{avg}}^{\text{HD 80404}}} \times F_{\text{avg}}^{\text{models}}, \quad (4.1)$$

where $F_{\text{avg}}^{\text{models}}$ was calculated by averaging 15 theoretical spectra from the theoretical spectra web server ⁴(Allard et al. 2010) of our calibrator spectral type A7 Ib. Second, we flattened and normalized $F_{\lambda}^{\text{RCar}}$ (in the range of 2.21 - 2.34 μm) using a third-order polynomial function. Finally, to ensure that the CO vibro-rotational transitions are centered at their expected wavelengths, we applied a wavelength correction (equivalent to a Doppler velocity of 17 kms^{-1}) for the local standard of rest (LSR), taking into account the proper motion and the distance of the source. The normalized R Car spectrum of each epoch is presented in Fig. 4.2.

⁴<http://svo2.cab.inta-csic.es/theory/newov2/>

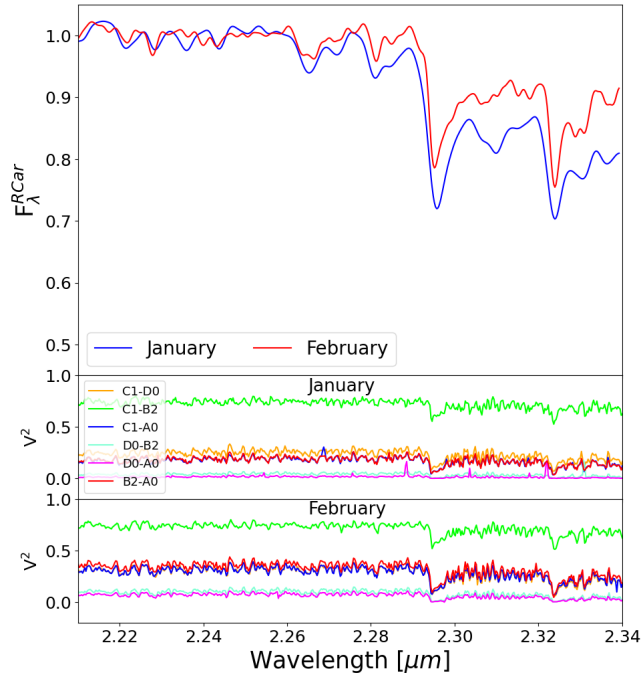


Figure 4.2: R Car calibrated spectra and V^2 . Top panel shows the normalized calibrated spectra of the GRAVITY data. The blue spectrum corresponds to the January epoch, while the red one corresponds to the February one (see the labels on the plot). The middle and bottom panels show plots of the V^2 versus wavelength for the two epochs observed. In these panels, the colors correspond to different baseline configurations.

4.3 Analysis and results

4.3.1 Geometrical model

To obtain the angular size of R Car across the K band, we applied a geometrical model of a uniform disk (UD) to the V^2 data. The visibility function of this model is given by the following equation (Berger & Segransan 2007):

$$V_{\text{UD}}(u, v) = 2(F_r) \frac{J_1(\pi\rho\Theta_{\text{UD}})}{\pi\rho\Theta_{\text{UD}}}, \quad (4.2)$$

where $\rho = \sqrt{u^2 + v^2}$, u and v are the spatial frequencies sampled by the interferometric observations, J_1 is the first-order Bessel function, and Θ_{UD} and F_r are the angular diameter of the uniform disk profile and a scaling factor that accounts for the over-resolved

Table 4.2: Best-fit parameters of the uniform disk geometrical model.

$\lambda[\mu m]$	Θ_{UD} [mas]		F_r	
	January	February	January	February
2.016	$20.44^{+0.17}_{-0.18}$	$19.00^{+0.13}_{-0.13}$	$0.808^{+0.010}_{-0.009}$	$0.842^{+0.009}_{-0.008}$
2.069	$19.71^{+0.12}_{-0.13}$	$18.14^{+0.09}_{-0.10}$	$0.910^{+0.008}_{-0.008}$	$0.908^{+0.008}_{-0.007}$
2.122	$18.37^{+0.08}_{-0.09}$	$16.59^{+0.07}_{-0.07}$	$0.940^{+0.006}_{-0.006}$	$0.932^{+0.006}_{-0.006}$
2.175	$17.36^{+0.07}_{-0.06}$	$15.39^{+0.06}_{-0.06}$	$0.954^{+0.006}_{-0.006}$	$0.942^{+0.006}_{-0.006}$
2.228	$16.67^{+0.06}_{-0.06}$	$14.84^{+0.05}_{-0.05}$	$0.964^{+0.005}_{-0.005}$	$0.948^{+0.005}_{-0.006}$
2.281	$16.97^{+0.06}_{-0.06}$	$15.41^{+0.06}_{-0.05}$	$0.945^{+0.005}_{-0.005}$	$0.931^{+0.006}_{-0.005}$
2.333	$19.12^{+0.08}_{-0.08}$	$18.18^{+0.07}_{-0.08}$	$0.932^{+0.006}_{-0.006}$	$0.923^{+0.007}_{-0.007}$
2.386	$20.83^{+0.10}_{-0.10}$	$20.18^{+0.10}_{-0.10}$	$0.928^{+0.006}_{-0.007}$	$0.915^{+0.007}_{-0.007}$

flux in the observations, respectively. Prior to modeling the pseudo-continuum data, we averaged 200 spectral bins into one single measurement. This allowed us to obtain eight spectral channels across the $2.0 \mu m$ - $2.4 \mu m$ range. Considering the calibration error in the averaged quantities, the final precision of the V^2 is $\sigma_{V^2} \sim 0.01$ and the precision of the CPs σ_{CP} is ~ 1 deg. Figure 4.3 shows the calibrated V^2 and CPs as well as the u-v coverage of the two epochs of observation for the eight spectral channels probed.

To fit the data, we used a Markov chain Monte Carlo (MCMC) algorithm based on the Python package `emcee` (Foreman-Mackey et al. 2013). We let 250 walkers evolve for 150 steps using the data of each spectral bin independently. Table 4.2 shows the best fit of Θ_{UD} and F_r for each one of the observed epochs. Figure 4.4 shows the V^2 data and their corresponding best-fit models. Figure 4.5 shows the evolution of the best-fit Θ_{UD} versus wavelength of the two epochs of observation. From this figure, we observe two significant changes in the pseudo-continuum structure of R Car.

First, the size of the target changes with wavelength, decreasing as we move toward the center of the bandpass ($\lambda \sim 2.23 \mu m$) and then increasing again. This trend is expected due to the presence of molecules such as H_2O at $\sim 2 \mu m$ and CO at ~ 2.29 - $2.33 \mu m$ lying above the stellar surface (see, e.g., Wittkowski et al. 2008). The smallest Θ_{UD} value (at $\sim 2.23 \mu m$) corresponds to the pseudo-continuum-emitting region due to

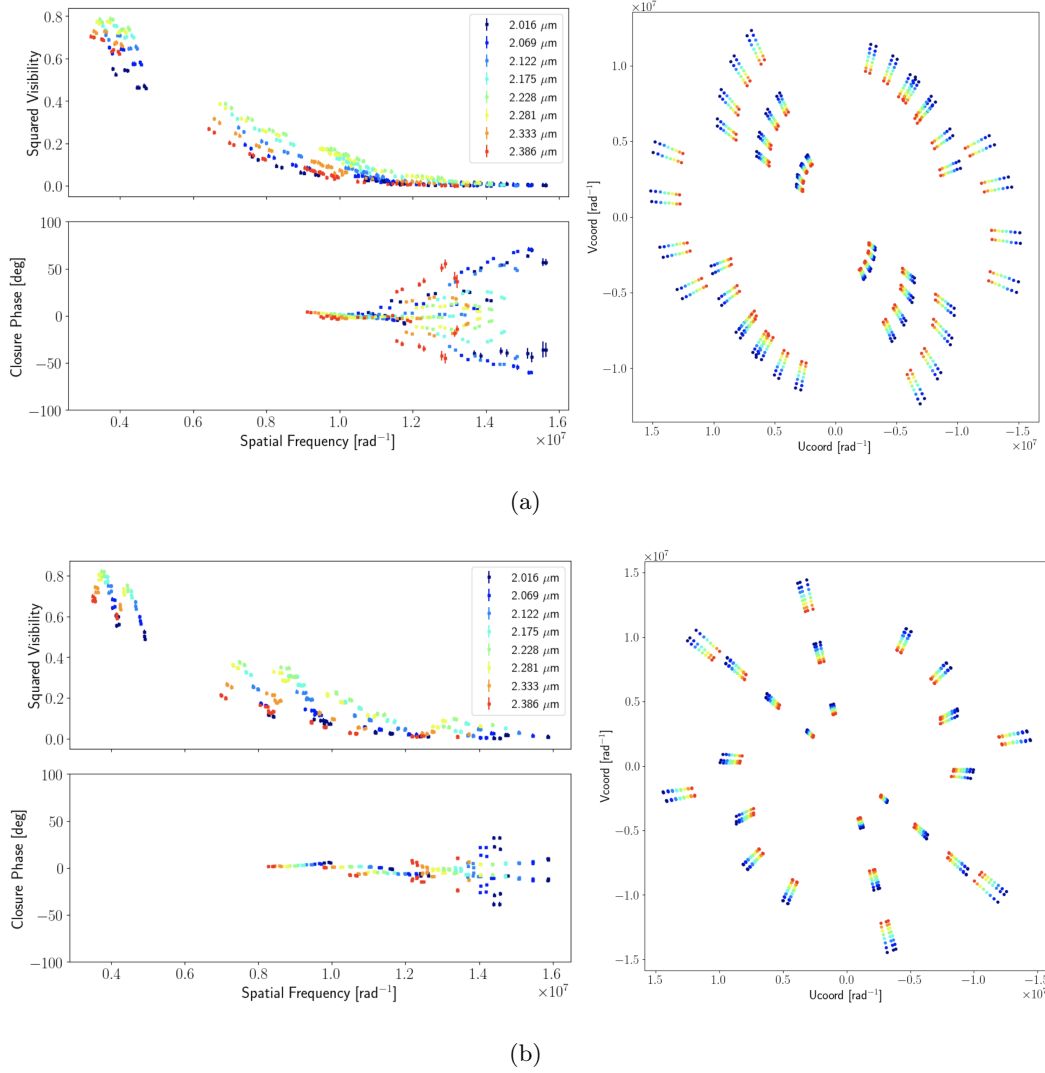


Figure 4.3: GRAVITY calibrated interferometric observables. The left plot shows the V^2 and CPs plotted versus spatial frequencies for the data sets collected and the right one shows the corresponding u-v coverage. Panel (a) corresponds to the January epoch, while panel (b) corresponds to the February one. The colors in the plots show the different wavelengths (see the labels on the plot).

the photosphere. This size is the best estimate of the stellar disk diameter in the K band. Ireland et al. (2004b) derived a wavelength-dependent Gaussian full width at half maximum (FWHM) between 15 and 20 mas at 700-920 nm. Our best-fit UD diameter at $\sim 2.23 \mu\text{m}$ indicates that the star appears to be larger near the V band than in the K

band. This size difference is due to the presence of dust layers obscuring the stellar-disk in the V band, but that are transparent in the K band, allowing us to have a closer look at the continuum-emitting region.

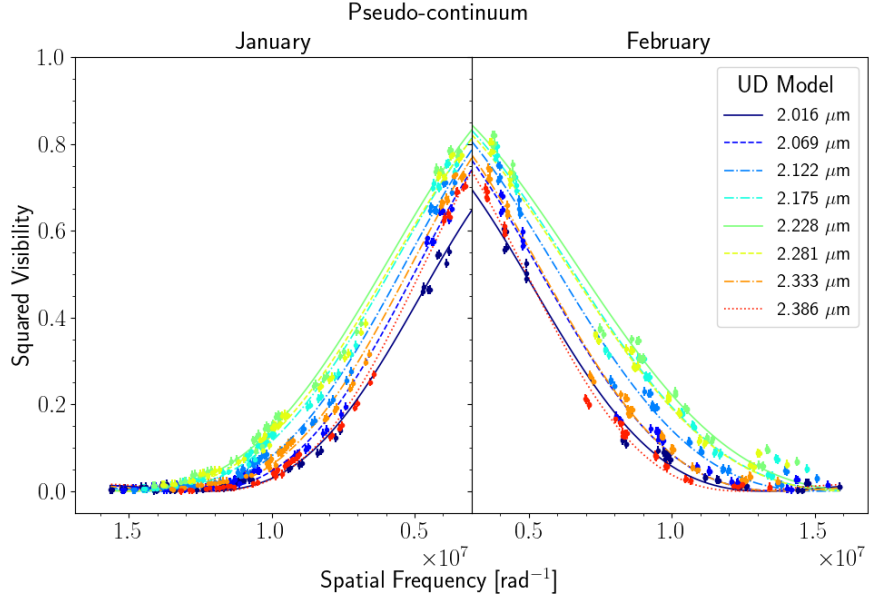


Figure 4.4: V^2 of the pseudo-continuum versus spatial frequencies for both epochs. The lines indicate the best-fit UD models. Each color corresponds to a different wavelength (see the label on the plot). We highlight that the spatial frequencies increase in opposite directions depending on the epoch. This allowed us to have a better visual comparison of the trends present in the V^2 data between the two epochs.

Second, the disk diameter is larger during the January epoch by up to 12% compared with the February epoch. From the light curve reported in Fig. 4.1, it can be observed that the V magnitude of the star increased in the February epoch, when the diameter of the star is smaller. This behavior comes with an expected increment of the temperature during February, which makes the star look brighter at the cost of it having a smaller radius (see, e.g., Wittkowski et al. 2012, 2018; Haubois et al. 2015). A rough estimate of the temperature difference (T_J/T_F) between the observed epochs could be obtained using the Steffan-Boltzmann law and the magnitude difference ($|\Delta V_{\text{mag}}| = 1.8$) from Fig. 4.1, resulting in $T_{\text{January}}/T_{\text{February}} \sim 0.62$.

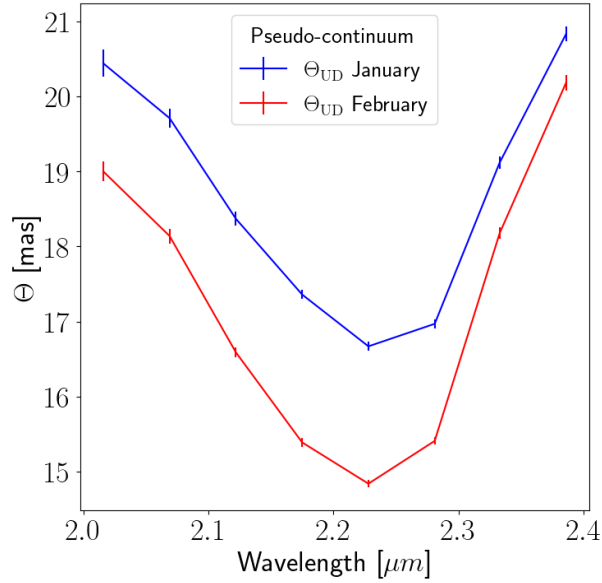


Figure 4.5: Best-fit Θ_{UD} as a function of wavelength for the two analyzed epochs. Each color corresponds to a different epoch (see the labels on the plot).

4.3.2 Spherically thin layer: MOLsphere model

The GRAVITY spectra show prominent CO band heads (see Fig. 4.2). The data show drops in the V^2 of the CO 2-0 ($\lambda_0 \sim 2.2946 \mu\text{m}$) and CO 3-1 ($\lambda_0 \sim 2.3240 \mu\text{m}$) vibrational transitions compared with the pseudo-continuum, which indicates that the CO line-emitting region is more extended (see, e.g., Wittkowski et al. 2012). The innermost CO layers are important to trace the dust nucleation region since most of the carbon or oxygen present in the atmosphere is concentrated in the stable bound of this molecule (Höfner & Olofsson 2018).

To characterize the regions where these transitions originate, we employed a single-layer model (called MOLsphere) that has proven to be successful in explaining the absorption of the CO molecule that appears in the visibilities of evolved stars (Perrin et al. 2004, 2005; Montargès et al. 2014; Rodríguez-Coira et al. 2021). This model consists of a stellar disk with a compact layer around it. The star is modeled by a stellar surface of radius R_* that emits as a black body at a temperature of T_* . It is surrounded by a compact spherical layer with a radius of R_L that absorbs the radiation emitted by the star and re-emits it like a black body. The MOLsphere is characterized by its temperature,

T_L , radius, R_L , and its optical depth, τ_λ . The region between the stellar photosphere and the layer is assumed to be empty (see Fig. 4.6 for a sketch of the model). The analytical expression of the model is given by

$$I_\lambda^r = \begin{cases} B_\lambda(T_*)e^{(-\tau_\lambda/\cos\theta)} \\ + B_\lambda(T_L)[1 - e^{(-\tau_\lambda/\cos\theta)}] & \text{if } r \leq R_* \\ B_\lambda(T_L)[1 - e^{(-2\tau_\lambda/\cos\theta)}] & \text{if } R_* < r \leq R_L \\ 0 & \text{otherwise,} \end{cases}, \quad (4.3)$$

where $I_\lambda^r = I_\lambda^r(T_*, T_L, R_*, R_L, \tau_\lambda)$; T_* and T_L are the temperatures of the photosphere and of the CO layer, respectively; R_* and R_L are the angular radius of the star and the layer, respectively; τ_λ is the optical depth of the molecular layer at wavelength λ ; $B_\lambda(T)$ is the Planck function (at wavelength λ and temperature T); and β is the angle between the radius vector and the line-of-sight so that $\cos \beta = \sqrt{1 - (r/R_L)^2}$.

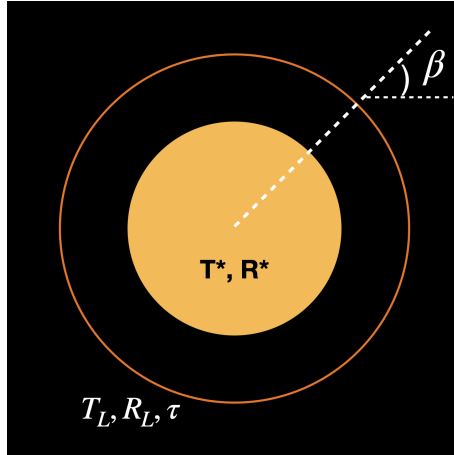


Figure 4.6: Illustration of single-layer model. The yellow disk represents the star, and the orange ring represents the layer. The parameters in the image are as described in Sect. 4.3.2. This image was adapted from Rodríguez-Coira et al. (2021).

For the fitting, we adopted a $T_*=2800$ K and $R_*=5$ mas (Monnier et al. 2014; McDonald et al. 2012). We used the disk estimation reported in the *H* band because it is considerably less affected by molecular contribution, in contrast with the *K* band where molecules such as CO, H₂O, and OH, among others (see, e.g., Wittkowski et al.

2018; Paladini 2011), are present over the entire band. The unknown parameters are then T_L , R_L , and τ_L . We performed a two-step procedure to estimate these parameters. As a first step, for each pair of T_L and R_L , we performed a least-squares minimization to find the best-fit value of τ_L that reproduces the spectrum F_λ^{RCar} . The next step consisted of using an MCMC method based on the Python library `emcee` to estimate the best combinations of T_L , R_L , and τ_L that reproduce the V^2 .

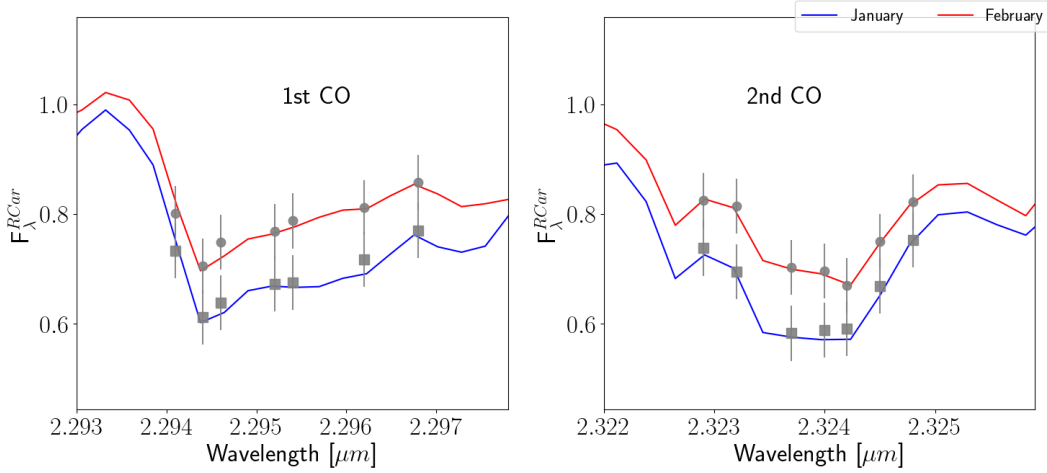


Figure 4.7: Best fit to spectra with the single-layer model for the two CO band heads and epochs. The gray dots correspond to the data points and the solid-lines correspond to the best-fit model (see the labels on the plot).

To account for the over-resolved flux when modeling the V^2 data, we added a scaling factor of Fr . This value was estimated simultaneously with the other parameters in the model. Table 4.3 shows the corresponding results for the good quality spectral channels across the two CO band heads. Figures 4.7 to 4.8 4.9 show the best fit to R Car’s spectra and V^2 obtained with the single-layer model. From the best-fit models, we derive a temperature range between 1300 and 1500 K, which is consistent with the expected temperature values to produce the CO vibro-rotational transitions observed in the K band (Geballe et al. 2007). The values of the optical depth, τ_L , support that the layer is optically thick across all the spectral channels, with higher τ_L toward the centers of the band heads. In Section 4.4, we discuss the implications of these results in the context of the wind-driving dust candidates that can coexist with the CO.

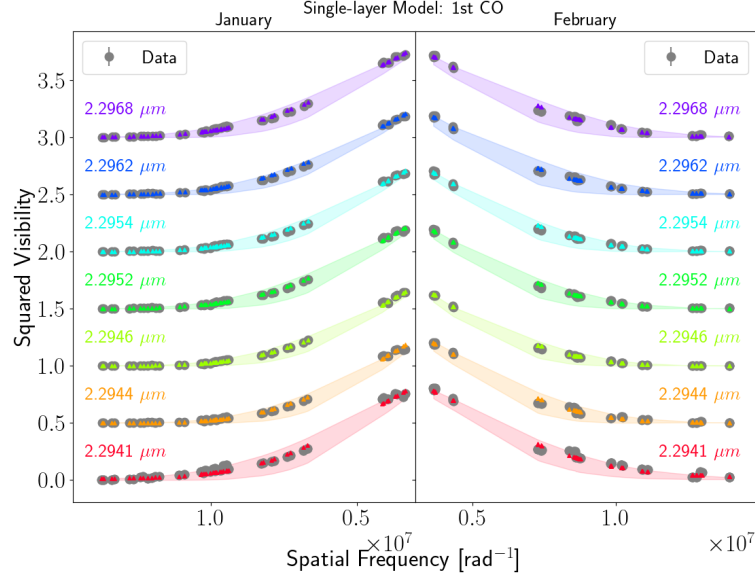


Figure 4.8: Best fit to V^2 from the best single-layer models across the first CO band head for our two epochs. The colored dots and the shaded regions correspond to the best-fit models and their corresponding error-bars. Each color correspond to a different wavelength (see labels on the plot). The data are shown with gray dots. We highlight that the spatial frequencies increase in opposite directions depending on the epoch. This allowed us to have a better visual comparison of the trends present in the V^2 data between the two epochs. Also, for better visualization, we displaced the V^2 vertically.

4.3.3 Image reconstruction

Regularized reconstructed images

The geometrical model described in Sect. 4.3.1 and the MOLsphere model in Sect. 4.3.2 show that the source is symmetric. However, the CPs observed in our data differ considerably from zero or 180 degrees, which indicates that the source is asymmetric (see Fig. 4.3). So, in order to depict the complex nature of the source across the *K* band and at the CO band heads, we reconstructed aperture-synthesis images using the software BSMEM (Baron & Young 2008). This code uses an iterative regularized minimization algorithm of the following form:

$$f(\mathbf{x}) = f_{\text{data}}(\mathbf{x}) + \mu f_{\text{prior}}(\mathbf{x}), \quad (4.4)$$

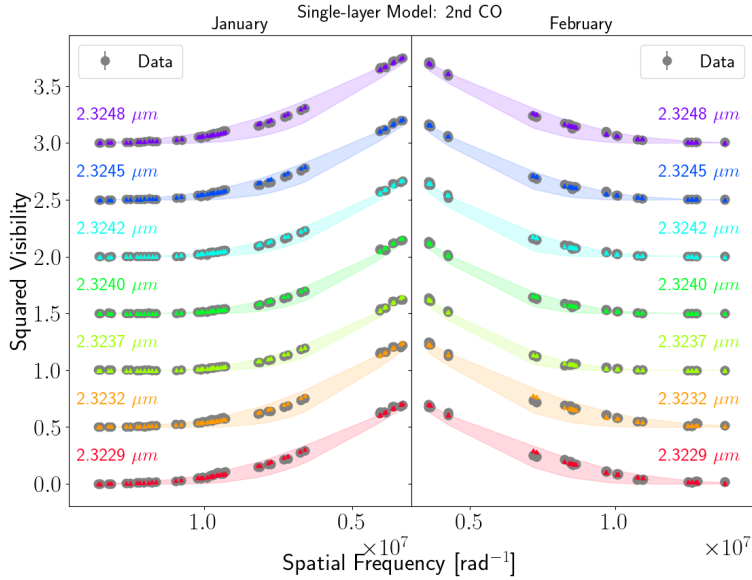


Figure 4.9: Best fit to V^2 from the best single-layer models across the second CO band head for our two epochs. The panels are as described in Fig. 4.8.

where $f_{data}(\mathbf{x})$ is a measurement of the log-likelihood and it characterizes the discrepancy between the image model (at a given iteration) and the observables; $f_{prior}(\mathbf{x})$ contains the prior information included in the reconstruction, and the hyperparameter μ is used to adjust the relative weight of the constraints between the measurements and the ones set by the priors (Renard et al. 2011). BSMEM uses Entropy (Gull & Skilling 1984) as regularizer in $f_{prior}(\mathbf{x})$.

As initial setup for our reconstruction, we created images of 128×128 pixels with a pixel scale of 0.469 mas. The best-fit sizes of the UD models were used as starting point in the reconstruction process. We performed the reconstructions by taking all the V^2 and CPs on each individual channel separately. Since our data are constrained by a relatively sparse u-v coverage, this could affect the quality of the reconstructed images. Therefore, to properly distinguish intrinsic astrophysical features from image reconstruction artifacts (Haubois et al. 2015; Sanchez-Bermudez et al. 2018) and to provide an estimate on the quality of our reconstructed images, we employed a bootstrapping method (Zoubir & Iskander 2004).

We built new data samples from the original one. The samples were created by keeping the original number of data points unaltered, but allowing random sampling

Table 4.3: Parameters of the single-layer model for the two CO band heads and our two epochs.

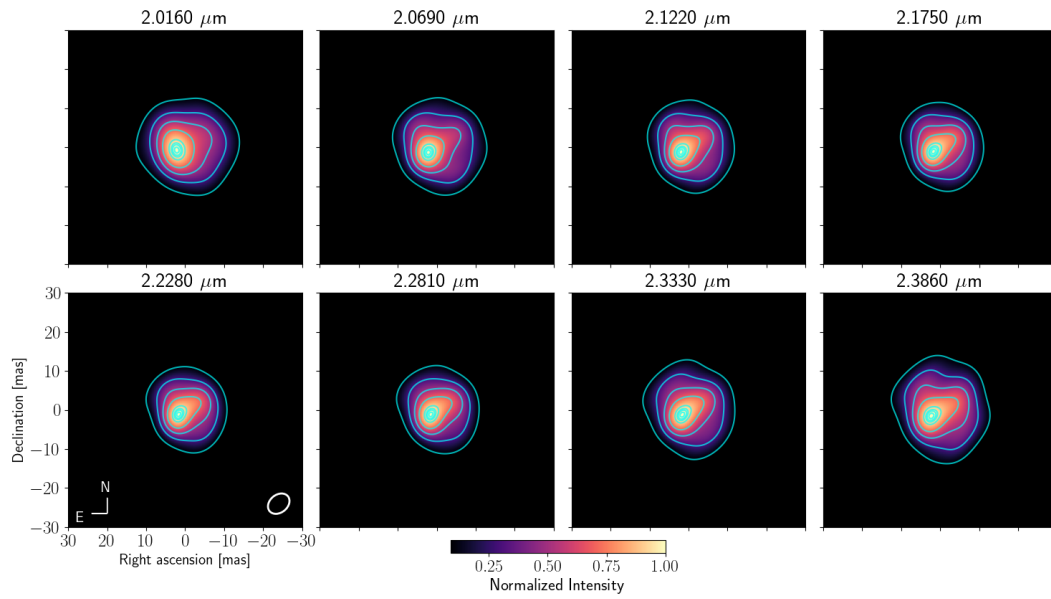
$\lambda[\mu m]$	T_L [K]	R_L [mas]	τ_L	Fr	T_L [K]	R_L [mas]	τ_L	Fr
	January				February			
CO 2-0								
2.2941	1316^{+136}_{-73}	$13.02^{+1.33}_{-1.73}$	$1.3^{+0.3}_{-0.6}$	$0.968^{+0.029}_{-0.030}$	1320^{+94}_{-60}	$12.61^{+1.09}_{-1.27}$	$0.9^{+0.2}_{-0.5}$	$0.973^{+0.024}_{-0.018}$
2.2944	1344^{+90}_{-105}	$12.41^{+1.65}_{-1.05}$	$1.9^{+0.5}_{-0.8}$	$0.976^{+0.028}_{-0.029}$	1366^{+120}_{-90}	$12.38^{+1.35}_{-1.28}$	$1.6^{+0.5}_{-0.6}$	$1.005^{+0.033}_{-0.024}$
2.2946	1360^{+106}_{-90}	$12.17^{+1.22}_{-1.21}$	$1.9^{+0.6}_{-0.9}$	$0.944^{+0.027}_{-0.029}$	1413^{+103}_{-117}	$12.12^{+1.60}_{-1.09}$	$1.7^{+0.6}_{-0.8}$	$0.956^{+0.031}_{-0.032}$
2.2952	1358^{+128}_{-84}	$12.22^{+1.25}_{-1.34}$	$1.6^{+0.5}_{-0.8}$	$0.981^{+0.030}_{-0.026}$	1413^{+129}_{-96}	$11.95^{+1.26}_{-1.24}$	$1.5^{+0.6}_{-0.8}$	$0.981^{+0.025}_{-0.019}$
2.2954	1389^{+95}_{-83}	$11.90^{+1.15}_{-1.02}$	$1.7^{+0.5}_{-0.6}$	$0.976^{+0.031}_{-0.026}$	1406^{+108}_{-83}	$12.07^{+1.26}_{-1.03}$	$1.4^{+0.4}_{-0.6}$	$0.989^{+0.028}_{-0.022}$
2.2962	1448^{+92}_{-111}	$11.28^{+1.23}_{-0.83}$	$1.7^{+0.6}_{-0.9}$	$0.962^{+0.026}_{-0.025}$	1394^{+195}_{-88}	$12.23^{+1.39}_{-1.78}$	$1.2^{+0.4}_{-0.7}$	$0.976^{+0.029}_{-0.033}$
2.2968	1424^{+148}_{-93}	$11.69^{+1.17}_{-1.30}$	$1.4^{+0.4}_{-0.7}$	$0.987^{+0.023}_{-0.024}$	1504^{+171}_{-126}	$10.95^{+1.44}_{-1.18}$	$1.3^{+0.4}_{-0.7}$	$0.972^{+0.022}_{-0.023}$
CO 3-1								
2.3229	1420^{+123}_{-94}	$11.41^{+1.19}_{-1.05}$	$1.5^{+0.5}_{-0.7}$	$0.958^{+0.026}_{-0.022}$	1467^{+159}_{-119}	$11.04^{+1.33}_{-1.20}$	$1.2^{+0.4}_{-0.7}$	$0.960^{+0.021}_{-0.025}$
2.3232	1316^{+131}_{-75}	$12.90^{+1.43}_{-1.45}$	$1.5^{+0.3}_{-0.6}$	$1.010^{+0.027}_{-0.030}$	1406^{+152}_{-100}	$11.79^{+1.42}_{-1.40}$	$1.2^{+0.3}_{-0.6}$	$0.996^{+0.024}_{-0.025}$
2.3237	1309^{+82}_{-76}	$12.78^{+1.20}_{-1.07}$	$2.1^{+0.5}_{-0.7}$	$0.958^{+0.032}_{-0.033}$	1336^{+86}_{-73}	$13.33^{+1.18}_{-1.09}$	$1.9^{+0.5}_{-0.7}$	$0.990^{+0.028}_{-0.026}$
2.3240	1315^{+81}_{-86}	$12.67^{+1.30}_{-1.09}$	$2.1^{+0.6}_{-0.8}$	$0.969^{+0.030}_{-0.035}$	1351^{+102}_{-79}	$12.80^{+1.31}_{-1.15}$	$1.8^{+0.5}_{-0.7}$	$0.971^{+0.034}_{-0.027}$
2.3242	1330^{+91}_{-81}	$12.18^{+1.15}_{-1.07}$	$1.9^{+0.6}_{-0.8}$	$0.960^{+0.027}_{-0.027}$	1352^{+116}_{-110}	$12.55^{+1.88}_{-1.29}$	$1.8^{+0.5}_{-0.9}$	$0.981^{+0.034}_{-0.037}$
2.3245	1394^{+112}_{-113}	$11.52^{+1.51}_{-1.07}$	$1.7^{+0.6}_{-0.7}$	$0.964^{+0.026}_{-0.025}$	1401^{+122}_{-106}	$12.02^{+1.39}_{-1.17}$	$1.5^{+0.5}_{-0.8}$	$0.969^{+0.024}_{-0.024}$
2.3248	1393^{+132}_{-88}	$11.83^{+1.24}_{-1.26}$	$1.4^{+0.4}_{-0.6}$	$0.995^{+0.025}_{-0.024}$	1452^{+142}_{-104}	$11.45^{+1.25}_{-1.15}$	$1.3^{+0.4}_{-0.6}$	$0.979^{+0.021}_{-0.022}$

with replacement. This created data sets with points with higher weights than in the original data set and some others with zero weights. This algorithm also produces slight changes in the u-v plane, which allows us to trace the impact of the u-v coverage on the reconstructed images, without losing the statistical significance of the original number of data points. According to [Babu & Singh \(1983\)](#), the statistical moments such as mean, variance, and standard deviation of the bootstrapped samples are good approximations to the statistical moments of the original data sets.

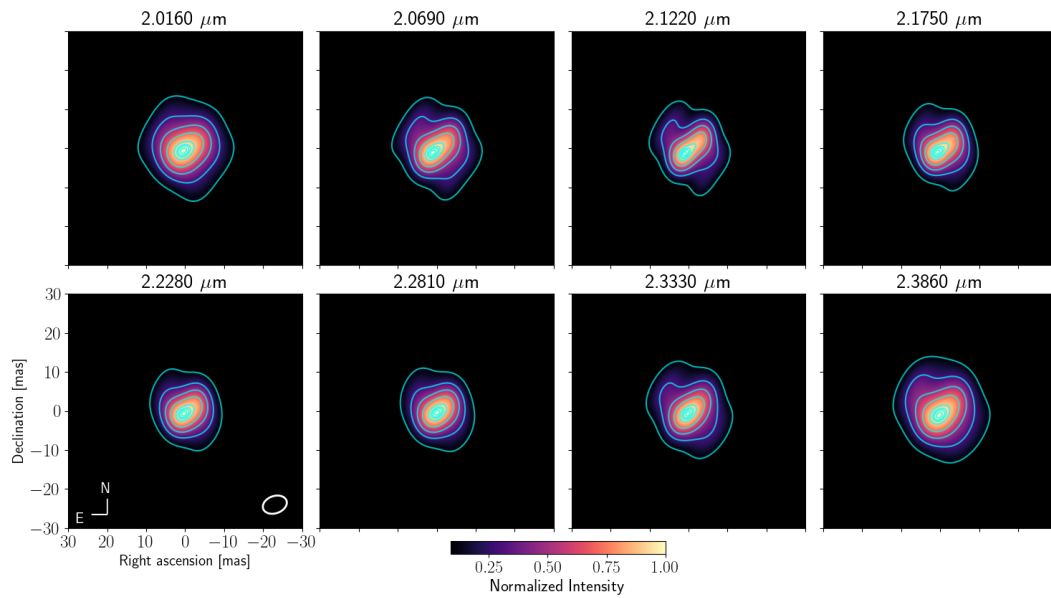
We employed this method by creating 50 different sampled data sets from the original

observables, $\mathbf{V}^{2*} = \mathbf{V}_1^2, \dots, \mathbf{V}_{50}^2$ and $\mathbf{CP}^* = \mathbf{CP}_1, \dots, \mathbf{CP}_{50}$, using the Python `scikit learn` package (Pedregosa et al. 2011). We performed image reconstructions on each sample to obtain a set of bootstrapped images: $I^* = I_1, \dots, I_{50}$. All the reconstructions from the samples converged, and the best-fit image reproduces the trend in the sampled observables (V^2 and CPs) quite well. We calculated the mean and standard deviation per pixel along the 50 bootstrapped images to obtain a mean image I_{mean} and a standard deviation map I_{σ} . We used $I_{\text{mean}}/I_{\sigma}$ to estimate the signal-to-noise ratio (S/N) of the structures present in the mean image. We removed from the images all the features with an $S/N < 3$ as they are related to reconstruction artifacts. Figs. 4.10 - 4.12 show the I_{mean} images for the pseudo-continuum and CO band head channels recovered. All the observed structures in the I_{mean} images lie within the three S/N contours. Figs. 4.20 to 4.22 show the comparison between the synthetic observables, obtained from the I_{mean} images, and the original data points. As can be seen, the trends are well-reproduced at all angular scales and wavelengths.

From a visual inspection of our best reconstructed images, I_{mean} (Figs. 4.10 - 4.12), we note that all the pseudo-continuum images are asymmetric and show structural differences between the observed epochs. In our January images, we observe a spot toward the south-east; while in February, a more elongated (and centered) structure is observed. Except the change in size across the band pass, we do not see significant structural changes with wavelength.

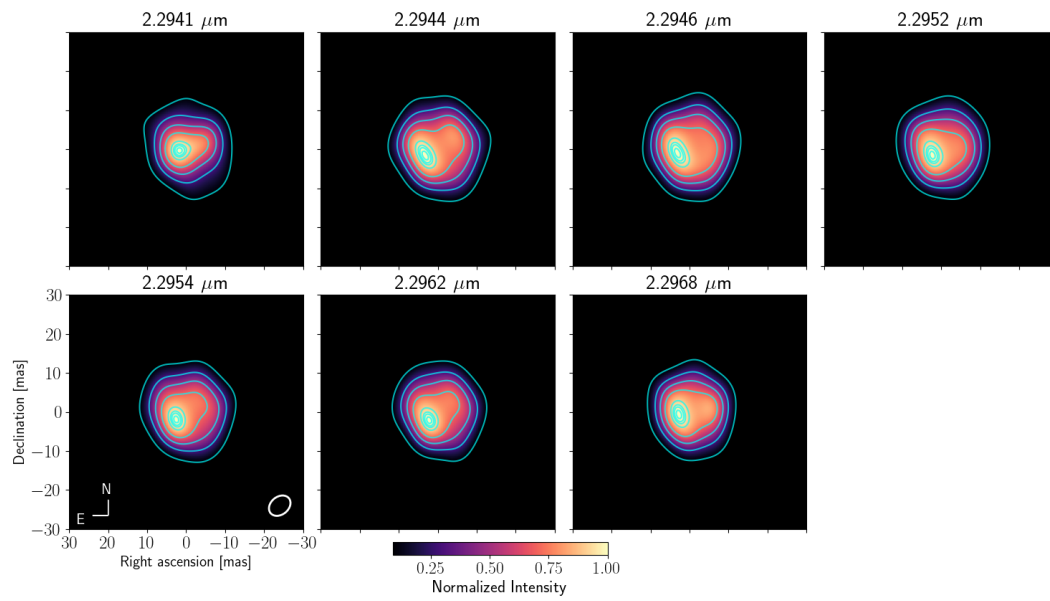


(a)

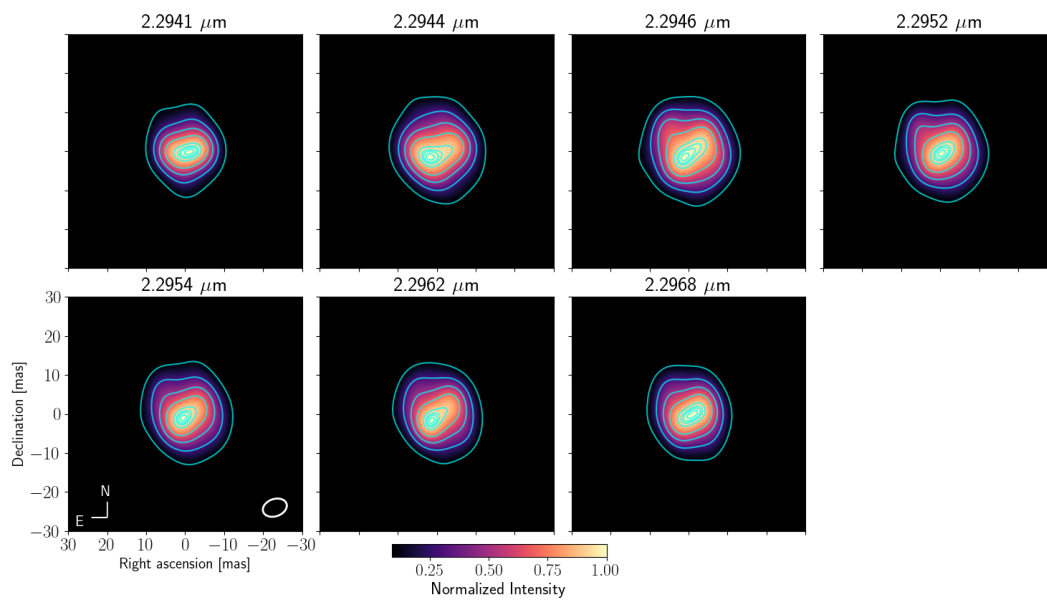


(b)

Figure 4.10: Best pseudo-continuum reconstructed images for the (a) January and (b) February epochs. The white ellipse located in the right corner of the image at $2.2280 \mu\text{m}$ corresponds to the mean synthesized primary beam. The blue contours represent 10, 30, 50, 70, 90, 95, 97, and 99 % of the intensity's peak.

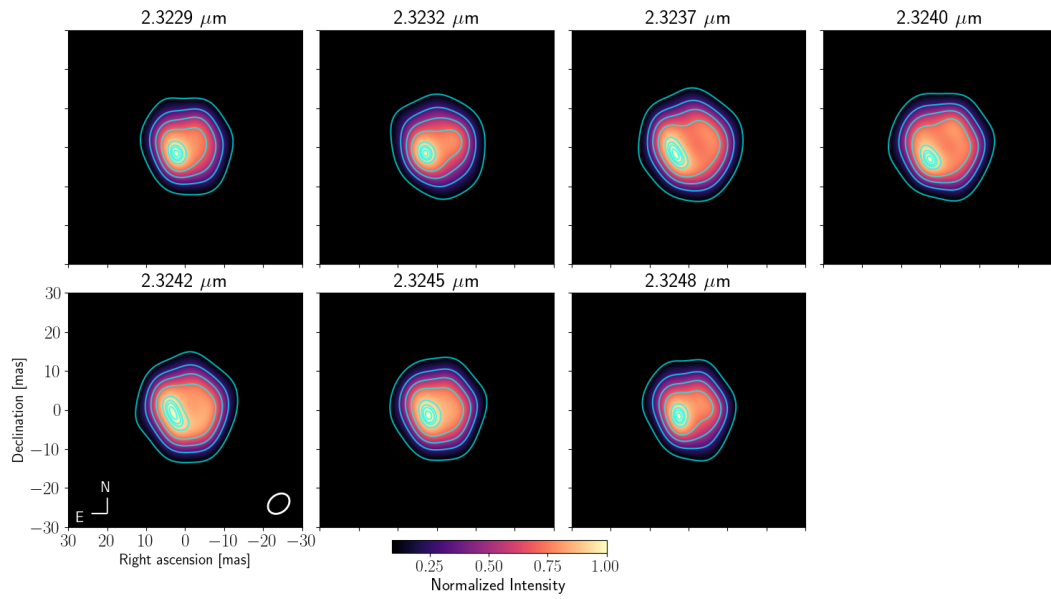


(a)

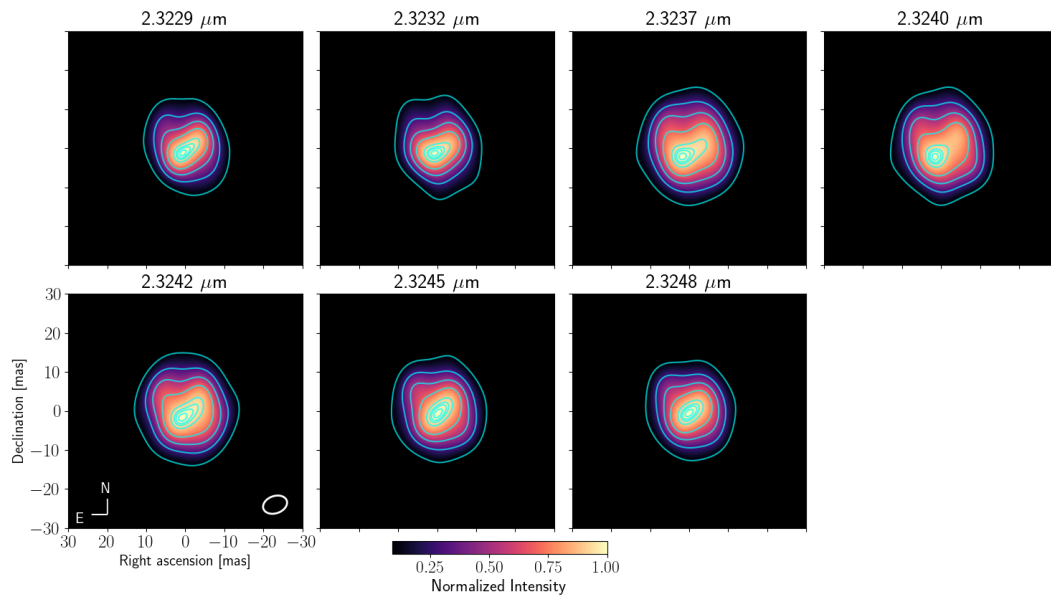


(b)

Figure 4.11: Best reconstructed images per spectral channel for the (a) January and (b) February epochs across the first CO band head. The white ellipse located at the right corner of the image at $2.2954 \mu\text{m}$ and the blue contours are as described in Figure 4.10.



(a)



(b)

Figure 4.12: Best reconstructed images per spectral channel for the (a) January and (b) February epochs across the second CO band head. The white ellipse located in the right corner of the image at $2.3242 \mu\text{m}$ and the blue contours are as described in Figure 4.10.

Principal component analysis to understand the structure of R Car

To have a more precise characterization of the asymmetries in the reconstructed images of the CO band heads, we used the principal component analysis (PCA) described by [Medeiros et al. \(2018\)](#). Those authors demonstrated that the visibilities of the principal components are equal to those of the visibilities. This method is useful for tracing the changes across a set of images that have the greatest effect on the visibility (amplitude and closure phase) profile. In our case, we estimate the most significant structural changes of the observed asymmetric structures across wavelength for each of the observed epochs. The following procedure was applied to the ensemble of wavelength-dependent images per epoch to extract their principal components.

For the PCA analysis, we normalized each data set by subtracting the corresponding mean image and dividing by their standard deviation image across the wavelength range. To perform the PCA analysis, we used the `CASSINI-PCA`⁵ package. This software allowed us to compute the covariance matrix of the data set and to transform it into the space of the principal components. This allowed us to determine the eigenvectors (or eigenimages in our case) and their corresponding eigenvalues. Since we only have seven images per data set, and the possible number of components must be smaller than or equal to the number of images in the data set, we decided to only keep the first four principal components. From our tests, we observe that those components explain, at least 93% of the variance in the data sets.

The maps that correspond to the first four principal components of the CO band heads are reported in Figs. 4.13 and 4.14. For both CO data sets, we observe that the first two components trace the variance associated with the general changes in brightness and size observed in the images of the CO band heads across wavelengths. However, components 3-4 show considerably more asymmetric changes in the external structure of the target (for contours between 50% and 10% of the peak). The observed varying structures in components 3-4 are evenly distributed across the different position angles in the structure of the source. We suspect that the variance explained by these components is associated with the more asymmetric structure in the CO images. This could also be connected with the possibility of having a clumpy CO distribution of material in the envelope around R Car. As an example of the contribution of each component to the asymmetric structure of the target, in Figure 4.15 we include the CPs obtained

⁵<https://github.com/cosmosz5/CASSINI>

at a wavelength of $2.2946 \mu\text{m}$ from the recovered images with cumulative components between 1 and 4. As can be observed, the recovered images improve the recovery of the asymmetries traced by the CPs as we add more components to them. This is an indication that the variance observed in the eigenimages is tracing a more changing environment in the CO distribution across the sampled wavelengths. Unfortunately, the limited resolution of our observations is not enough to properly resolve these asymmetries completely.

4.3.4 Pure-line CO images

Our CO reconstructed images contain a contribution associated with the underlying stellar component. To remove such contribution, we first centered the images across the CO band heads in a common reference position. For this purpose, we used the differential phases (DPs) in the GRAVITY data. DPs measure the photocenter displacement of an emission line with respect to the continuum for a given baseline length and orientation. We only restricted the pure-line CO images to the first band head, since the DPs of the second band head have much larger uncertainties. To compute the global 2D photocenter displacement vector at a given spectral channel, we used the following relation (Kraus 2012):

$$\vec{p} = -\frac{\phi_i}{2\pi} \cdot \frac{\lambda}{\vec{B}_i}, \quad (4.5)$$

where ϕ_i is the GRAVITY differential phase measured on baseline i , \vec{B}_i is the corresponding baseline vector $[B_x, B_y]$, and λ is the central wavelength of the working spectral channel. By solving the matrix represented by Eq. 4.5, we were able to find the global $[p_x, p_y]$ displacements of the emission line. We solved the system of equations employing the least-squares algorithm implemented in the Python function `numpy.linalg.lstsq`. This function inverts the matrix formed by each one of the observed differential phases per baseline per channel to find the solution of the astrometric displacements. To obtain an estimation of the precision (i.e., 1σ error-bars) of the reported displacements, we applied the same matrix inversion process to 100 different samples obtained with random points using a Gaussian distribution with a standard deviation equivalent to the error bars of the differential phases. The final astrometric displacements are equivalent to the mean of the 100 different samples, while their error bars are equivalent to the standard deviation of the displacements from the samples. We obtained the displacements for the

different spectral channels across the CO band heads, as well as for a few continuum channels. Fig. 4.16 shows the first CO band head offsets for our two epochs.

We can observe that the wavelengths corresponding to the continuum emission lie close to the reference position $[0,0]$, and the ones of the band head show displacements within 1 mas. It is interesting to highlight that the CO centroid position of the two epochs is different, confirming the variability of the structure of the source between them. Once the centroid position of the images was computed, we used them to extract the pure-line CO images using the following method. First, CPs are shift-invariant quantities, it means that images reconstructed with this observable could be placed at different positions in the pixel grid and, still, reproduce the CPs in the data. Therefore, to account for this effect, we computed the continuum and CO images, and we performed a sub-pixel shift to the corresponding centroid position obtained from the astrometric displacements $[p_x, p_y]$ of the differential phases. For the subsequent analysis, we took the continuum images at $\lambda_{cont} = 2.228 \mu m$. Second, once all the centroids of the images matched with the astrometric displacements, we subtracted the continuum image from each one of the CO images across the different spectral channels. Since the total flux in the reconstructed images is normalized to unity, before performing the subtraction we calibrated the total flux on each image by scaling them with their corresponding normalized flux scale from the spectra in Figure 4.2. Figure 4.17 shows the CO images with the continuum contribution subtracted. We masked the central region to better visualise the CO-emitting region. From a visual inspection of the images, we can identify some features. First, there are different structures between wavelengths and epochs, suggesting the inhomogeneous nature of CO. The images also show bright and faint regions at different position angles. We relate them with zones of lower (faint regions) and higher (bright regions) densities and temperatures.

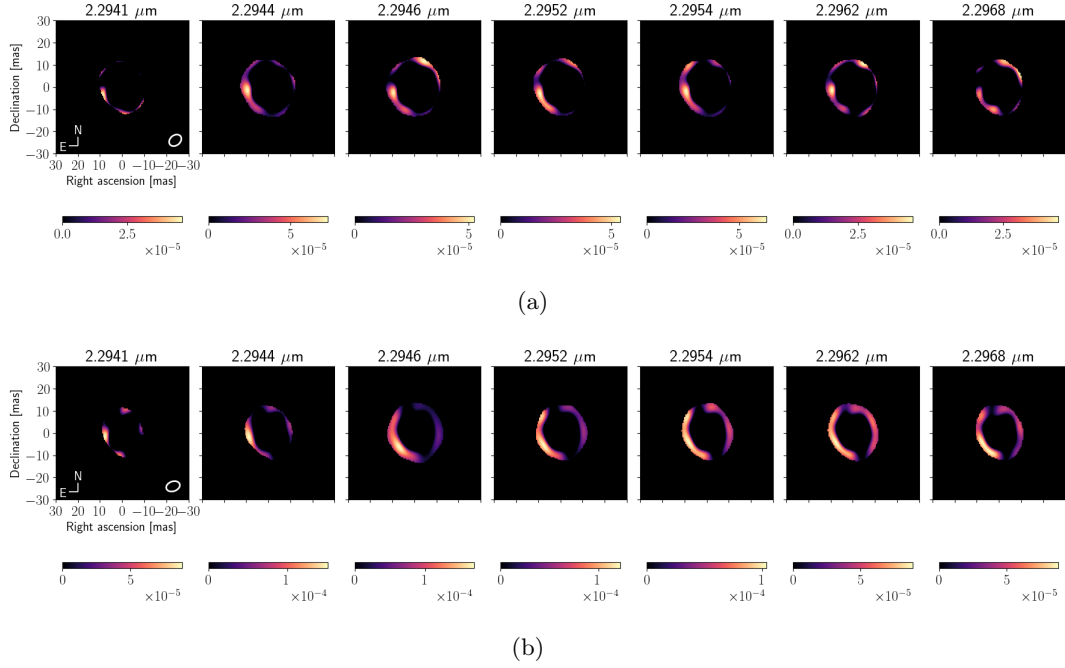


Figure 4.17: Pure-line CO images of the first CO band head for the (a) January and (b) February epochs. The region that corresponds to the subtracted continuum contribution has been masked for better visualization of the CO region. The white ellipse located in the lower right corner of the image at $2.2941 \mu\text{m}$ corresponds to the mean synthesized primary beam.

4.4 Discussion

4.4.1 CO column densities from the single-layer model

The single-layer model described in Section 4.3.2 allowed us to obtain information about the CO layer's physical conditions (e.g., opacity, temperature, and sizes). Using the optical thickness and temperature derived for the layer, we estimated the corresponding column density in units of cm^{-2} using the following relation (Savage & Sembach 1991):

$$N = \frac{\tau_L \Delta v \sqrt{\pi}}{f_{ij} \lambda_{ij} c \frac{\pi e^2}{m_e c^2}}, \quad (4.6)$$

where τ_L is the optical thickness obtained from our single-layer model, Δv is the width of the band head in km s^{-1} , f_{ij} is the absorption oscillator strength that depends on

the temperature, λ_{ij} is the wavelength of the transition, c is the speed of light, e^- is the electron charge and m_e its mass, and the constant term $\pi e^2/m_e c^2 = 8.8523 \times 10^{-13}$ cm/mol. We calculated the column density at the center of the first CO band head, where the optical thickness has its largest value, by setting $\lambda_{ij} = 2.2946 \mu m$. Then, using Eq. (3) from [Goorvitch \(1994\)](#), we calculated f_{ij} for the vibro-rotational transition $V_{0 \rightarrow 2}, J_{20 \rightarrow 21}$ (V and J are the vibrational and rotational states, respectively). We obtained their corresponding Einstein coefficients, A, from [Chandra et al. \(1996\)](#). Finally, we calculated Δv by fitting an inverse Lorentzian profile across the first CO band head for the two epochs. Since Δv is expressed in kms^{-1} , $\Delta v = c\Delta\lambda/\lambda_0$.

The obtained column densities for both epochs lie in the $N_{\text{CO}} \sim 9.19 \times 10^{18} - 1.01 \times 10^{19}$ cm^{-2} range. This result has two implications. On one side, these values are consistent with the range of column densities reported by authors including [Rodríguez-Coira et al. \(2021\)](#) and [Tsuji \(2006\)](#) for other evolved stars. Furthermore, these values, on average, are high enough to shield the dust particles allowing them to grow to micron-sized scales, where the stellar radiation could act efficiently to drive the observed winds in this kind of object. On the other side, our current single-layer model returns large uncertainties in the estimated parameters. Therefore, we cannot confirm if CO formation happened between both epochs.

To obtain a direct comparison between the size of the photosphere (R_*) and the size of the CO layer (R_L), we calculated the ratio R_L/R_* . We take the R_* value reported by [Monnier et al. \(2014\)](#) of 5 mas as a reference. From R_L/R_* , we find a mean extension of the layer $R_L \sim 2.4 R_*$. To verify the consistency of our results, we compared them with other O-rich Miras for which the single-layer model has been applied. Table 4.4 shows the values of the layer temperature and R_L/R_* for the Mira stars R Leo, χ Cyg, and T Cep, as well as for our R Car estimates. From the values reported, we confirm that the parameters derived for R Car are consistent with other estimates reported in the literature for similar type of objects.

4.4.2 Observational restrictions to the wind driving candidates for M-type Mira stars

Given the high chemical complexity around M-type AGB stars, it is not easy to determine the chemical composition of dust-driven winds. Even though observations tell us about the existence of different dust species in the circumstellar environment ([Molster et al.](#)

Table 4.4: Parameters of the single-layer model for other AGBs.

Star	T_* (K)	T_L (K)	R_L/R_*
R Leo	3856 ± 119	1598 ± 24	2.29 ± 0.19
χ Cyg	3211 ± 158	1737 ± 53	1.91 ± 0.02
T Cep	3158 ± 158	1685 ± 53	2.15 ± 0.02
R Car Jan (CO 2-0)	2800	1360^{+106}_{-90}	2.43 ± 0.20
R Car Feb (CO 2-0)	2800	1406^{+108}_{-83}	2.42 ± 0.20
R Car Jan (CO 3-1)	2800	1330^{+91}_{-81}	2.44 ± 0.20
R Car Feb (CO 3-1)	2800	1401^{+122}_{-106}	2.40 ± 0.20

Parameters of the single-layer model extracted from [Perrin et al. \(2004\)](#) for two O-rich AGB stars (R Leo and T Cep) and one S-type (χ Cyg) compared with the parameters reported in this work for the CO band heads and GRAVITY epochs analyzed.

2010), not all are efficient in absorbing or scattering the star’s radiation to trigger a stellar wind. A condition for a dust grain to be considered a wind driver is that it must be formed closer to the stellar surface within reach of shock waves produced by the star. The shortest distance from the star at which a dust grain can be formed depends on its chemical and optical properties ([Bladh & Höfner 2012](#)).

As mentioned in Sect. 4.1, the observed CO vibro-rotational transitions (with $\Delta V = 2$) originate in the deep photospheric layers where dust is forming. Therefore, with the CO layer parameters, obtained from our single-layer model and the pure-line CO images, we can set constraints on the types of dust grains that are considered wind-driving candidates and that can coexist with similar physical conditions to the CO innermost layers detected with our GRAVITY observations. It is important to remember from Sec. 1.3.2 that for winds to be triggered, the star pulsations must levitate the gas to a certain distance (defined as levitation distance, R_l , Eq. 1.6) where dust can condense (known as condensation distance, R_c , Eq. 1.5). The levitation distance can be extracted directly from the size of the layer from our single-layer model or from the pure-line CO-reconstructed images. The single-layer model provides us an average estimate of

$R_l = 2.43 R_*$, since the model only considers a symmetric structure. However, the reconstructed images provide us a range of R_l between 2.25 and 2.72 R_* due to the observed asymmetries. Assuming $u_{\text{esc}} = 44 \text{ km s}^{-1}$, $M = 0.87 M_\odot$ (Takeuti et al. 2013), $T_{\text{eff}} = 2800 \text{ K}$ (McDonald et al. 2012), and $R_* = 167 R_\odot$ (Monnier et al. 2014) for Eq. 1.6 and that the CO band heads that we observed are formed in a region from the stellar surface at $R_0 = 2 R_*$, we computed an initial velocity of the CO of $u_0 = 13 \text{ km s}^{-1}$ considering the single-layer model and u_0 between 10 and 16 km s^{-1} using the CO reconstructed images. These values are consistent with the ones reported in the literature on the order of $u_0 \sim 10 \text{ km s}^{-1}$ (Nowotny et al. 2010).

Using Eq. 1.5, we estimated the condensation radii for several types of dust grains assuming the condensation coefficients and temperatures reported by Bladh & Höfner (2012) and references therein (see Sec. 1.3.2). Considering that the levitation radius has to be larger or equal to the condensation radius, we obtained curves of possible p and T_c values with the R_l estimates from our single-layer model and pure-line CO reconstructed images.

Figures 4.18 and 4.19 show the T_c versus p , diagram. In both figures, the red dots correspond to a variety of dust grains with different condensation temperatures and values of p . The solid-black line in Fig. 4.18 displays the values of T_c and p for the R_l value obtained from the single-layer model. The colored solid lines in Fig. 4.19 correspond to the R_l values extracted from the pure-line CO images for both observed epochs at different orientations: 0° , 90° , 180° , and 270° . Since we have seven images per epoch, we adopted the median value per image data set at each orientation.

Those figures show that our CO layer radius is consistent with the condensation radius for composites Mg_2SiO_4 and MgSiO_3 . However, we find layer temperatures around $1300 \pm 100 \text{ K}$ (blue and green shaded regions on Fig.4.18), which are slightly higher than the expected condensation temperature for those two dust composites ($T_c \sim 1100 \text{ K}$). This temperature discrepancy could be explained by the fact that the single-layer model considers a homogeneous and symmetric distribution of the CO layer. However, the reconstructed images clearly show that the CO distribution is neither homogeneous nor symmetric as shown in Fig. 4.19 where, depending on the position angle, either one or both composites lie(s) below the estimated levitation radius. Therefore, regions with lower temperatures and larger levitation radii could exist around R Car. This supports the hypothesis that dust formation could occur in an anisotropic way over the CO shell

extension.

Magnesium-iron silicates (olivines and pyroxenes) with nano grain sizes ($\sim 0.1 \mu\text{as}$) have already been detected in the circumstellar environments of M-type AGB stars (Norris et al. 2012; Ohnaka et al. 2017), and they appear to be the main factor responsible for the dust-driven winds observed in these stars. While our GRAVITY observations and models suggest the possible coexistence of those dust types at the inner gaseous (CO) shells, we require additional interferometric observations in the mid-infrared (potentially with the beam-combiner MATISSE-VLTI) to confirm this scenario. Very recent models of dusty winds in M-type AGBs suggest Fe enrichment of the wind as it moves far away from the photosphere (Höfner et al. 2022). Those models suggest an inner core of Mg_2SiO_4 (or of a similar composite) surrounded by more outer layers of MgFeSiO_4 . New MATISSE-VLTI interferometric observations could help us to confirm this scenario in the proximity of R Car in the near future. By confirming this scenario, mid-infrared interferometric observations could shed new light on the problem of a lack of the $10 \mu\text{m}$ silicate feature in the spectra of M-type AGB stars.

4.4.3 The role of CO asymmetries on mass-loss estimates

The mass-loss rate is a crucial parameter for understanding the evolution of M-type AGB stars. Bladh et al. (2019) presented an extensive grid of DARWIN dynamic atmosphere and wind models to establish the mass-loss rates, wind velocities, and grain sizes for M-type AGB stars. These models assume that the principal mechanism for wind triggering is the radiation scattering on Mg_2SiO_4 composites. This grid of models produce mass-loss rates on the order of $1 \times 10^{-6} M_\odot \text{yr}^{-1}$ for stellar parameters similar to R Car (e.g., $M_* = 0.75 M_\odot$; $\log[L_*/L_\odot] = 3.55$; $P = 283$ days).

More importantly, those models show that, for the mass ($0.75 - 1 M_\odot$) and luminosity ($\log[L_*/L_\odot] = 3.7$) ranges of R Car, large values of the pulsation amplitude in the models and high chemical enrichment develop stable winds based on the Mg_2SiO_4 composites. However, there is a region (when the piston velocity, $\Delta u_p = 2 \text{ km/s}$ and $n_d/n_H = 1 \times 10^{15}$) of low chemical enrichment and small pulsation amplitudes where those DARWIN models do not develop stable dust-driven winds. While those models are important to demonstrate the dynamical evolution of dust-driven winds with chemical properties based on magnesium-iron silicates, they do not incorporate the importance of asymmetries on the development of the wind.

Liljegren et al. (2018) studied the effects of complex convective structures on wind production and mass loss in M-type AGB stars. The authors used the CO5BOLD code (Freytag et al. 2003) to simulate the convective surface and pulsations of AGBs, using the results as boundary conditions in their DARWIN models. Those models show that gas is not levitated uniformly above the star’s surface (only about 70% or less of the stellar surface is covered), causing dust not to be formed in a spherical layer around the star. Instead, it forms clumps. This appears to have a direct implication in an overestimation of the mass-loss rate determined with homogeneous models. In this context, our work shows direct evidence of the asymmetric and variable gas distribution at the innermost layers of M-type AGB stars. A specific DARWIN model of R Car is beyond the scope of this thesis and it is left for future studies. However, by contrasting the structures observed in our reconstructed images and future dedicated CO5BOLD/DARWIN models, we could obtain better constraints on the mass-loss evolution and the role of magnesium dust composites on the development of stable winds.

4.5 Appendix: Additional figures

In this section, we show the comparison between the synthetic and observed V^2 and CPs across the pseudo-continuum, the first and second CO band heads for our January and February epochs (see Sect. 4.3.3). In all figures, the red dots in the main panels correspond to the synthetic V^2 and CPs extracted from the raw reconstructed images, while the data are shown with gray dots in the main panels. The lower panels show the corresponding residuals (in terms of the number of standard deviations) coming from the comparison between the data and the best-fit reconstructed images.

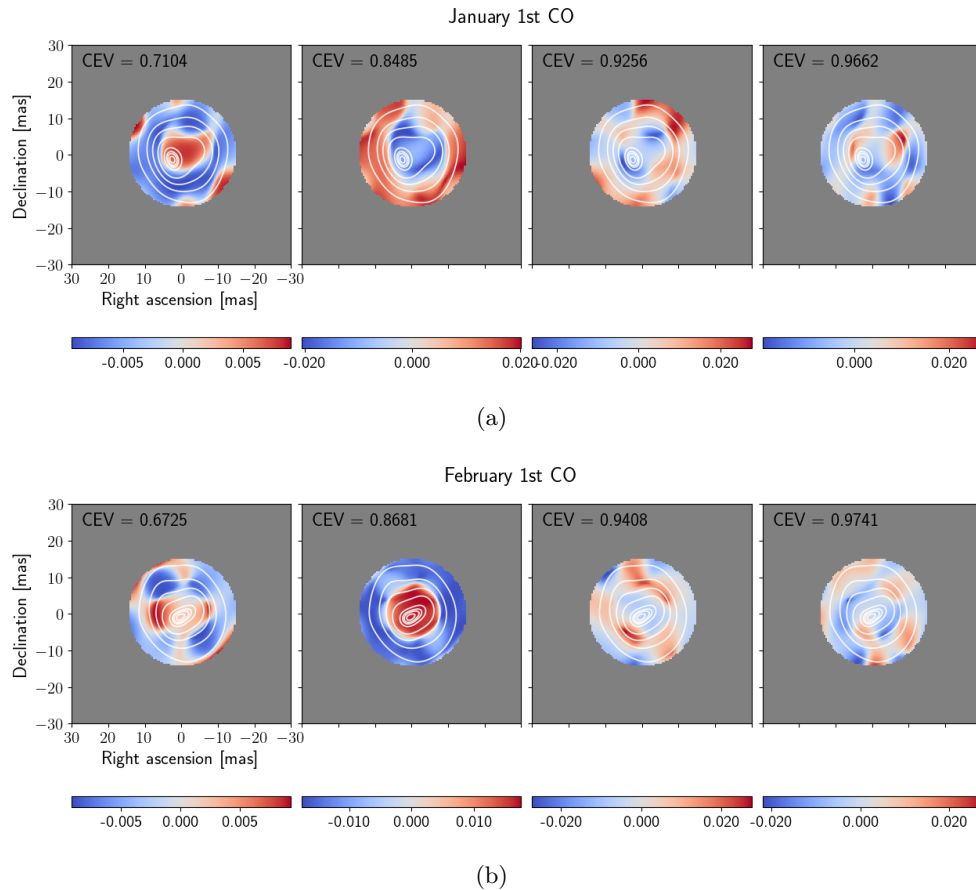


Figure 4.13: First four principal components for the January and February epochs for the first CO band head. The relative scale of the structures in the eigenimages is displayed with a color bar at the bottom of each panel. Only the central 20 mas of the eigenimages are shown in each panel. The white contours correspond to the mean image across wavelength (per given data set) and they represent 10, 30, 50, 70, 90, 95, 97, and 99% of the intensity's peak. The Cumulative Explained Variance (CEV) per principal component is located in the top left side of each panel.

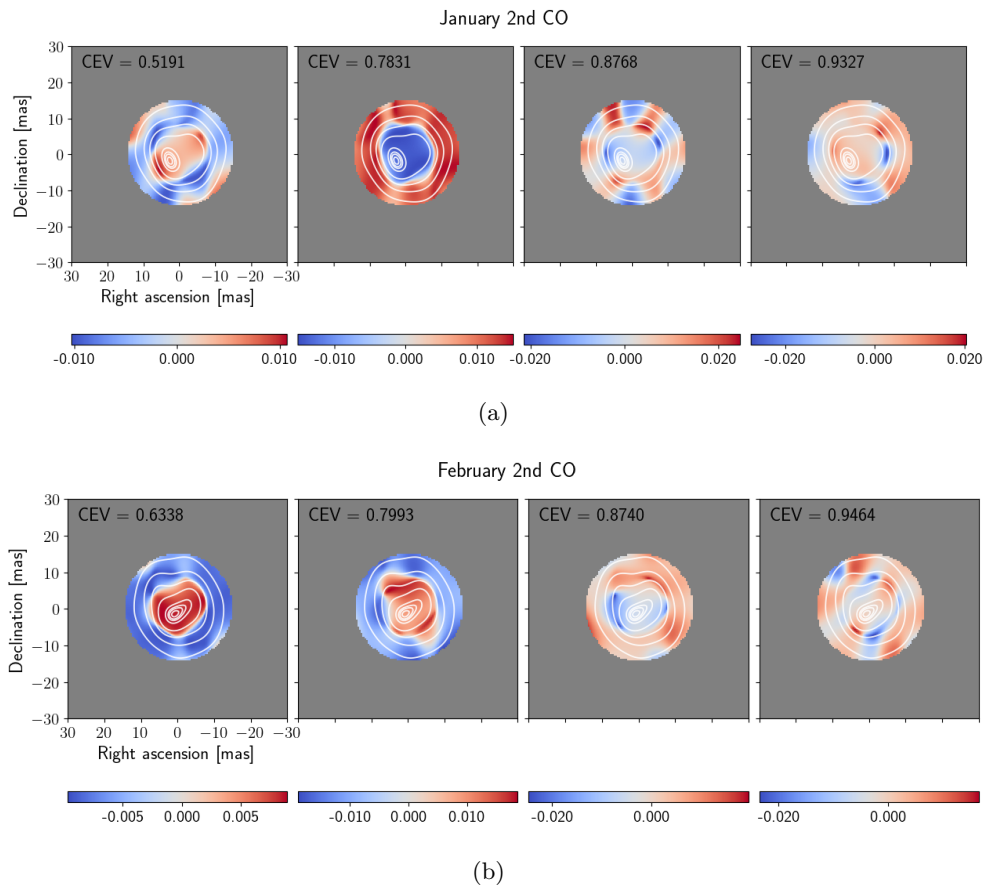


Figure 4.14: First four principal components for the January and February epochs for the second CO band head. The panels are as described in Fig. 4.13.

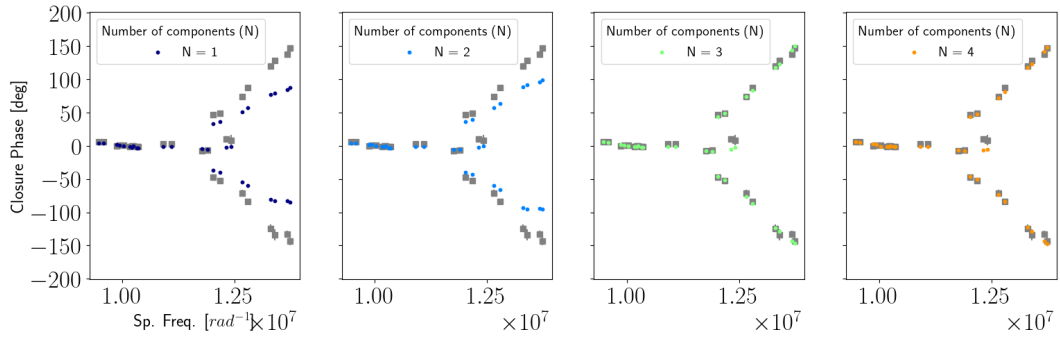


Figure 4.15: Representative example of CPs versus spatial frequencies of the data set that corresponds to the first CO band head at $2.2946 \mu m$ (gray squares). The colored dots show the CPs from the recovered images obtained with different numbers of principal components (see the labels on the plot).

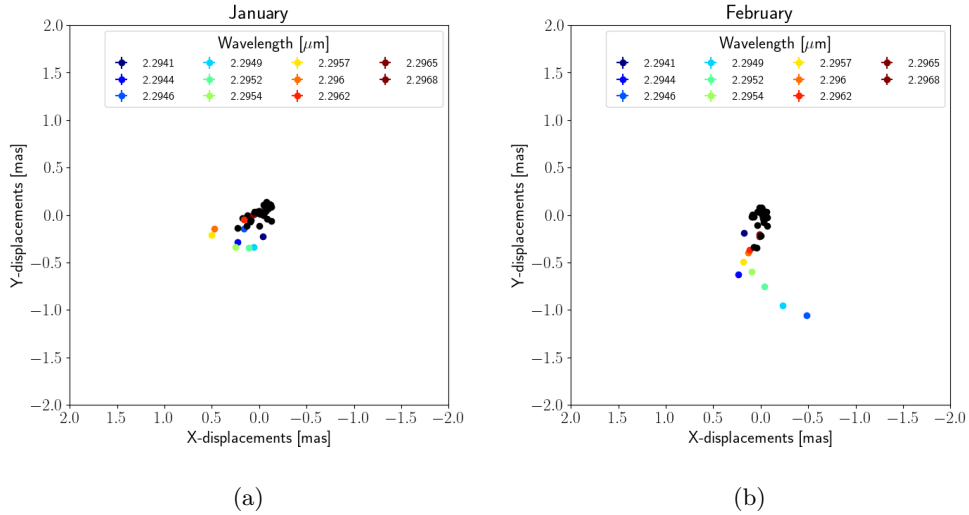


Figure 4.16: Two-dimensional photocenter offsets in mas. The black dots correspond to the photocenter position of the continuum emission and the labeled colored dots to the photo-centers of the CO band head. The error bars of the reported displacements are smaller than the used symbols.

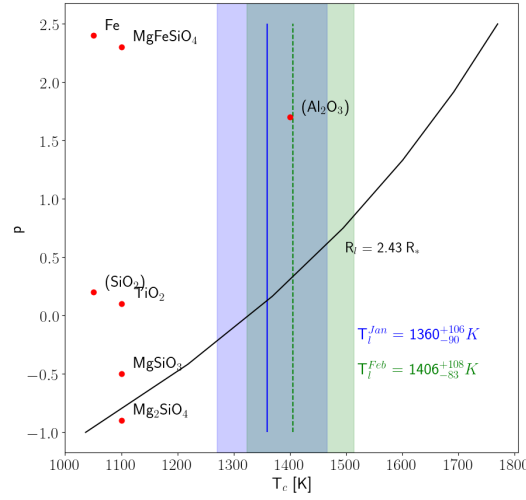


Figure 4.18: Curve of constant levitation radius ($R_l = 2.43 R_*$) represented with a solid-black line. The plot shows the condensation temperature, T_c , as a function of the dust absorption coefficient, p . The red circles indicate the positions of a variety of dust grains. The blue and green shaded regions correspond to the CO temperature ranges estimated from the single-layer model (see labels on the plot).

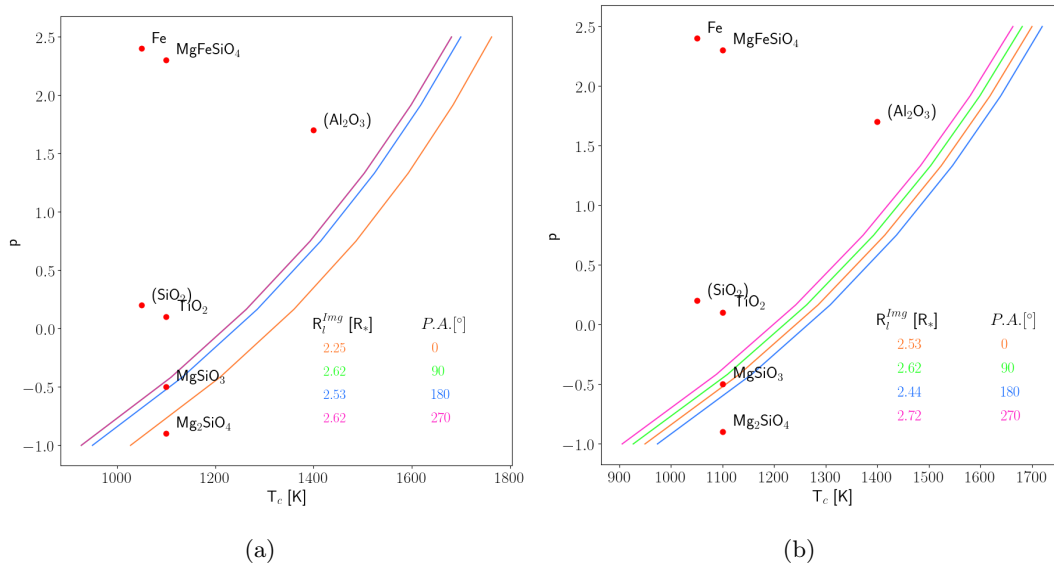


Figure 4.19: The panels are similar to Fig. 4.18 but they show the the median condensation radii obtained directly from the pure-line CO reconstructed images at different position angles (see labels on the panels) for a) the January and b) February epochs.

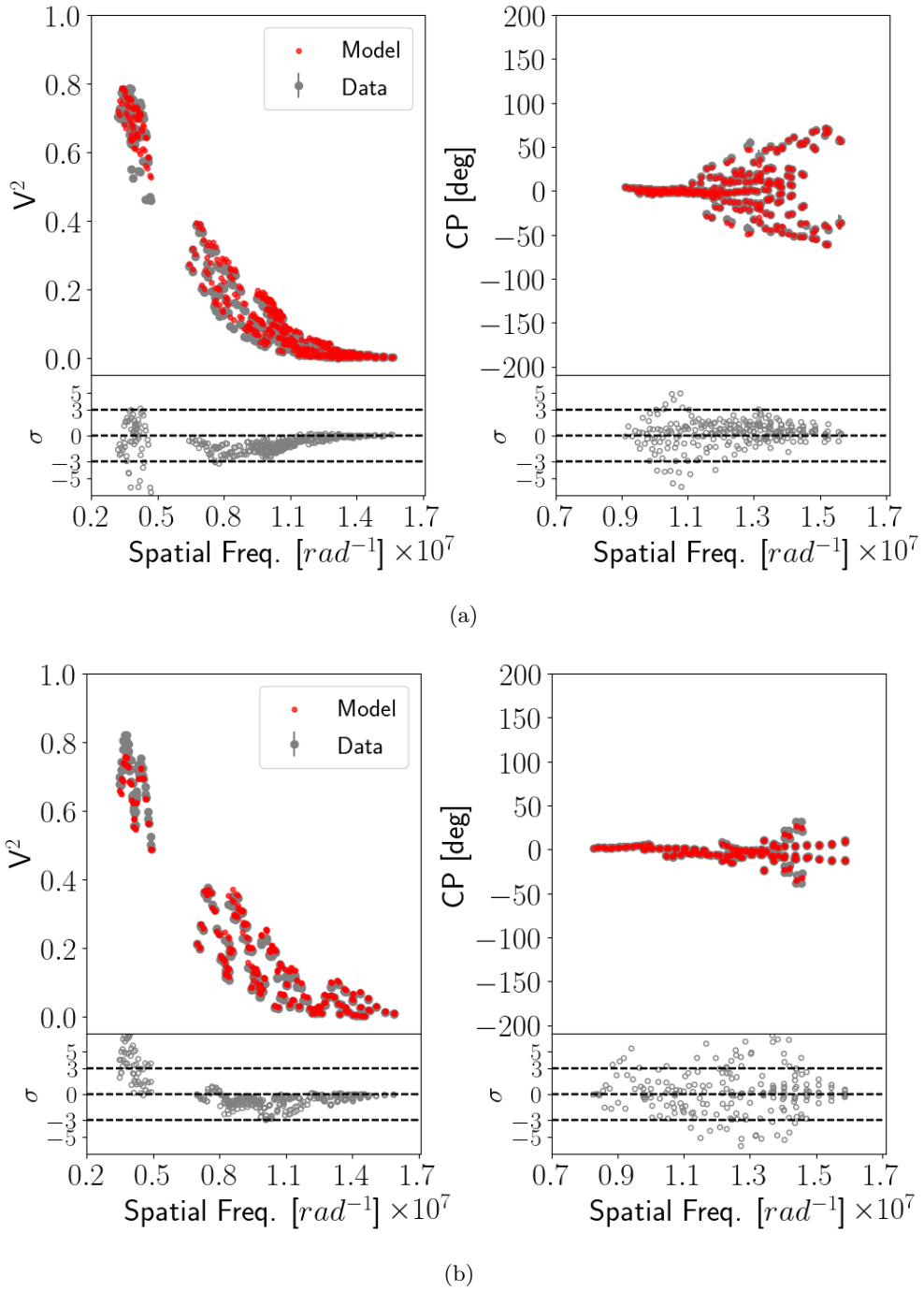
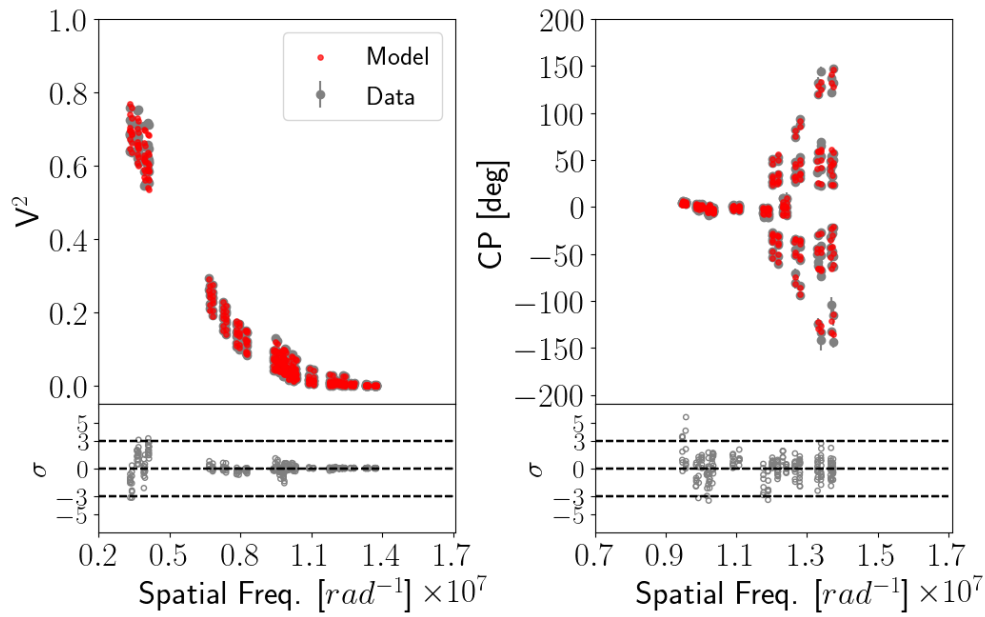
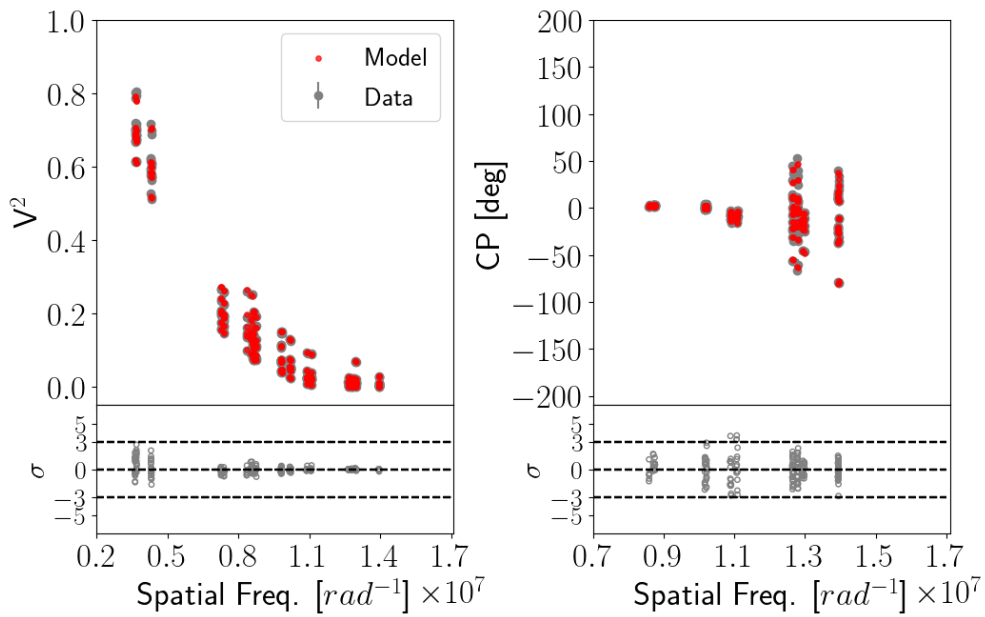


Figure 4.20: Fit to observed V^2 and CPs from the best reconstructed images across the pseudo-continuum for the (a) January and (b) February epochs. The red dots in the main panel correspond to the synthetic V^2 and CPs extracted from the raw reconstructed images. The data are shown with gray dots in the main panels. The lower panels show the residuals (in terms of the number of standard deviations) coming from the comparison between the data and the best-fit reconstructed images.

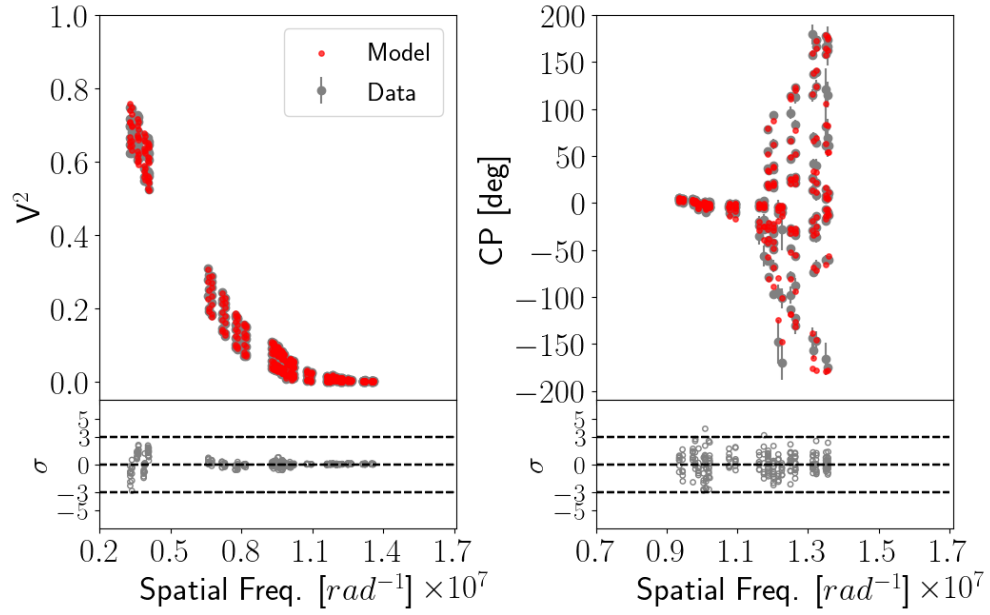


(a)

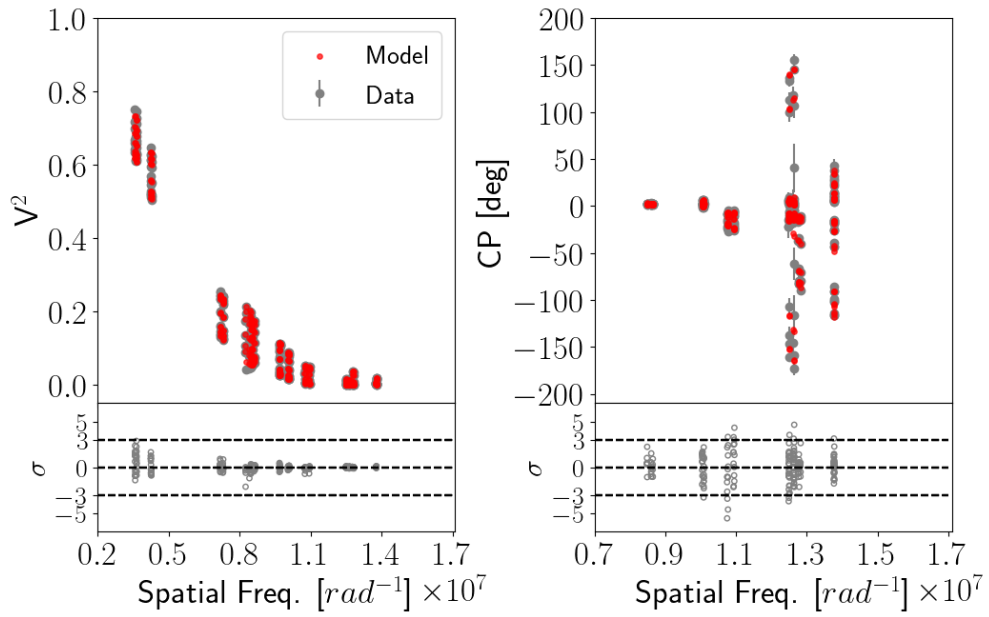


(b)

Figure 4.21: Fit to observed V^2 and CPs from the best reconstructed images across the first CO band head for the (a) January and (b) February epochs. The panels are as described in Figure 4.20.



(a)



(b)

Figure 4.22: Fit to observed V^2 and CPs from the best reconstructed images across the second CO band head for the (a) January and (b) February epochs. The panels are as described in Figure 4.20.

Conclusions and future work

Although there are lots of models to explain the mechanisms involved in the mass-loss processes during the AGB phase, the evidence to confront these models is still scarce. One of the main reasons for this, is the lack of high angular resolution observations in the regions where winds are formed ($1-3 R_*$). One way to solve the issue is through the analysis of high-angular resolution observations. In particular, AGB stars are bright in the NIR making them ideal candidates to be studied with IR interferometry. In this thesis, we employed interferometric observations to study the innermost parts of the M-type AGB star R Car. We are confident that the results presented across these pages will motivate novel periodic studies of other AGB stars with IR interferometry. The main results of this work can be summarized as follows.

- **The complex surface of R Car in the H -band.** Current models of convection in evolved stars, although very general, predict the emergence of structures of varying sizes on the star's surface. Such structures can change in position and size over intervals ranging from weeks to years. Furthermore, the relationship between these structures and the star's physical parameters can also be determined with models. However, can the models accurately capture the real physics happening in the stars? To answer this question, we have to confront those models with observations. As mentioned in Chapter 3, providing the necessary observations requires a window where dust is transparent and the ability to resolve the object's photosphere, something achieved in this work through interferometry in the H -band. The importance of this work relies in the fact that we were able not only to image the star's surface at two different pulsation phases but also to identify the surface

structures and their changes across the time, providing new observational tests on how convection could work in AGB stars. The main results are presented below.

- ◇ To derive the size of R Car’s stellar surface, we performed a parametric fitting to the V^2 at the two epochs of observation: 2014 and 2020 ($\phi = 0.78$ and 1.01 , respectively). This gave us an estimate of $\Theta_{\text{UD}}^{2014} = 10.23 \pm 0.05$ mas (1.86 ± 0.01 AU) for the 2014 epoch and $\Theta_{\text{UD}}^{2020} = 13.77 \pm 0.14$ mas (2.51 ± 0.23 AU) for the 2020 epoch. According to other studies, in H -band, the object is expected to be smaller around phase 0.8, and larger before the minimum of the pulsation phase. The diameters estimated by us agree with this trend.
- ◇ To characterize the asymmetric structure observed in the large CP variations, we reconstructed interferometric images. Those reconstructed images reveal the stellar surface and several bright spots lying above it. We measured the size of these patterns using a power spectrum analysis finding that the patterns change in size between the two pulsation phases. On average they are smaller when the star is smaller, and larger when the star is larger. Although this is an expected behavior, to our knowledge, this is the first time that it is shown for an M-type Mira star using images and with a quantitative analysis.
- ◇ To unveil the nature of these spots, we compared their measured size with three different extrapolations from stellar convection models. Those models establish convective cell sizes proportional to ~ 10 times the pressure scale height in the atmosphere of the target. Our findings suggest that the characteristic sizes of these spots are consistent with the predictions. With these results, we provide important evidence to the still scarce observational proofs of the role of convection in the evolution of AGBs.
- ◇ For a better characterization of the convective structures and their time evolution, future H -band interferometric images across the pulsation cycle of R Car are necessary. A proper comparison of those observations with state-of-the-art hydrodynamic and radiative transfer models will be mandatory.
- **The innermost gaseous layers in the K band.** Understanding the mechanisms leading to the mass loss in M-type AGB stars requires to know the types of dust that can form and survive near the star at temperatures around the condensation temperature limits (~ 900 - 1500 K). The reason is because the first interactions

that lead to the subsequent mass loss occur at distances around $1-3 R_*$, where the temperatures are of this order.

State-of-the-art wind models for AGB stars allow the exploration of dust particles with different compositions to understand how efficient they are as wind drivers through the scattering of the star's radiation. However, directly detecting the dust becomes a challenge since we require the angular resolution to observe the regions where all these interactions begin to occur, something that is not achievable with single-dish telescopes. The problem becomes more complicated since dust is mostly transparent in the near-infrared and, at mid-infrared wavelengths there is a considerable degradation of the resolution compared with shorter wavelengths.

One way to address this problem is by considering one of the most stable molecules against dissociation, which can form in the closer vicinity of the star: the CO. This molecule has the peculiarity that some of its (vibro-rotational) transitions, mainly those detected in the K band, form in regions where dust begins to condense. Therefore, by directly studying these regions through high-angular resolution techniques we can also provide indirect constraints on the types of dust proposed in the wind models. The importance of this second work is that we were able not only to image and to characterize the innermost CO layers at different pulsation phases but also to establish physical conditions of temperature and density that the dust candidates have to fulfill to be considered efficient wind-drivers. The main results of the work can be summarized as follows

- ◇ We obtained a first-order estimate of the size of the source by applying a geometrical model to the V^2 across the K -band for our two epochs, which are separated by ~ 30 days, corresponding to $\sim 10\%$ of the full pulsation period. From this analysis, we found that the size of the target changes with wavelength due to the presence of molecules like H_2O and CO at $\sim 2 \mu m$ and $\sim 2.29 - 2.33 \mu m$, respectively. The best estimate of the stellar disk diameter in the K band was derived at a wavelength of $\sim 2.23 \mu m$. Our parametric model allowed us to obtain a diameter of 16.67 ± 0.05 mas (3.03 AU) in January, 2018 and 14.84 ± 0.06 mas (2.70 AU) in February, 2018.
- ◇ We found prominent CO band heads in our GRAVITY spectra. These band heads also appear as drops in the V^2 data at the CO 2-0 ($\lambda_0 \sim 2.2946 \mu m$)

and CO 3-1 ($\lambda_0 \sim 2.3240 \mu\text{m}$) vibro-rotational transitions compared with the pseudo-continuum, which indicate that the CO line-emitting region is more extended. The innermost CO layers are important to trace the dust nucleation region since most of the C and O present in the atmosphere are concentrated in the stable bound of this molecule.

- ◇ We estimated the temperature, size, and optical thickness of these CO layers by employing a parametric single-layer model. With the optical thickness, we estimated also the column density at the minimum peak of the first CO band head. Our estimate of the column density goes in agreement with estimates reported for other AGB stars, and it is enough to allow the formation of dust grains. Although our results are consistent with other works, we can provide even better estimations with future higher angular resolution measurements in combination with more complex models of the CO layer/s.
- ◇ Using the temperature and size of the CO layer, we set constraints on the dust candidates that could coexist with the gas. We found that the composites Mg_2SiO_3 and MgSiO_4 can coexist at the same distances as the ones we obtained for the CO innermost layers ($\sim 2\text{-}2.4 R_*$). However, the condensation temperatures for these dust particles are lower than the temperatures obtained from the CO layer model. We propose that the temperature discrepancy is due to the nature of the single-layer model, which considers a homogeneous and symmetric distribution of the CO layer, giving average values for T_L , R_L , and τ_L . Our hypothesis is supported by the varying interferometric CPs and the posterior image reconstruction, which show that the CO distribution is neither homogeneous nor symmetric.
- ◇ To complement the information obtained from our symmetrical models, we reconstructed interferometric images. As expected from the variation of the CPs, we observed several asymmetries in the images across the spectral ranges and for both epochs of observation. To discard the presence of artifacts in our images, we employed bootstrap, PCA, and spectro-astrometric analyses. Our findings suggest the presence of a complex, perhaps clumpy distribution of the CO layer, which also changes within a period of 30 days or less.

5.1 Future work

Throughout this thesis, we studied the convective surface and the innermost gaseous layers of the AGB star R Car to provide observational evidence that helps us to understand how mass loss and convection occurs in these types of stars, two phenomena that are not fully understood. We also provided constraints on the types of dust that could coexist under physical conditions similar to the surrounding gas. However, due to its low optical thickness in the H and K bands, we were unable to detect direct signals from the sought dust particles. As can be seen in Figs. 5.1 and 5.2, the bands where the highest number of dust features are found are L (3.0-4.0 μm), M (4.0 - 5.0 μm), and N (8.0 - 13.0 μm).

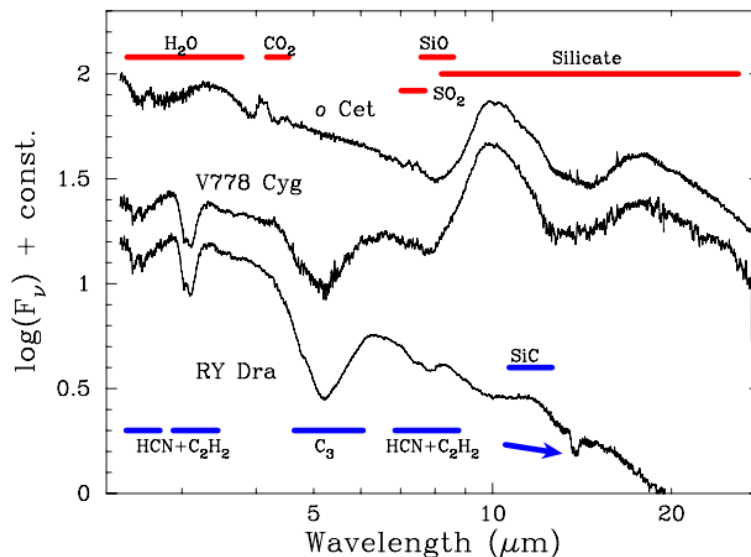


Figure 5.1: ISO-SWS spectra of the prototypical oxygen-rich AGB star Mira (o Ceti), a carbon-rich star (RY Dra) and a star with mixed chemistry (V778 Cyg): oxygen-rich dust but carbon-rich photosphere. The most prominent spectral features are indicated. Figure taken from Yamamura et al. (2000).

One way to study the dust responsible for these features is through the analysis of interferometric observations. As part of the binary AGB project, of which I am a member along with various colleagues from the interferometric community¹, we are

¹This work consists in the study of several M-, S- and C- type AGB stars with infrared interferometry

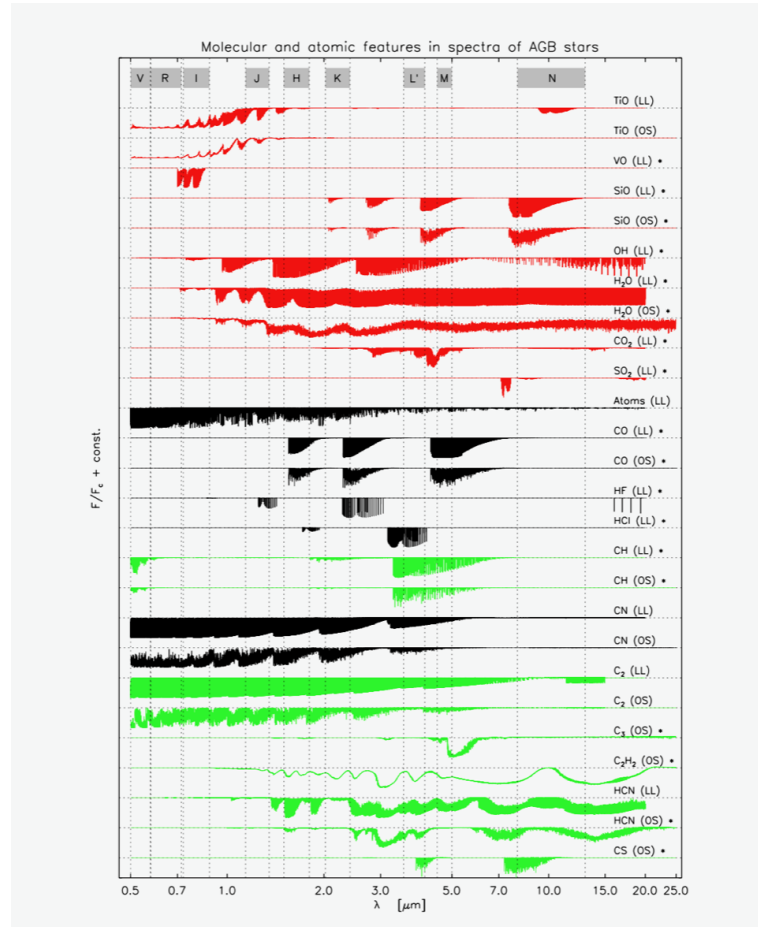


Figure 5.2: The typical spectrum of an AGB star in the infrared from 0.5 to 25 μm . The molecules contributing to the spectrum of an M-type AGB star are shown in red, and the molecules contributing to a C-type star are shown in green. The black spectra shows the molecular contributions to both type of stars. Image taken from [Paladini \(2011\)](#).

studying a sample of different AGB stars in the L , M , and N bands with infrared interferometry. Those observations were obtained with the MATISSE/VLTI instrument, using the small, medium, and large ATs configurations, resulting in angular resolutions of $\lambda/2B_{\text{max}} = 2.25$ mas and $\lambda/2B_{\text{max}} = 7.50$ mas for a baseline of 140 m and for wavelengths $\lambda = 3 \mu\text{m}$ and $\lambda = 10 \mu\text{m}$, respectively. In particular, I am analyzing R Car data. Although the analysis of these data is a work in progress, I can provide some

to unveil, for the first time, the asymmetric nature of the dust layers around them through image reconstruction and atmospheric modeling.

preliminary plots and describe the methodology applied.

- By applying a geometrical model to the V^2 data, we will estimate the size of the star across the L , M , and N bands, just as we did for the analyses in the H and K bands. This will provide us with an understanding of the extent of the different gas and dust layers surrounding the star.
- In Figs. 5.3 and 5.4 we present preliminary plots of the calibrated V^2 and CPs of R Car in the L and M bands. As we can see, the CPs vary widely between 0 - 180 degrees, indicating that the star is asymmetric in these bands. To depict the asymmetries, image reconstruction will be necessary. Given the high spectral resolution of our data, and the computational cost of the reconstruction algorithms, we will select different characteristic intervals such as 3.2 μm where the contribution of water is present, or between 4.5 - 5.0 μm where CO is present. Once we reduce, calibrate and filter our N band data, we will repeat this process to obtain images at this wavelength range.
- Just like with the GRAVITY instrument, MATISSE has the advantage of providing us with both, the interferometric observables and the spectrum of the star. By employing them, we can estimate the dust properties using complex radiative transfer models such as RADMC3D (Dullemond et al. 2012). A demonstration of the effectiveness of this methodology can be found in Cannon et al. (2023). Here is a brief description of the method that will be employed.
 - ◊ With the RADMC3D code, it is possible to obtain intensity maps from arbitrary 3D dust density distributions with different dust grain properties and stellar parameters. In contrast to the work of Cannon et al. (2023) where the authors could not perform image reconstruction of their target (α Ori), the geometrical distribution of the dust clumps will be given by our reconstructed images. By using those images as a starting point, we will only have to select the chemical composition, size, and distribution of the dust grains to run the models with these initial conditions.
 - ◊ Then, we can extract and compare the spectrum from the RADMC3D models with our data to test the consistency between both of them for different dust properties and distributions. By minimizing the differences between models

and data, we will be able to estimate the dust properties that best represent the spectra.

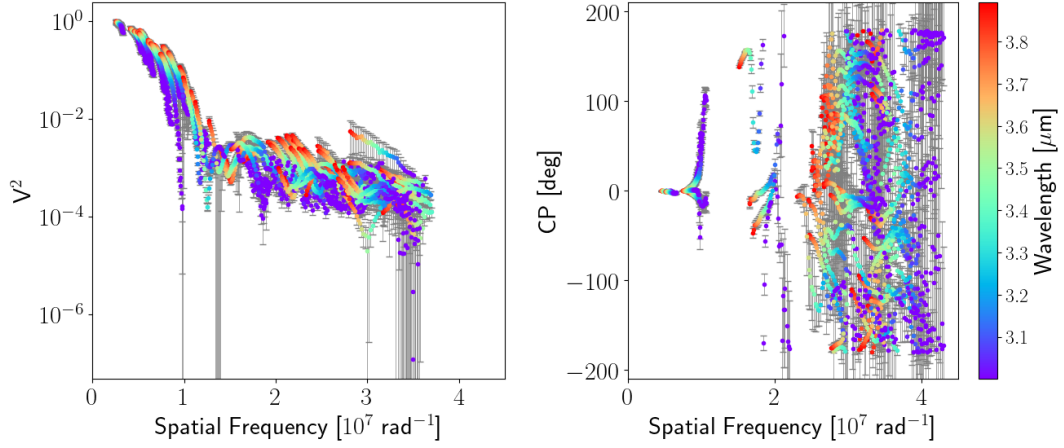


Figure 5.3: Calibrated V^2 and CPs of R Car in the L band ($3.0 - 4.0 \mu\text{m}$) as a function of the spatial frequency. We can see how the observables change depending of the wavelength probed. This means that different gaseous layers might have different sizes but also their distribution can be different. In other words, there is a chromatic behavior in the structure of the gaseous layers around R Car both in size and in the asymmetries traced.

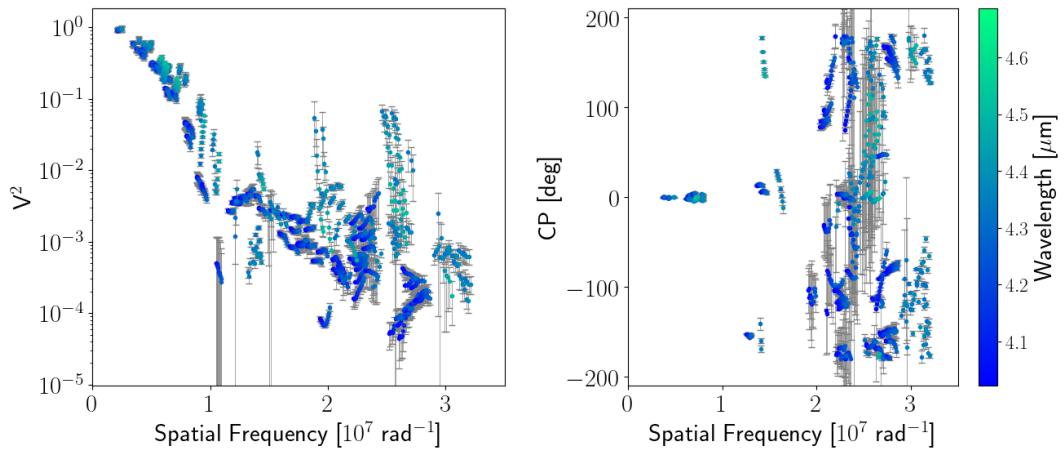


Figure 5.4: Calibrated V^2 and CPs of R Car in the M band ($4.1 - 4.7 \mu\text{m}$) as a function of the spatial frequency. We can see again the chromatic effects in the observables.

The analysis of these L , M , and N bands data will give us new observational evidence about the types of dust responsible for driving the winds in M-type AGB stars, their physical properties and their distribution around the star. Furthermore, image reconstruction of future interferometric observations at different epochs will allow us to monitor how this dusty circumstellar environment is changing, something that has not been done yet in the field with milliarcsecond resolution.

5.2 Prospects for the following decade: the ngVLA

The following decade will be crucial for our understanding of the complex phenomena occurring at the innermost parts of AGB stars. Once the next-generation Very Large Array (ngVLA) is finished, it will enable the imaging of astronomical sources with an unprecedented detail by providing improvements in sensitivity and angular resolution compared with current radio interferometers operating in the 1.2 -116 GHz range.

In the field of stellar physics, with the Karl G. Jansky Very Large Array (VLA) and ALMA it is possible to marginally resolve some of the closest ($d \lesssim 150$ pc) AGBs and RSGs whose enormous radio photospheres can span several AU and subtend up to a few tens of mas (see e.g., [Asaki et al. 2023](#)). However, with the ngVLA, we will be able to measure detailed properties of radio photospheres (e.g., the presence of atmospheric temperature gradients, spots, and surface features, as well as temporal changes). With those studies, it will be possible to complement what we know about the atmospheric physics, including the temperature structure of the atmosphere, and to set constraints on the mechanisms (e.g., shocks, pulsation, convection) that help to drive the observed mass-loss rates from these stars. Together with the interferometric observations in the infrared, it will be possible to perform more detailed comparisons with predictions of state-of-the-art 3D dynamic atmospheric models of AGB and RSG stars. Empirically testing the emerging new 3D models that include the effects of pulsation, convection, shocks and dust condensation, will demand new ultra high-resolution measurements of diverse samples of stars using instruments like the ngVLA ([Akiyama & Matthews 2019](#)).

To illustrate the capabilities of the future ngVLA, in [Fig. 5.5](#) we present an example of an image reconstruction of four simulated images with different characteristics. The interferometric observables were extracted by taking into account the $u - v$ coverage of the ngVLA Main Array (214 18m antennas, baseline from tens of meters to ~ 1000 km, see [Fig. 5.6](#)). As we can see, the reconstructed images recover the features in the

simulated images with a very-high detail. The interested reader can consult [Akiyama & Matthews \(2019\)](#) for more details of the reconstruction algorithms employed.

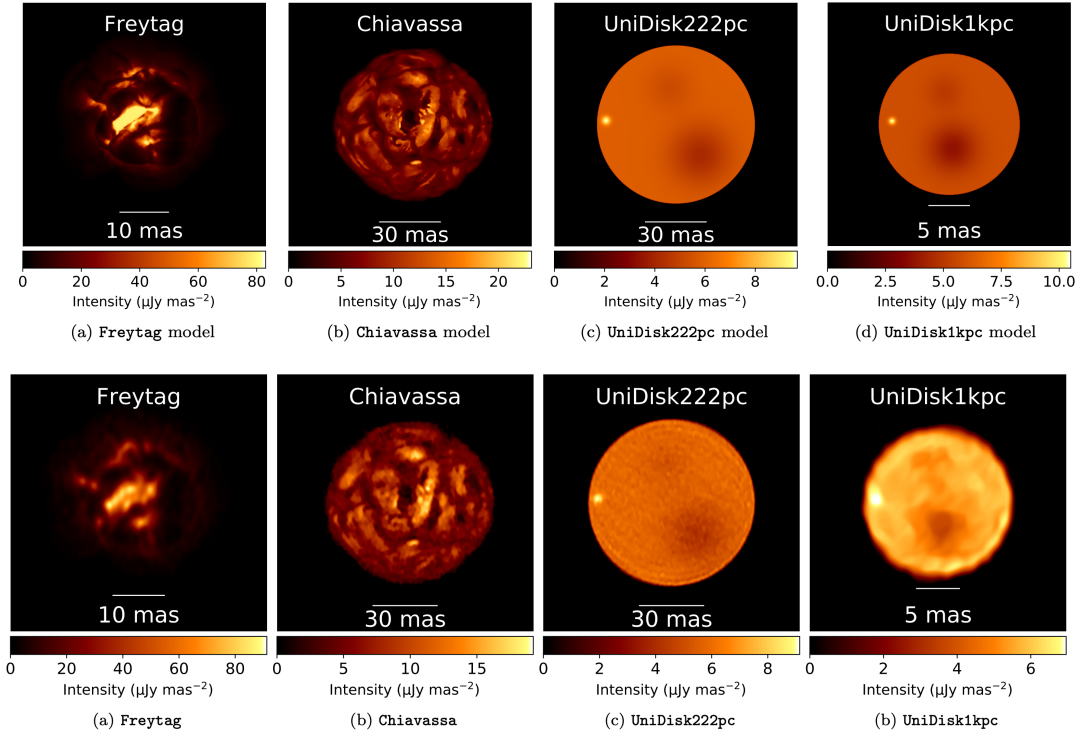


Figure 5.5: Upper row: simulated stellar models used to test the capabilities of the ngVLA. Once the observables were simulated, an image reconstruction was performed and the results can be seen in the lower row. The first two panels on the left were obtained from simulations based on dynamic 3D atmospheric models and correspond to a $1 M_{\odot}$ AGB (panel a) and a $12 M_{\odot}$ RSG (panel b). Those images were extracted from [Freytag et al. \(2017\)](#) and [Chiavassa et al. \(2009\)](#), respectively. Panels (c) and (d) correspond to toy models comprising a uniform circular disk with three 'spots' of different sizes superposed (one brighter than the underlying photosphere and two that are cooler). These models are then located at different distances : 222 pc and 1 kpc, respectively. Figure taken from [Akiyama & Matthews \(2019\)](#).

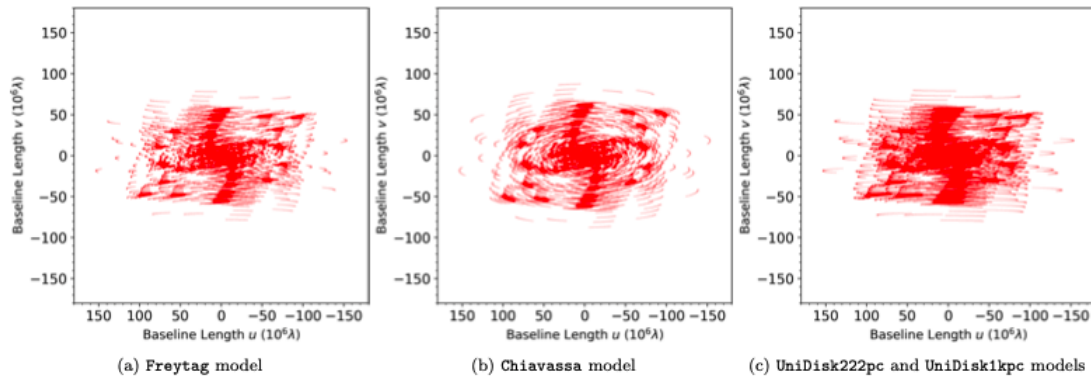


Figure 5.6: uv-coverage of the simulated ngVLA observations. The simulated ngVLA observations of each model in the upper panel of Fig. 5.5 were obtained using the `simobserve` task in `CASA`. In all cases the array configuration was taken to be the ngVLA Main Array. Figure taken from [Akiyama & Matthews \(2019\)](#).

5.3 Closing remarks

In this thesis, we have showed that the structures on the surface and the innermost layers of gas/dust in AGB stars can be highly asymmetric at different spatial and temporal scales. To characterize these changes both spatially and temporally, new interferometric observations with baselines that allow us to map different angular scales are necessary, and this has to be done over one or several pulsation cycles of the star.

We also showed that such detailed studies are scarce and require observations with the highest possible quality. However, we demonstrated that they are not impossible to achieve and that provide valuable results. Therefore, it will be worthwhile to extend these studies to a significant sample of AGB stars in different environments. As we can see, there are lots of new things to discover in the near future, and instruments like the ngVLA or the VLTI and their improvements will be an essential part of these discoveries. Eventually, we expect to build a sufficiently large sample of high-resolution observational evidence to fine-tune the theoretical models, in order to increase their predictive power.

Python codes

Here, I show examples of the codes used to obtain the results presented in Chapter 4. This notebook can also be found in [this](#) Github repository. The repository contains a Jupyter notebook which is included here in a pdf format.

R Car GRAVITY analysis

Abel Rosales-Guzmán

September 18, 2023

1 R Car analysis tools

1.0.1 This is a Python-Jupyter notebook which contains some examples of the usage of the different algorithms used to analyze GRAVITY-VLTI data of the Mira star R Car.

2 Contents

Example of the MCMC model fitted to the GRAVITY-VLTI R Car V2

Example of the Molsphere model fitted to the GRAVITY-VLTI R Car V2

Example of the Bootstrapping algorithm applied to the interferometric observables of R Car

Example of the Principal Component Analysis applied to our reconstructed images of R Car

2.0.1 The following are required Python (version > 3.0) packages which need to be installed before the execution of the current Jupyter Notebook:

Astropy

corner

emcee

lmfit

matplotlib

numpy

scipy

sklearn

oitools.py (provided in the current project/directory)

```
[90]: ### Author: Abel Rosales-Guzman  
###The following lines load the required Python modules:  
from astropy.modeling import models  
import astropy.io.fits as pyfits  
from astropy import constants as const  
from astropy import units as u  
from copy import copy
```

```

import corner
import cv2
import datetime
import emcee
from lmfit import Model, Parameters, minimize
import matplotlib.pyplot as plt
from matplotlib.ticker import FormatStrFormatter
from multiprocessing import Pool
import numpy as np
import oitools
import os
import scipy.special as sp
from sklearn.decomposition import PCA
from sklearn.utils import resample
#####

```

2.0.2 The following script (In 2 and 4) provides an example of the Uniform Disk model fitted to the GRAVITY-VLTI R Car V². The code uses a Markov-Chain Monte-Carlo (MCMC) method implemented through the Python emcee package. The model uses the parametric expression of a Uniform Disk in Fourier space. This model only contains two parameters, the diameter of the disk, and a coefficient to account for the over-resolved flux/component (Fr) plausible present in the data. While the model only has two parameters, we used the MCMC approach to better estimate the statistical errors of the best-fit model. The following lines run the Uniform Disk model for one spectral channel (2.228 μm) of R Car's pseudo-continuum. The same setup could be used to replicate the best-fit models for other spectral channels in the pseudo-continuum or across the CO bandheads.

```

[2]: ### MCMC auxiliary functions:
def mas2rad(x_mas):
    x_rad = 4.847309743e-9 * x_mas
    return x_rad

def rad2mas(x_rad):
    x_mas = x_rad/4.847309743e-9
    return x_mas

## The following function describes a fully illuminated uniform disk in the
↪Fourier space:
def disk(u, v, diam, Fr):
    """
    diam = angular diameter in mas
    Fr = Scaling factor that accounts for the over-resolved flux
    """
    diam = mas2rad(diam)
    r = np.sqrt(u**2 + v**2)

```

```

v_disk = 2 * (sp.j1(np.pi * diam * r) / (np.pi * diam * r))

return Fr*(v_disk)**2

## The following function describes the log-prior probability:
def lnprior(theta):
    # probability is uniform inside a given range, and zero outside
    if (1. < theta[0] < 30.) and (0. < theta[1] < 2.): #and (0. < theta[2] < 3.
        ↪) :
        return 0.0
    return -np.inf

## The following function describes the log-likelihood (i.e, the Chi2) ↪
↪probability:
def lnlike(theta, u, v, vis2, vis2err):
    diam = theta[0]
    Fr = theta[1]
    vis2model = disk(u, v, diam, Fr)
    chi2 = -0.5*np.sum((vis2-vis2model)**2/(vis2err)**2)
    return chi2

## The following function describes the posterior probability:
def lnprob(theta, u, v, vis2, vis2err):
    lp = lnprior(theta)
    if lp == -np.inf:
        return lp
    return lp + lnlike(theta, u, v, vis2, vis2err)

```

```

[4]: ## The following line passes to a variable the name of the OIFITS file with the ↪
        ↪data:
fits_f='phasediff_18_January_a200_COMB_RCar_cont_2.228m.fits'

#####Automatic from here#####
## The data are read from the OIFITS file ####
oidata = pyfits.open(fits_f)
oi_wave = oidata['OI_WAVELENGTH'].data
oi_vis2 = oidata['OI_VIS2'].data

waves = oi_wave['EFF_WAVE']
vis2 = oi_vis2['VIS2DATA']
vis2_err = oi_vis2['VIS2ERR']

vis2_err2 = np.full(vis2.shape, 0.01)
u = oi_vis2['UCOORD']
v = oi_vis2['VCOORD']

nvis = vis2.shape[0]

```

```

ndim = 2
nwalkers = 250
pos1 = np.random.uniform(1., 30., size=nwalkers)
pos2 = np.random.uniform(0., 2., size=nwalkers)

fig2, ax2 = plt.subplots(ncols=1,nrows=1, figsize=(7,7))

spf_u = u/waves[0]
spf_v = v/waves[0]
bssl = np.sqrt(spf_u**2+spf_v**2)

#### The following lines run the Markov chains:
sampler = emcee.EnsembleSampler(nwalkers, ndim, lnprob, args=(spf_u, spf_v,
↳vis2, vis2_err2))
steps = 150
pos = np.array([pos1, pos2]).T

sampler.run_mcmc(pos,steps, progress = True)
samples = sampler.get_chain()
flat_samples = sampler.get_chain(discard=70, flat=True)
fig1, _axs1 = plt.subplots(nrows=2, ncols=1, figsize=(12,7), sharex=True)
axs1 = _axs1.flatten()
axs1[1].set_xlabel('Step number')
axs1[0].set_ylabel('Diameter')
axs1[1].set_ylabel('Fr')

inds = np.random.randint(len(flat_samples), size=50)
for i in range(ndim):
    axs1[i].plot(samples[:, :, i], "k", alpha=0.3)

##### Plots #####
diam_mcmc, Fr_mcmc = map(lambda v: (v[1], v[2] - v[1], v[1] - v[0]), zip(*np.
↳percentile(flat_samples, [16, 50, 84], axis=0)))

fig3 = corner.corner(flat_samples, labels=['D', 'Fr'], show_titles=True,
↳title_fmt='0.2f',
    levels=(1 - np.exp(-0.5), 1 - np.exp(-2.0)),
    truths=[diam_mcmc[0], Fr_mcmc[0]], quantiles=[0.16, 0.5, 0.84],
    title_kwargs={'fontsize': 12})
print('Best Values')
print('Theta_UD = {:.2f} +- {:.2f} {:.2f} mas'.format(diam_mcmc[0],
↳diam_mcmc[1], diam_mcmc[2]))
print('F_r = {:.3f} +- {:.3f} {:.3f}'.format(Fr_mcmc[0], Fr_mcmc[1],
↳Fr_mcmc[2]))

iind1 = np.argsort(bssl)

```



```

ax2.errorbar(bssl, vis2, yerr=vis2_err2, fmt='o', ms=5, label='Data', c='red')
#####
ax2.plot(bssl[iind1], disk(sp_f_u, sp_f_v, diam_mcmc[0], Fr_mcmc[0])[iind1],
        ↪label='Model', c='blue', zorder=500)
ax2.text(1.0e7, 0.8, r'\Theta_{UD}={:.2f}_{-{: .2f}}^{+{: .2f}}$ mas'.
        ↪format(diam_mcmc[0], diam_mcmc[1], diam_mcmc[2]), fontsize=17)
ax2.text(1.0e7, 0.65, r'$F_r={:.3f}_{-{: .3f}}^{+{: .3f}}$'.
        ↪format(Fr_mcmc[0], Fr_mcmc[1], Fr_mcmc[2]), fontsize=17)

ax2.set_ylim(-0.05, 1.0)
ax2.set_xlim(0.1e7, 1.71e7)
ax2.set_xticks(np.arange(0.1e7, 1.71e7, step=0.3e7))
ax2.set_title(r'{:.3f} $\mu$ m$'.format(waves[0]/1.e-6))
ax2.set_xlabel(r'Spatial Frequency [$rad^{-1}$]', fontsize=18)
ax2.set_ylabel('V$^2$', fontsize=18)

plt.show()

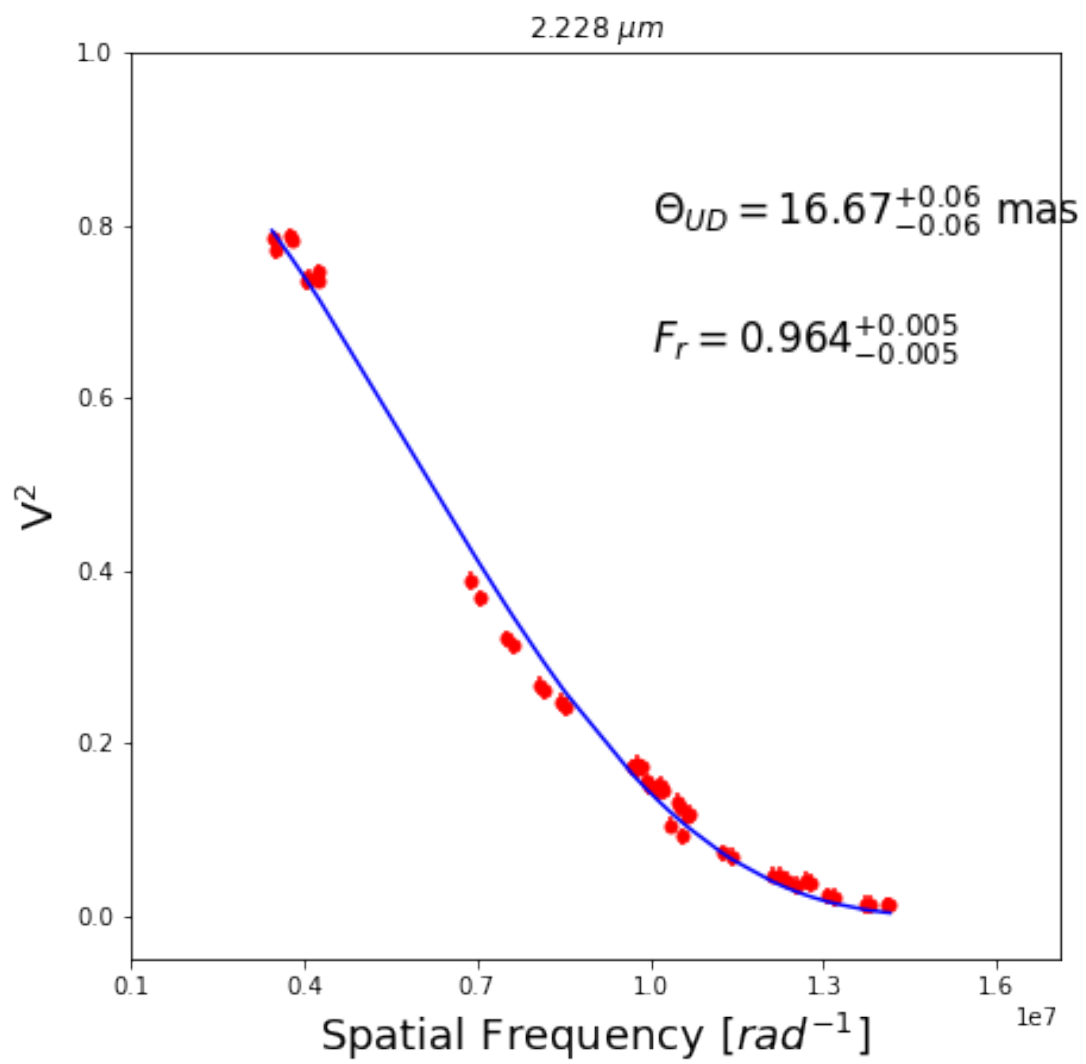
```

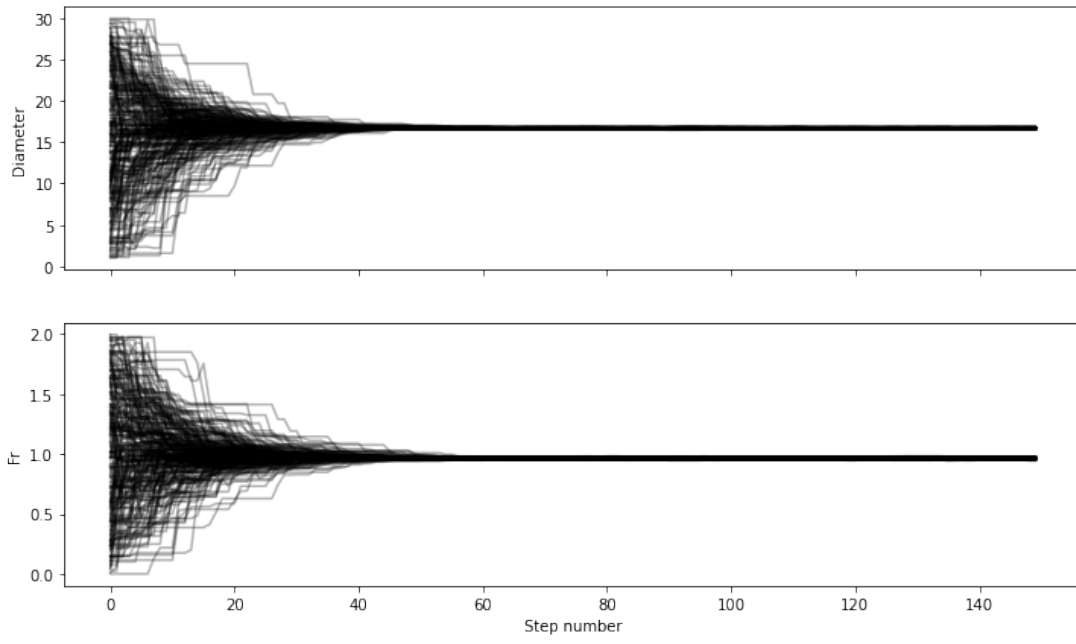
100% | 150/150 [00:01<00:00, 143.10it/s]

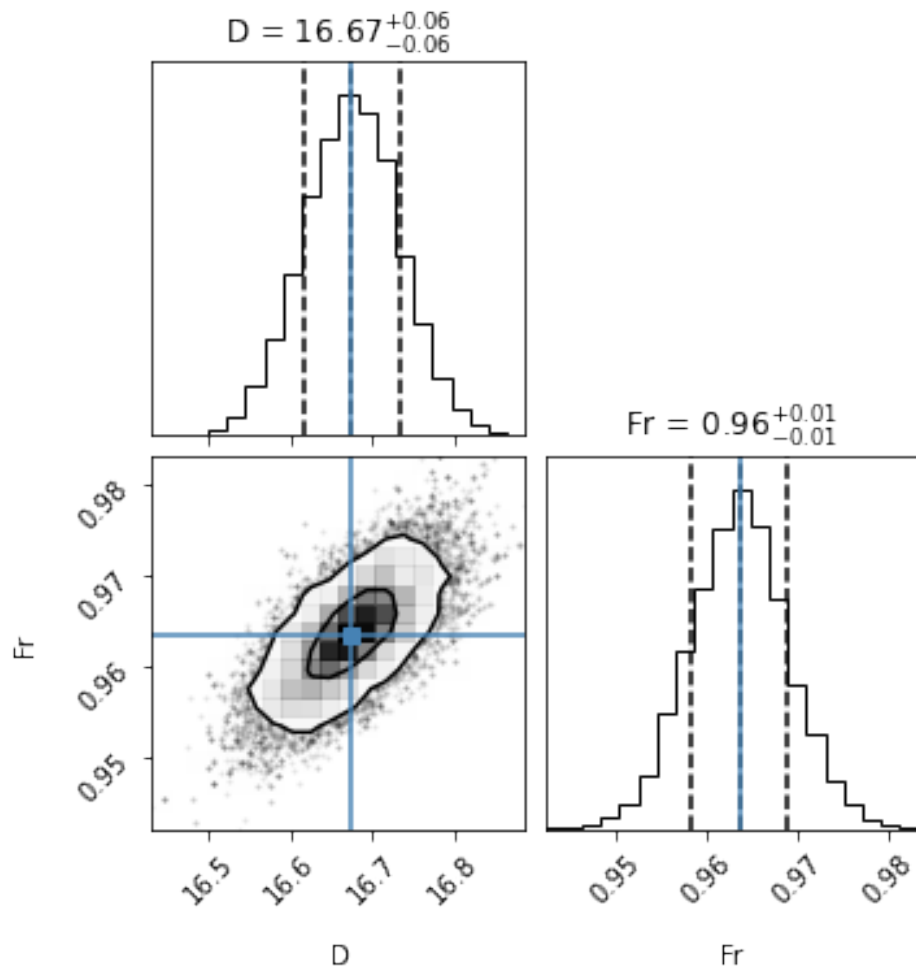
Best Values

Theta_UD = 16.67 +- 0.06 0.06 mas

F_r = 0.964 +- 0.005 0.005







[Go back to top](#)

2.0.3 The following part of the notebook script (ln 5, 8 and 30) provides an example of the single layer model (the so-called MOLsphere) fitted to the GRAVITY-VLTI R Car V² and spectra. The code also uses a Markov-Chain Monte-Carlo method implemented through the Python emcee package. The model uses the parametric set of expressions (see e.g., Rodriguez-Coira et al., 2021 and/or the main text of our manuscript) which describe a star that irradiates as a Black-Body surrounded by an infinitesimal layer of gas, which also irradiates as Black-Body modified by a given optical depth. The model fits simultaneously the spectrum of the source (particularly the region of the CO bandhead in the K-band GRAVITY data) and the squared visibilities. The best-fit model provides an estimate of the temperature, optical depth and the size of the layer, in combination with the size of the central star. The following lines run the MOLsphere model for one spectral channel (2.2946 μ m). However, the same setup could be used to replicate the best-fit models for other spectral channels across the CO bandheads

```
[5]: ##### Visibility and Intensity Functions #####

#The following function creates a pixel grid for the MOLsphere model:
def img_grid(npixels, pixelscale):
    size = npixels*pixelscale
    x = np.linspace(-0.5*size, 0.5*size, npixels)
    y = np.linspace(-0.5*size, 0.5*size, npixels)
    return x, y

# This is the function that defines the MOLsphere model:
def SLModel(Tl, Rl, tau, Fr):
    """
    This function calculates the V2 corresponding to the MOLsphere
    Tl, Rl = Temperature and radius of the layer
    Ts, Rs = Temperature and radius of the star
    tau = optical dept of the molecular layer at a wavelength lamdba
    r = radius to evaluate the model
    Fr = Scaling factor to account for the over resolved component
    Wavelength is given in microns
    """
    npixels = 128 #px
    pixelscale = 0.46875 #[mas/px]
    x, y = img_grid(npixels, pixelscale)
    r=np.zeros([x.shape[0], y.shape[0]])
    for j in range(128):
        for k in range(128):
            r[j,k]=np.sqrt(x[j]**2+y[k]**2)

    I2 = np.zeros([128,128])
    Rs = 5. # diameter of R Car = 10 mas, thus R = 5mas
    Ts = 2800. # Kelvin, effective temperture of R Car
    wavelength = slm_wave
```

```

bb_s = models.BlackBody(temperature=Ts*u.K)
bb_L = models.BlackBody(temperature=Tl*u.K)

B_s = bb_s(wavelength*u.micron)
B_l = bb_L(wavelength*u.micron)
# I = []
for i in range(r.shape[0]):
    for j in range(r.shape[1]):
        if r[i,j] <= Rs:
            cos_beta1 = (1./Rl)*np.sqrt(Rl**2-r[i,j]**2)
            I2[i,j] = B_s.value*np.exp(-tau/cos_beta1) +
↳B_l.value*(1-np.exp(-tau/cos_beta1))
        elif (r[i,j] > Rs) and (r[i,j] < Rl):
            cos_beta = np.sqrt(1-(r[i,j]/Rl)**2)
            I2[i,j] = B_l.value*(1-np.exp(-2*tau/cos_beta))
        else:
            I2[i,j] = 0.000
    ##Adding the Over resolved component
    I3 = I2/np.sum(I2)
    I3 = Fr*I3
    Fr_comp = 1.-Fr
    [iind0, iind1] = np.where(I3 == 0)
    px_zero = iind0.shape[0]
    temp = Fr_comp/px_zero
    I3[iind0, iind1] = temp
    ###Computing the V2
    vis_synth, phi_synth, t3phi_synth = oitools.compute_obs(oi_data, I3,
↳pixelscale, 6, 4)
    return (np.squeeze(vis_synth))**2

def I_SLModel(Tl, Rl, tau):
    """
    This function calculates the intensity (I) of the MOLsphere
    Tl, Rl = Temperature and radius of the layer
    Ts, Rs = Temperature and radius of the star
    tau = optical dept of the molecular layer at a wavelength lamdba
    r = radius to evaluate the model
    wavelength is given in microns
    """
    npixels = 128 #px
    pixelscale = 0.46875 #[mas/px]
    x, y = img_grid(npixels, pixelscale)
    r=np.zeros([x.shape[0], y.shape[0]])
    for j in range(128):
        for k in range(128):
            r[j,k]=np.sqrt(x[j]**2+y[k]**2)
    I2 = np.zeros([128,128])

```

```

Rs = 5. # diameter of R Car = 10 mas, thus R = 5mas
Ts = 2800. # Kelvin, effective temperature of R Car
wavelength = slm_wave
bb_s = models.BlackBody(temperature=Ts*u.K)
bb_L = models.BlackBody(temperature=Tl*u.K)

B_s = bb_s(wavelength*u.micron)
B_l = bb_L(wavelength*u.micron)
# I = []
for i in range(r.shape[0]):
    for j in range(r.shape[1]):
        if r[i,j] <= Rs:
            cos_beta1 = (1./Rl)*np.sqrt(Rl**2-r[i,j]**2)
            # print(cos_beta)
            I2[i,j] = B_s.value*np.exp(-tau/cos_beta1) +
↳B_l.value*(1-np.exp(-tau/cos_beta1))
            # I2[i,j]=I
        elif (r[i,j] > Rs) and (r[i,j] <= Rl):
            cos_beta = np.sqrt(1-(r[i,j]/Rl)**2)
            # print(r[i,j], cos_beta, Rl2)
            I2[i,j] = B_l.value*(1-np.exp(-2*tau/cos_beta))
            # I2[i,j]=I
        else:
            I2[i,j] = 0.000

return I2

```

[8]: *###Similar to the first example in this notebook, the following functions*
↳*define the probabilities for the MCMC engine:*

```

def resid_flux(params, Flux, fluxerr):
    """
    Function used to fit the tau given Tl and Rl
    """
    pars = params.valuesdict()
    Tl = pars['Tl']
    Rl = pars['Rl']
    tau = pars['tau']
    temp_I = I_SLModel(Tl, Rl, tau)
    F_tau0 = flux_tau0_1[0] # Flux at zero optical depth (see Rodríguez-Coira,
↳et al., 2021)
    F_layer = np.sum(temp_I) # Flux of the layer
    F_teor = F_layer/F_tau0
    return (Flux-F_teor)/fluxerr

def lnprior(theta):
    #flat prior, probability is uniform inside a given range, and zero outside

```

```

    if (1000. < theta[0] < 2800.) and (5.1 < theta[1] < 20.) and (0.01 <
↳theta[2] < 2.):
        # print(theta)
        return 0.0
    return -np.inf

def lnlike(theta, vis2, vis2err):
    Tl = theta[0]
    Rl =theta[1]
    Fr = theta[2]
    # ndof = vis2.shape[0]
    # dim = len(theta)
    factor = 39. #ndof
    #####fitting the tau#####
    params = Parameters()
    params.add('tau', value=0.5, min=1.e-6, max=5.)
    params.add('Tl', value=Tl, vary=False)
    params.add('Rl', value=Rl, vary=False)
    result = minimize(resid_flux, params, args=(norm_spec[:,1][ind2], (np.
↳array([0.05]))**2))
    taul = result.params['tau'].value
    Taus_err = result.params['tau'].stderr
    TChi2 = result.redchi
    if TChi2 < 3: ##keeping only the smallest Chi^2
        Tauss_chi2.append(TChi2)
        Tauss.append(taul)
        TRl.append(result.params['Rl'].value)
        TTl.append(result.params['Tl'].value)
        vis_synth2 = SLModel(Tl, Rl, taul, Fr)
    else:
        Tauss_chi2.append(TChi2)
        Tauss.append(0.)
        TRl.append(result.params['Rl'].value)
        TTl.append(result.params['Tl'].value)
        tau_no=0.
        vis_synth2 = SLModel(Tl, Rl, tau_no, Fr)
    return ((-0.5*np.sum((vis2 - vis_synth2)**2/vis2err**2)/(factor)))

def lnprob(theta, vis2, vis2err):
    lp = lnprior(theta)
    if not np.isfinite(lp):
        return -np.inf
    else:
        return lp + lnlike(theta, vis2, vis2err)

```



```

[30]: ## The MCMC main routine. Notice that it has to go inside the "if" command to
↳run in parallel with the Pool() module

if __name__=="__main__":
    #Estimated time for the execution of this cell using 1000 iterations: 4Hrs
↳40min
    norm_spec = np.genfromtxt('RCar_normspec_final_Jan.txt') #January
↳#norm_spec[:,0]-> wavelength, norm_spec[:,1]- > Flux
    oi_data = 'phasediff_18_January_COMB_RCar_CO_2.2946m.fits' #filename of the
↳OIFITS data file

    specr_min = [2.2945e-6] #Spectral range defined in meters
    specr_max = [2.2947e-6]
    #####
    wave_range = [2.2945e-6, 2.2947e-6] #### Wavelength range that wants to be
↳fitted
    flux_tau0_1 = [0.0013643644802048] # Calculated flux if tau = 0 (See Eq. 7
↳from Rodriguez-Coira et al., 2021)
    lambda_co=[2.2946] #center of the band head defined in microns

    #####Automatic from here#####
    oidata = pyfits.open(oi_data)
    oi_wave = oidata['OI_WAVELENGTH'].data
    oi_vis2 = oidata['OI_VIS2'].data
    oi_t3 = oidata['OI_T3'].data
    waves = oi_wave['EFF_WAVE']
    vis2 = oi_vis2['VIS2DATA']
    vis2_err = oi_vis2['VIS2ERR']
    t3 = oi_t3['T3PHI']
    t3_err = oi_t3['T3PHIERR']

    u_coord = oi_vis2['UCOORD']
    v_coord = oi_vis2['VCOORD']
    u1 = oi_t3['U1COORD']
    u2 = oi_t3['U2COORD']
    v1 = oi_t3['V1COORD']
    v2 = oi_t3['V2COORD']

    nvis = vis2.shape[0]
    nt3phi = t3.shape[0]
    vis2_err2 = np.full(vis2.shape[0], 0.01)

    #####
    # To compute the UV coordinates of the closure phases:
    uv_cp = np.zeros([u1.shape[0]])
    u_cp = np.zeros([u1.shape[0]])
    v_cp = np.zeros([u1.shape[0]])

```

```

u3 = -1.0 * (u1 + u2)
v3 = -1.0 * (v1 + v2)

for j in range(u1.shape[0]):
    uv1 = np.sqrt((u1[j])**2 + (v1[j])**2)
    uv2 = np.sqrt((u2[j])**2 + (v2[j])**2)
    uv3 = np.sqrt((u3[j])**2 + (v3[j])**2)
    if uv1 >= uv2 and uv1 >= uv3:
        uv_cp[j] = uv1
        u_cp[j] = u1[j]
        v_cp[j] = v1[j]
    elif uv2 >= uv1 and uv2 >= uv3:
        uv_cp[j] = uv2
        u_cp[j] = u2[j]
        v_cp[j] = v2[j]
    elif uv3 >= uv1 and uv3 >= uv2:
        uv_cp[j] = uv3
        u_cp[j] = u3[j]
        v_cp[j] = v3[j]

[ind] = np.where((waves >= wave_range[0]) & (waves <= wave_range[1]))
slm_wave = waves[ind[0]]/1.e-6
print(slm_wave)
[ind2] = np.where((norm_spec[:,0] >= wave_range[0]/1.e-6) & (norm_spec[:,0]
↪ <= wave_range[1]/1.e-6)) ##index of the spectrum
spf_u = u_coord/waves[0]
spf_v = v_coord/waves[0]
bsl = np.sqrt(spf_u**2 + spf_v**2)
print(norm_spec[:,0][ind2][0])
Tauss = []
Tauss_chi2=[]
TR1=[]
TT1=[]
np.seterr(all='ignore')
ndim = 3
nwalkers = 20 #must be even
steps = 1000 #1000

with Pool() as pool:
    sampler = emcee.EnsembleSampler(nwalkers, ndim, lnprob, args=(vis2,
↪ vis2_err2), threads=pool)

    pos0 = np.random.uniform(1000, 2800, size=nwalkers)
    pos1 = np.random.uniform(5.1, 20, size = nwalkers)
    pos2 = np.random.uniform(0.1, 2., size = nwalkers)
    pos = np.array([pos0, pos1, pos2]).T
    sampler.run_mcmc(pos, steps, progress=True)

```

```

samples = sampler.get_chain()

fig, axes = plt.subplots(3, figsize=(10,7), sharex = True)
fig.patch.set_facecolor('white')
labels = ['Tl', 'Rl', 'Fr']
for i in range(ndim):
    ax = axes[i]
    ax.plot(samples[:, :, i], 'k', alpha=0.3)
    ax.set_xlim(0, len(samples))
    # ax.set_ylim()
    ax.set_ylabel(labels[i])
axes[-1].set_xlabel('step number');
plt.savefig('Jan_Conv_TlRlFr_{:.4f}mic.png'.format(norm_spec[:, 0][ind2][0]))
plt.show()

tauss1 = np.asarray(Tauss)
[iind11] = np.where((tauss1 > 2e-6) & (tauss1 < 4.8))
Taumcmc = np.percentile(tauss1[iind11], [16, 50, 84])
q1 = np.diff(Taumcmc)
print('Tau')
print(Taumcmc[1], q1[0], q1[1])
print('Samples to discard')
discard = int(input())

flat_samples = sampler.get_chain(discard=discard, flat=True, thin=1)
prob_dist = sampler.get_log_prob(discard=discard, flat=True, thin=1)
indd = np.where(prob_dist > -6.0)
fl_samples = np.squeeze(flat_samples[indd,:])
Tl_mcmc, Rl_mcmc, Fr_mcmc = map(lambda v: (v[1], v[2] - v[1], v[1] - v[0]),
↪ zip(*np.percentile(fl_samples, [16, 50, 84], axis=0)))
fig = corner.corner(fl_samples, labels=['Tl', 'Rl', 'Fr'],
↪ show_titles=True, title_fmt='0.3e',
                    levels=(1 - np.exp(-0.5), 1 - np.exp(-2.0)),
                    truths=[Tl_mcmc[0], Rl_mcmc[0], Fr_mcmc[0]], quantiles=[0.
↪ 16, 0.5, 0.84],
                    title_kwargs={'fontsize': 12})
fig.savefig('Jan_Corner_{:.4f}mic.png'.format(norm_spec[:, 0][ind2][0]))
fig.show()

print('Best Values')
print('T_l = {:.3f} +- {:.3f} {:.3f} K'.format(Tl_mcmc[0], Tl_mcmc[1],
↪ Tl_mcmc[2]))
print('R_l = {:.3f} +- {:.3f} {:.3f} mas'.format(Rl_mcmc[0], Rl_mcmc[1],
↪ Rl_mcmc[2]))
print('Tau_l = {:.3f} +- {:.3f} {:.3f}'.format(Taumcmc[1], q1[0], q1[1]))
print('Fr = {:.3f} +- {:.3f} {:.3f}'.format(Fr_mcmc[0], Fr_mcmc[1],
↪ Fr_mcmc[2]))

```

```

    print((np.sum(I_SLModel(Tl_mcmc[0], Rl_mcmc[0], Taumcmc[1]))/
    ↪flux_tau0_1[0])-norm_spec[:,1][ind2])

    v2_model = SLModel(Tl_mcmc[0], Rl_mcmc[0], Taumcmc[1], Fr_mcmc[0])
    bsl_ord = np.argsort(bsl)
#
#####Plots#####
    plt.figure(figsize=(9,9))
    plt.xlabel(r'Spatial Frequency  $[\text{rad}^{-1}]$ ', fontsize=22)
    plt.ylabel(r'Squared Visibility', fontsize=22)
    plt.ylim(-0.05, 1.)
    index = np.random.randint(len(samples), size=100)
    for inds in index:
        sampls=f1_samples[inds]
        plt.plot(bsl[bsl_ord], SLModel(sampls[0], sampls[1],
    ↪tauss1[iind11][inds], sampls[2])[bsl_ord], 'C1', alpha=0.1)
        plt.errorbar(bsl, vis2, yerr=vis2_err2, label='Data', fnt='o',
    ↪color='limegreen')
        plt.plot(bsl[bsl_ord], v2_model[bsl_ord], c='k',
                label=r'Model T$_L$={:.3f} K, R$_L$={:.3f} mas, $\tau_L$={:.3f},
    ↪F$_r$={:.3f}'.format(Tl_mcmc[0], Rl_mcmc[0], Taumcmc[1], Fr_mcmc[0]))
        plt.tick_params(axis='both', labelsize=20)
        plt.legend(fontsize=13)
        plt.tight_layout()

    plt.savefig('Jan_vis2spf_model_{:.4f}mic.png'.format(norm_spec[:
    ↪,0][ind2][0]))
    plt.show()

    plt.figure(figsize=(9,9))
    plt.xlabel(r'Spatial Frequency  $[\text{rad}^{-1}]$ ', fontsize=22)
    plt.ylabel(r'Squared Visibility', fontsize=22)
    plt.ylim(-0.05, 1.)
    index = np.random.randint(len(samples), size=100)
    plt.errorbar(bsl, vis2, yerr=vis2_err2, label='Data', fnt='o',
    ↪color='limegreen')
    plt.scatter(bsl, v2_model, c='purple',
                label=r'Model T$_L$={:.3f} K, R$_L$={:.3f} mas, $\tau_L$={:.3f},
    ↪F$_r$={:.3f}'.format(Tl_mcmc[0], Rl_mcmc[0], Taumcmc[1],
    ↪Fr_mcmc[0]),zorder=500)
    plt.tick_params(axis='both', labelsize=20)
    plt.legend(fontsize=13)
    plt.tight_layout()
    plt.savefig('Jan_V3_vis2spf_model_{:.4f}mic.png'.format(norm_spec[:
    ↪,0][ind2][0]))

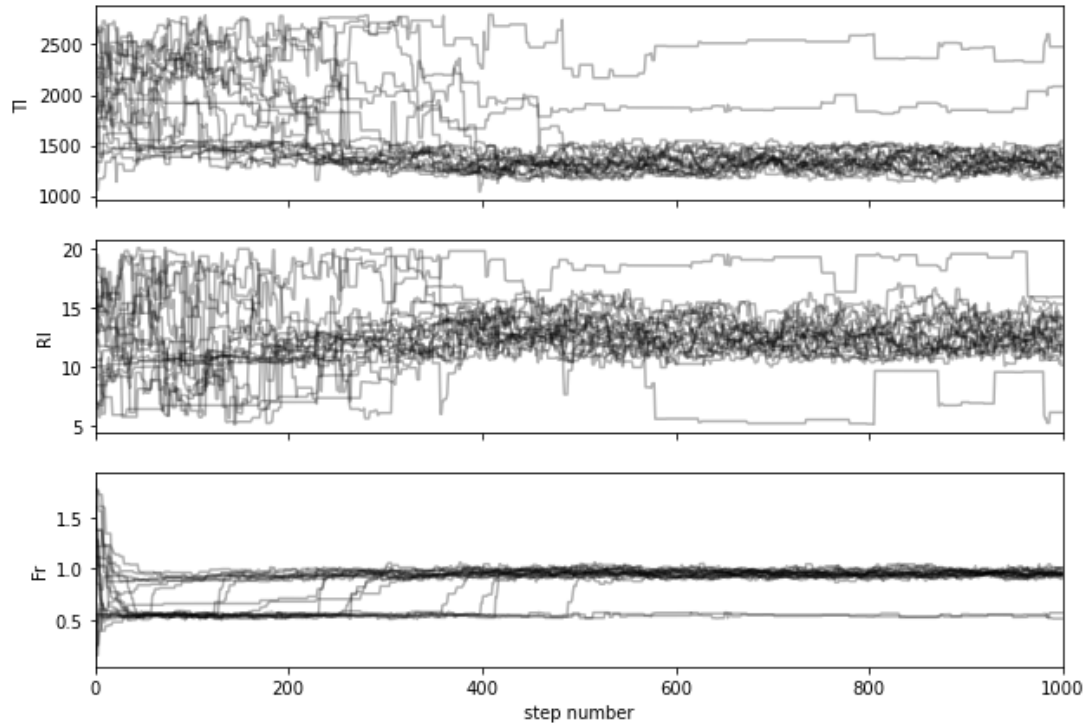
```

```
plt.show()
```

```
2.2946410354052205
```

```
2.294641013196623
```

```
100% | 1000/1000 [4:40:16<00:00, 16.82s/it]
```



```
Tau
```

```
1.7735459930550008 0.4417837826432305 0.666409310755729
```

```
Samples to discard
```

```
200
```

```
<ipython-input-30-9d9a211fa08b>:121: UserWarning: Matplotlib is currently using  
module://ipykernel pylab.backend_inline, which is a non-GUI backend, so cannot  
show the figure.
```

```
fig.show()
```

```
Best Values
```

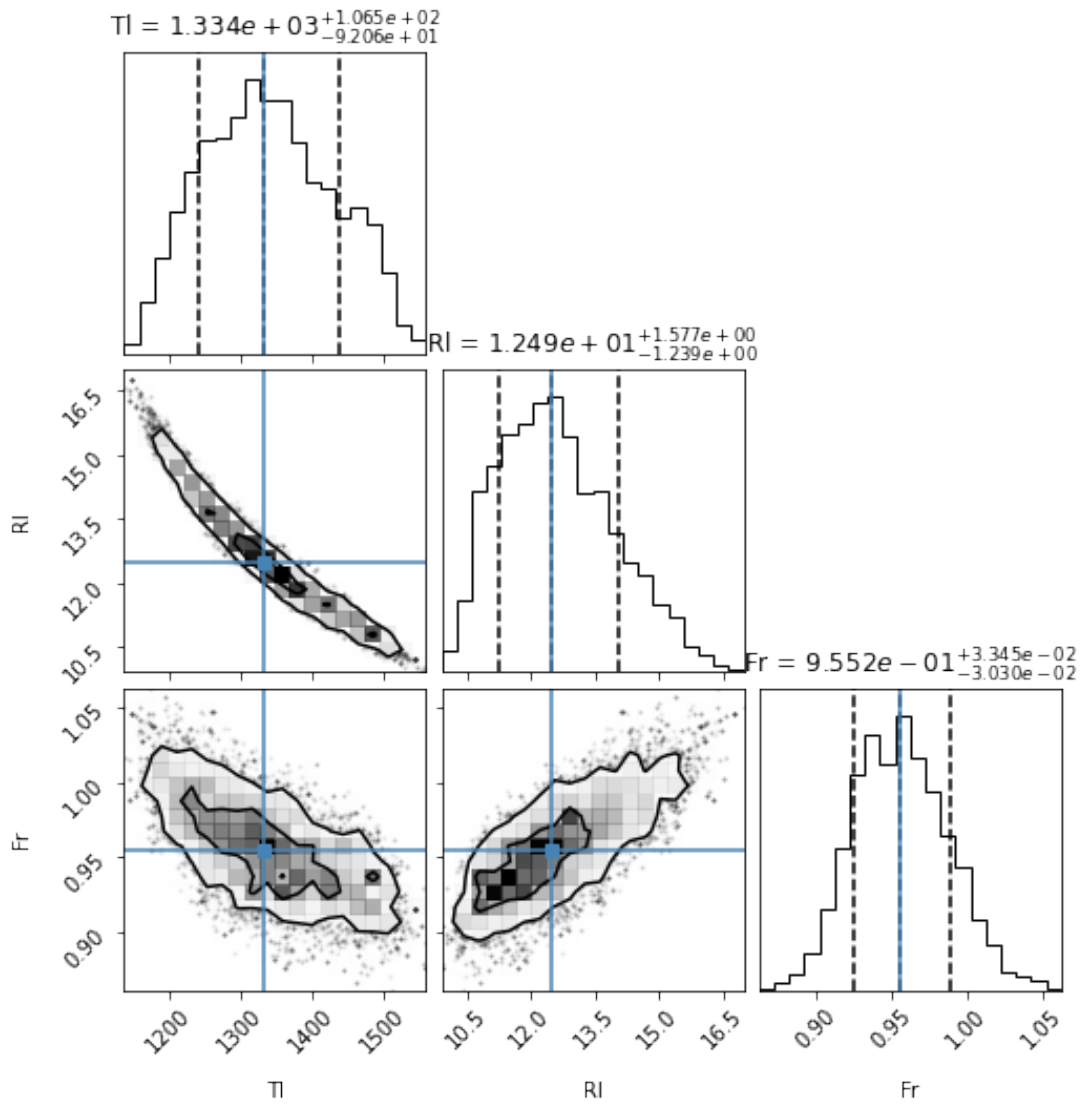
```
T_l = 1334.031 +- 106.453 92.060 K
```

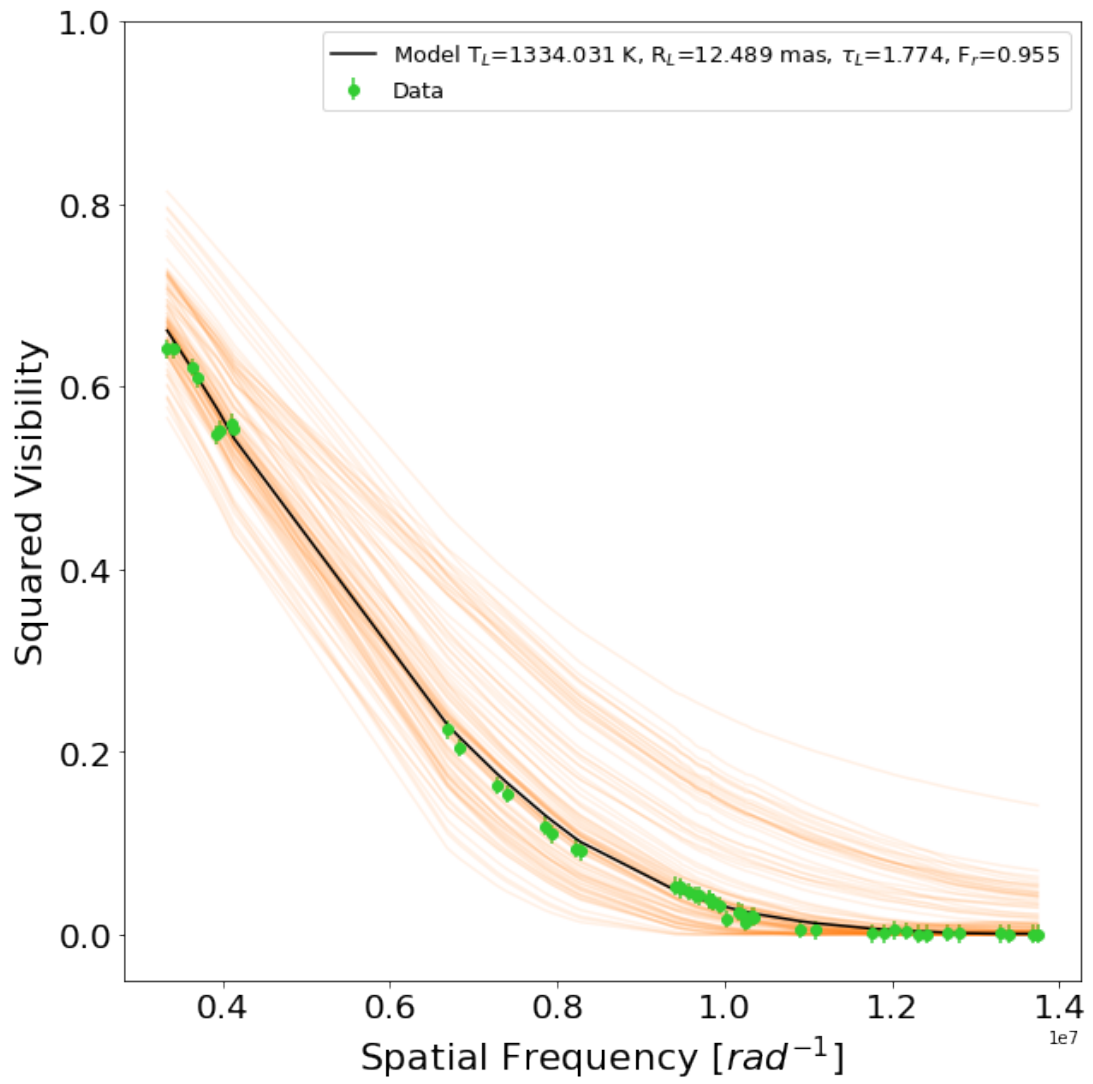
```
R_l = 12.489 +- 1.577 1.239 mas
```

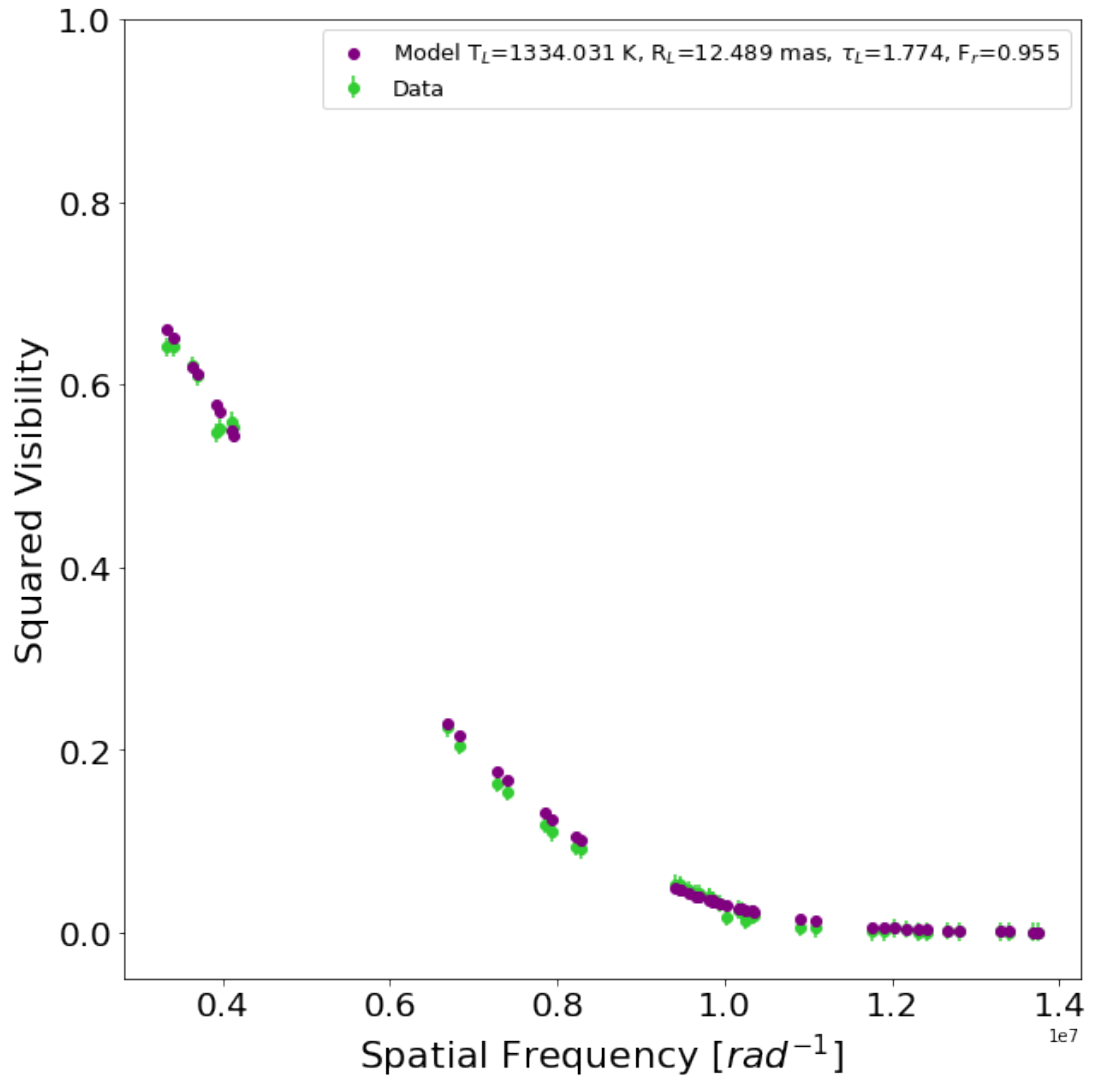
```
Tau_l = 1.774 +- 0.442 0.666
```

```
Fr = 0.955 +- 0.033 0.030
```

```
[0.0059141]
```







[Go back to top](#)

2.0.4 The following example shows how the samples from the interferometric observables were created using a bootstrapping algorithm. The different samples are created to explore different best-fit images obtained with the regularized minimization algorithm BSMEM to recover images. By generating different samples from the distribution of data points in our data help us, also, to explore slightly different u-v planes than the original distribution. This helps to ameliorate the effect of the sparseness of the u-v plane in the mean reconstructed image. The following part of the notebook (In 6 and 7) shows how those samples are obtained using the random seed generator from the Python sklearn package “resample”, which considers replacement. The example is set for one spectral channel across the pseudo-continuum (2.228 μm) but the same code could be used for other channels and OIFITS files. The final samples are stored into OIFITS files, which can be used by BSMEM for imaging the source. Notice that, for the example, only 10 different samples are created. However, this could be expanded as required by the user.

```
[6]: waves_cont = np.array([2.228]) ## Wavelength used for the example (in microns)

month = ['January']
file = 'phasediff_18_'+month[0]+'_a200_COMB_RCar_cont_'+'{:.3f}'.
    ↪format(waves_cont[0])+'.m.fits'
path=''
directory = os.path.exists(path+'bt_method/'+'{:.3f}'.format(waves_cont[0]))
if directory == False:
    print('Creating directory')
    os.system('mkdir '+path+'bt_method/'+'{:.3f}'.format(waves_cont[0]))
oi_data=pyfits.open(file)
for k in range(50):
    oi_data.writeto(path+'bt_method/'+'{:.3f}'.format(waves_cont[0])+'/
    ↪'+ 'bt{ }_'.format(k)+file, overwrite=True)
    data= pyfits.open(path+'bt_method/'+'{:.3f}'.format(waves_cont[0])+'/
    ↪'+ 'bt{ }_'.format(k)+file, mode='update')
    av2=data['OI_VIS2'].data['VIS2DATA']
    at3=data['OI_T3'].data['T3PHI']
    ### We label each data point
    numbers_v2=np.arange(av2.shape[0])
    numbers_t3=np.arange(at3.shape[0])
    ### Using the labels we create random samples of the data points allowing
    ↪replace and keeping the total number of points.
    ### This method allows us to create as many data samples as we want. In our
    ↪case we created 50
    boot_v2 = resample(numbers_v2, replace=True, n_samples=numbers_v2.shape[0],
    ↪random_state=k)
    boot_t3 = resample(numbers_t3, replace=True, n_samples=numbers_t3.shape[0],
    ↪random_state=k)
    aa=np.array(boot_v2, dtype='int')
    bb=np.array(boot_t3, dtype='int')
```

```

data['OI_VIS2'].data = data['OI_VIS2'].data[aa]
data['OI_T3'].data = data['OI_T3'].data[bb]

data.flush()
data.close()

```

```

[7]: fig4, _axs4 = plt.subplots(nrows=1, ncols=3, figsize=(15,6))
axs4 = _axs4.flatten()
colrs = plt.cm.gist_rainbow(np.linspace(0,1,10))
temp = np.random.randint(23)
axs4[0].set_xlabel(r'Spatial Frequency [rad$^{\{-1\}}$]')
axs4[0].set_ylabel(r'V$^2$')

axs4[1].set_xlabel(r'Spatial Frequency [rad$^{\{-1\}}$]')
axs4[1].set_ylabel(r'Closure Phase')

axs4[2].set_xlabel(r'UCOORD [m]')
axs4[2].set_ylabel(r'VCOORD [m]')

for k in range(10): ### Number of samples generated from the data
    #####Automatic from here#####
    oidata = pyfits.open('bt_method/2.228/bt{ }_'.format(k)+file)
    oi_wave = oidata['OI_WAVELENGTH'].data
    oi_vis2 = oidata['OI_VIS2'].data
    oi_t3 = oidata['OI_T3'].data
    waves = oi_wave['EFF_WAVE']
    vis2 = oi_vis2['VIS2DATA']
    vis2_err = oi_vis2['VIS2ERR']
    t3 = oi_t3['T3PHI']
    t3_err = oi_t3['T3PHIERR']

    u_coord = oi_vis2['UCOORD']
    v_coord = oi_vis2['VCOORD']
    u1 = oi_t3['U1COORD']
    u2 = oi_t3['U2COORD']
    v1 = oi_t3['V1COORD']
    v2 = oi_t3['V2COORD']

    nvis = vis2.shape[0]
    nt3phi = t3.shape[0]
    vis2_err2 = np.full(vis2.shape[0], 0.01)

    #####
    # To compute the UV coordinates of the closure phases:
    uv_cp = np.zeros([u1.shape[0]])
    u_cp = np.zeros([u1.shape[0]])

```

```

v_cp = np.zeros([u1.shape[0]])
u3 = -1.0 * (u1 + u2)
v3 = -1.0 * (v1 + v2)

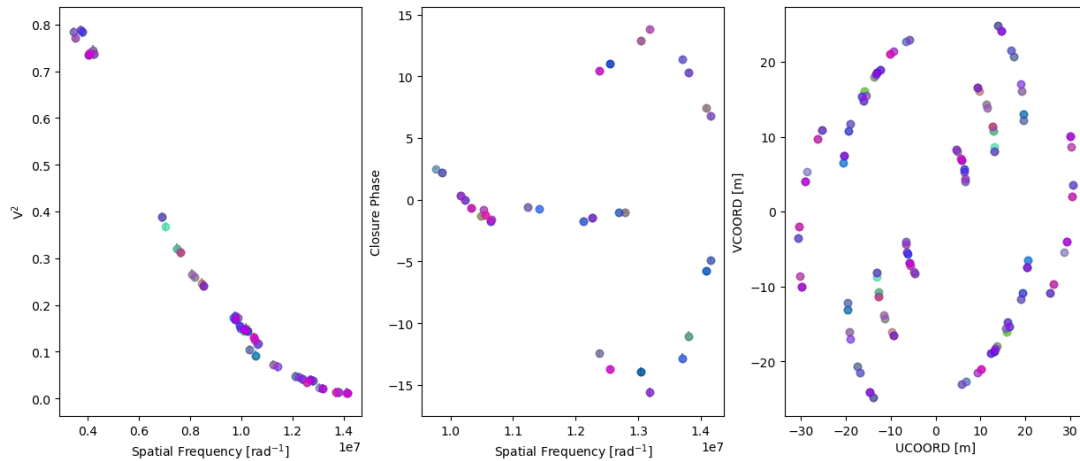
for j in range(u1.shape[0]):
    uv1 = np.sqrt((u1[j]**2 + (v1[j])**2))
    uv2 = np.sqrt((u2[j]**2 + (v2[j])**2))
    uv3 = np.sqrt((u3[j]**2 + (v3[j])**2))
    if uv1 >= uv2 and uv1 >= uv3:
        uv_cp[j] = uv1
        u_cp[j] = u1[j]
        v_cp[j] = v1[j]
    elif uv2 >= uv1 and uv2 >= uv3:
        uv_cp[j] = uv2
        u_cp[j] = u2[j]
        v_cp[j] = v2[j]
    elif uv3 >= uv1 and uv3 >= uv2:
        uv_cp[j] = uv3
        u_cp[j] = u3[j]
        v_cp[j] = v3[j]

spf_u = u_coord/waves[0]
spf_v = v_coord/waves[0]
uvvis_range = np.sqrt(spf_u**2 + spf_v**2)
uvcp_range=uv_cp/waves[0]

    ## The plots show, with different colored dots, the 10 different samples of
    the data generated.
    ## The first plot displays the samples for the squared visibilities, the
    second panel displays the closure phases
    ## and the third panel displays the u-v coverage explored, respectively.
    axs4[0].errorbar(uvvis_range, vis2, yerr=vis2_err2, fmt='o',
    color=colrs[k], alpha=0.2)
    axs4[1].errorbar(uvcp_range, t3, yerr=t3_err, fmt='o', color=colrs[k],
    alpha=0.2)
    axs4[2].scatter(u_coord, v_coord, color=colrs[k], alpha=0.2)
    axs4[2].scatter(-u_coord, -v_coord, color=colrs[k], alpha=0.2)

    oidata.close()
plt.show()

```



2.0.5 The following part of the notebook is based on the CASSINI-PCA package. The code (In 115, 116) shows an example of the Principal Component Analysis (PCA) applied to our January reconstructed images across the 1st CO band head of the R Car GRAVITY data. According to Medeiros et al., (2018), the visibilities of the Principal Components are equal to the Principal Components of the visibilities. This method is useful to trace the changes, across a set of images, which have a significant effect on the visibility (amplitude and -closure-phase) profile. In the case of the R Car data, we use the PCA to evaluate the variability of the source across wavelengths. First, we computed the PCA of the recovered images across the CO bandpass. Second, we evaluate how many of those components were needed to reproduce the interferometric observables. This allow us to filter out variable structures potentially associated with noise and/or artifacts in the image. Hence, by selecting the number of principal components that reproduce the observables we are able to trace “bona fide” variability of the target.

```
[115]: def observables(data, wave_do, wave_up, imrec):
        """
        Function that computes the observables from the data and the synthetic_
        ↪observables
        from the reconstructed image
        data = The OIFITS file containing the interferometric data
        [wave_do, wave_up] = Is the wavelength interval containing the spectral_
        ↪channel analysed
        imrec = The reconstructed image from where we extract the synthetic_
        ↪observables
        """
        scale=0.469
        npix=128
        ##### AUTOMATIC FROM HERE #####
```

```

oidata = pyfits.open(data)
oi_wave = oidata['OI_WAVELENGTH'].data
oi_vis2 = oidata['OI_VIS2'].data
oi_t3 = oidata['OI_T3'].data
waves = oi_wave['EFF_WAVE']
vis2 = oi_vis2['VIS2DATA']
vis2_err = oi_vis2['VIS2ERR']
t3 = oi_t3['T3PHI']
t3_err = oi_t3['T3PHIERR']
vis2_err2 = np.full(vis2_err.shape, 0.01)
u = oi_vis2['UCOORD']
v = oi_vis2['VCOORD']
u1 = oi_t3['U1COORD']
u2 = oi_t3['U2COORD']
v1 = oi_t3['V1COORD']
v2 = oi_t3['V2COORD']
nvis = vis2.shape[0]
nt3phi = t3.shape[0]
#####
# To compute the UV coordinates of the closure phases:
uv_cp = np.zeros([u1.shape[0]])
u_cp = np.zeros([u1.shape[0]])
v_cp = np.zeros([u1.shape[0]])
u3 = -1.0 * (u1 + u2)
v3 = -1.0 * (v1 + v2)
for j in range(u1.shape[0]):
    uv1 = np.sqrt((u1[j]**2 + (v1[j])**2)
    uv2 = np.sqrt((u2[j]**2 + (v2[j])**2)
    uv3 = np.sqrt((u3[j]**2 + (v3[j])**2)
    if uv1 >= uv2 and uv1 >= uv3:
        uv_cp[j] = uv1
        u_cp[j] = u1[j]
        v_cp[j] = v1[j]
    elif uv2 >= uv1 and uv2 >= uv3:
        uv_cp[j] = uv2
        u_cp[j] = u2[j]
        v_cp[j] = v2[j]
    elif uv3 >= uv1 and uv3 >= uv2:
        uv_cp[j] = uv3
        u_cp[j] = u3[j]
        v_cp[j] = v3[j]
[ind] = np.where((waves >= wave_do) & (waves <= wave_up))
uvvis_range = np.sqrt(u**2 + v**2)/waves[ind[0]]
uvcp_range=uv_cp/waves[ind[0]]
vis_synth, phi_synth, t3phi_synth = oitools.compute_obs_wave(data, imrec,
↪scale, 6, 4, waves[ind[0]])

```

```

vis_synth=np.squeeze(vis_synth)

    return vis2[:,ind[0]], vis2_err2[:,ind[0]], t3[:,ind[0]], t3_err[:,ind[0]],
↳vis_synth, t3phi_synth, uvvis_range, uvcp_range

def PCA_ncomps_wave(ncomps, waves, month, interval, data_pth):
    """
    Function to calculate the Principal Components of a given image data set.
    ncomps = Number of desired principal components (depends on the explained
↳variance that you want the components
        to explain)
    waves = Array with the spectral channels that you want to analyse
    month = Our data was split into two months: January and February
    interval = Continuum, 1st CO band head or 2nd CO band head
    data_pth = Path of the OIFITS files from where we extract the
↳interferometric observables (V2 and CPs)
    """
    images = np.zeros([len(waves), 128,128])
    images_smooth = np.zeros([len(waves), 128,128])
    for i in range(len(waves)):
        img_path = 'mean_img_{:}.4f'.format(month, waves[i]) # Path
↳to the mean reconstructed images
        img = pyfits.getdata(img_path)
        images[i,:,:] = img
        mn_img = np.mean(images, axis=0)
        std_img = np.std(images, axis=0)
        rmn_imgs = (images - mn_img)/std_img ### To remove the mean from all the
↳images
        images_rshp = rmn_imgs.reshape(rmn_imgs.shape[0], 128*128)
        PCAs = PCA(n_comps)
        PCAs.fit(images_rshp)
        converted_img = PCAs.fit_transform(images_rshp)
        print('Cumulative explained variance')
        print(np.cumsum(PCAs.explained_variance_ratio_))
        comp_data = np.zeros([len(waves), ncomps, 128, 128])
        mean_PCA = PCAs.mean_.reshape(128,128)
        ratio_expv_PCA = np.cumsum(PCAs.explained_variance_ratio_)
        plot_ncomp(PCAs, interval, mn_img)
        for i in range(len(waves)):
            comp1= (PCAs.components_[0].reshape(128,128)*converted_img[i,0])
            comp2 = (PCAs.components_[1].reshape(128,128)*converted_img[i,1])
            comp3 = (PCAs.components_[2].reshape(128,128)*converted_img[i,2])
            comp4 = (PCAs.components_[3].reshape(128,128)*converted_img[i,3])

            comp_data[i,0,:,:] = (comp1 + mean_PCA)*std_img + mn_img
            comp_data[i,1,:,:] = (comp1 + comp2 + mean_PCA)*std_img + mn_img
            comp_data[i,2,:,:] = (comp1 + comp2 + comp3 + mean_PCA)*std_img + mn_img

```

```

        comp_data[i,3,:,:] = (comp1 + comp2 + comp3 + comp4 +
↪mean_PCA)*std_img+ mn_img
        if waves[i] == 2.2946:
            plot_obs_ncomp(data_pth, comp_data[i], waves[i], month, ncomps,
↪interval)

def plot_ncomp(PCA_comps, month, mn_img):
    """
    Function that plots the principal components with their cumulative
↪explained variance
    for the images corresponding to the 1st CD band head centered at 2.2946
↪microns
    """
    levs = np.array([0.10, 0.30, 0.50, 0.70, 0.90, 0.95, 0.97, 0.99])
    fig1, _axs1 = plt.subplots(ncols=4, nrows=1, figsize=(15, 8))
    axs1 = _axs1.flatten()
    fig1.suptitle('Principal Components '+month, fontsize=19, y=0.75)
    axs1[0].set_ylabel('Declination [mas]', fontsize=17)
    axs1[0].set_xlabel('Right ascension [mas]', fontsize=17)
    img_ms = np.zeros([128,128])
    cv2.circle(img_ms, (64,64), 32, color=1, thickness=-1)
    for i in range(4):# Number of principal components
        axs1[i].set_xticks(np.arange(-30,40,10))
        axs1[i].set_yticks(np.arange(-30,40,10))
        axs1[i].tick_params(axis='both', labelsize=15)
        temp = np.ma.masked_where(PCA_comps.components_[i].
↪reshape(128,128)*img_ms == 0, PCA_comps.components_[i].
↪reshape(128,128)*img_ms)
        custom_cmap = copy(plt.cm.get_cmap("coolwarm"))
        custom_cmap.set_bad('gray')
        imm = axs1[i].imshow(temp, origin='lower', cmap=custom_cmap,
↪extent=[30,-30,-30,30])#, norm=norm)
        axs1[i].contour(mn_img, levels=levs*np.max(mn_img),
↪extent=[30,-30,-30,30], linewidths=(1.3,), colors='white', origin='lower',
↪alpha=0.9)
        axs1[i].text(27, 24, 'CEV = {:.4f}'.format(np.cumsum(PCA_comps.
↪explained_variance_ratio_)[i]), fontsize=17)
        cbar=fig1.colorbar(imm, ax=axs1[i], orientation='horizontal')
        cbar.formatter.set_powerlimits((0, 0))
        if i != 0:
            axs1[i].set_xticklabels([])
            axs1[i].set_yticklabels([])
            cbar.ax.tick_params(labelsize=15)
    fig1.subplots_adjust(wspace=0.05, hspace=0.0)
    fig1.savefig('')
    plt.show()

```

```

def plot_obs_ncomp(data_pth, data_comp, wave, month, ncomps, interval):
    """
    Function that generates a representative example of the Closure Phases
    ↪versus
    spatial frequencies of the data set that corresponds to the
    1st CD band-head at 2.2946 microns (gray squares). The colored dots show
    the CPs from the recovered images obtained with different numbers of
    ↪Principal Components
    data_pth = Path from where we extract the interferometric observables
    data_comp = Array containing the Eigenimages (or principal components)
    wave = spectral channel
    month = Our data were split into to months: 'January' and 'February'
    """
    fig4, _axs4 = plt.subplots(nrows=1, ncols=4, figsize=(18,5), sharey=True)
    axs4 = _axs4.flatten()
    axs4[0].set_xlabel(r'Sp. Freq. [rad-1]', fontsize=18)
    axs4[0].set_ylabel('Closure Phase [deg]', fontsize=18)
    axs4[0].set_yticks(np.arange(-200., 201, step=50))
    wave_do = (wave*1e-6)-1e-10
    wave_up = (wave*1e-6)+1e-10
    #####
    scale=0.46875
    ncomps=4
    colrs=plt.cm.jet(np.linspace(0,1,5))
    for k in range(ncomps):
        v2, v2e, t3, t3e, a, c, uvvis, uvcp = observables(data_pth, wave_do,
        ↪wave_up, data_comp[k,:,:])
        axs4[k].errorbar(uvcp, t3, yerr=t3e, color = 'gray', fmt = 'o',
        ↪marker='s')
        axs4[k].scatter(uvcp, c, zorder=50, color=colrs[k], s=10, label='N =
        ↪{}'.format(k+1))
        axs4[k].set_ylim(-201,201)
        axs4[k].legend(fontsize='xx-small', title='Number of components (N)',
        ↪title_fontsize='small')
        #####
    fig4.subplots_adjust(wspace = 0.05, hspace=0)
    fig4.savefig('PCA_t3phi_2.2946mic.png', bbox_inches='tight')
    plt.show()

```

```

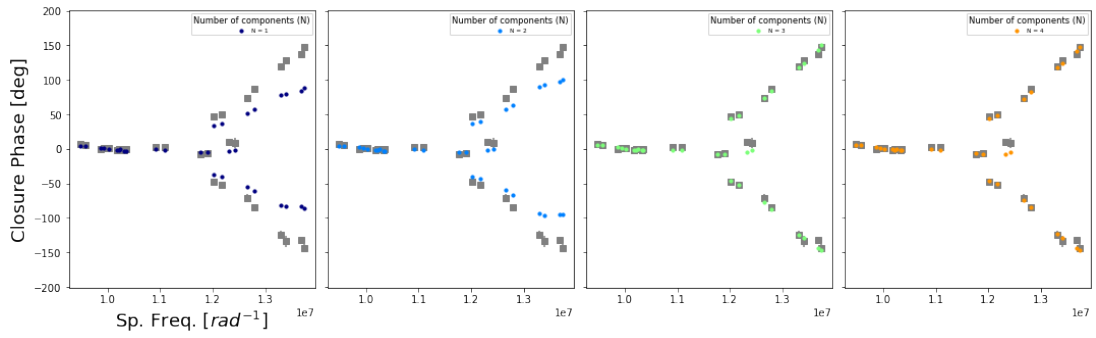
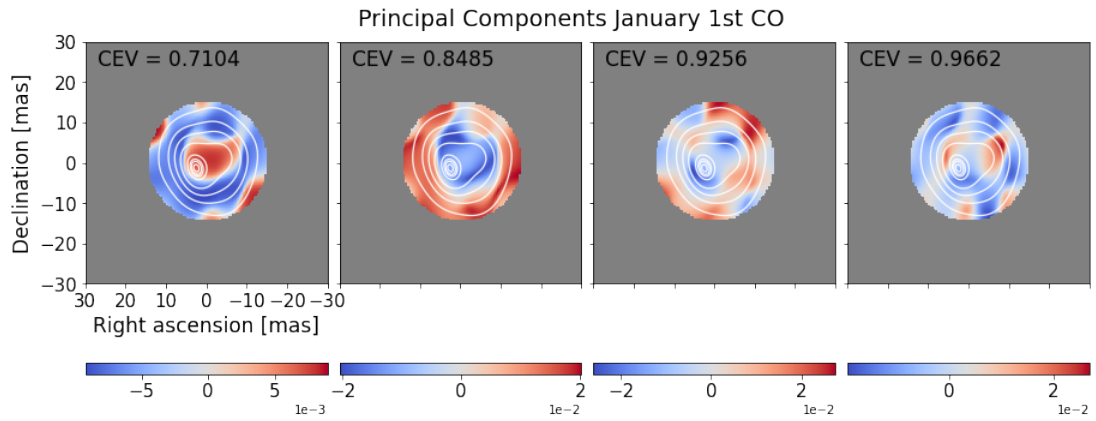
[116]: ##Calling the functions to calculate and plot the Principal Components
waves_1CD = np.array([2.2941, 2.2944, 2.2946, 2.2952, 2.2954, 2.2962, 2.2968])
↪#wavelengths of the 1st CD bandhead
Mths = ['January']
n_comps = 4 #Number of Eigenvectors containing >90% of the variance in the
↪dataset

```



```
PCA_ncomps_wave(4, waves_1CO, Mths[0], 'January 1st CO', 'January_COMB_RCar.  
↪fits')
```

Cumulative explained variance
[0.71037513 0.84848733 0.92557209 0.96618601]



Go back to top

Bibliography

- Abuter, R., Accardo, M., Amorim, A., et al. 2017, *Astronomy & Astrophysics*, 602, A94
- Akiyama, K. & Matthews, L. D. 2019, arXiv preprint arXiv:1910.00013
- Allard, F., Guillot, T., Ludwig, H.-G., et al. 2003, in *Symposium-International Astronomical Union*, Vol. 211, Cambridge University Press, 325–332
- Allard, F., Homeier, D., & Freytag, B. 2010, arXiv preprint arXiv:1011.5405
- Anugu, N., Kluska, J., Gardner, T., et al. 2023, *The Astrophysical Journal*, 950, 149
- Arroyo-Torres, B., Wittkowski, M., Chiavassa, A., et al. 2015, *Astronomy & Astrophysics*, 575, A50
- Asaki, Y., Maud, L. T., Francke, H., et al. 2023, arXiv preprint arXiv:2310.09664
- Auer, L. & Woolf, N. 1965, *The Astrophysical Journal*, 142, 182
- Babu, G. J. & Singh, K. 1983, *The Annals of Statistics*, 999
- Baldwin, J., Haniff, C., Mackay, C., & Warner, P. 1986, *Nature*, 320, 595
- Baraniuk, R., Davenport, M., DeVore, R., & Wakin, M. 2008, *Constructive Approximation*, 28, 253
- Baron, F., Monnier, J. D., & Kloppenborg, B. 2010, in *Optical and Infrared Interferometry II*, Vol. 7734, International Society for Optics and Photonics, 77342I
- Baron, F. & Young, J. S. 2008, in *Optical and Infrared Interferometry*, Vol. 7013, International Society for Optics and Photonics, 70133X

- Baud, B. & Habing, H. 1983, *Astronomy and Astrophysics*, 127, 73
- Beckers, J., Enard, D., Faucherre, M., et al. 1990, in *SPIE Conf. Ser.*, Vol. 1236, International Society for Optics and Photonics, 108–124
- Beltran, M. T., Cesaroni, R., Neri, R., et al. 2005, *Astronomy & Astrophysics*, 435, 901
- Berger, J. P. & Segransan, D. 2007, *New Astronomy Reviews*, 51, 576
- Bhatnagar, S. & Cornwell, T. 2004, *Astronomy & Astrophysics*, 426, 747
- Biegging, J. H., Rieke, M. J., & Rieke, G. H. 2002, *Astronomy & Astrophysics*, 384, 965
- Bik, A. & Thi, W. 2004, *Astronomy & Astrophysics*, 427, L13
- Bladh, S. & Höfner, S. 2012, *Astronomy & Astrophysics*, 546, A76
- Bladh, S., Liljegren, S., Höfner, S., Aringer, B., & Marigo, P. 2019, *Astronomy & Astrophysics*, 626, A100
- Boffin, H. M., Hussain, G., Berger, J.-P., & Schmidtobreick, L. 2016, *Astronomy at High Angular Resolution: A Compendium of Techniques in the Visible and Near-Infrared*, Vol. 439 (Springer)
- Bonaca, A., Tanner, J. D., Basu, S., et al. 2012, *The Astrophysical Journal Letters*, 755, L12
- Brown, A. G., Vallenari, A., Prusti, T., et al. 2021, *Astronomy & Astrophysics*, 649, A1
- Buscher, D. F. 2015, *Practical optical interferometry* (Cambridge University Press)
- Candes, E. J., Romberg, J. K., & Tao, T. 2006, *Communications on Pure and Applied Mathematics: A Journal Issued by the Courant Institute of Mathematical Sciences*, 59, 1207
- Cannon, E., Montargès, M., de Koter, A., et al. 2023, arXiv preprint arXiv:2303.08892
- Carrillo, R. E., McEwen, J. D., & Wiaux, Y. 2014, *Monthly Notices of the Royal Astronomical Society*, 439, 3591
- Carroll, B. W. & Ostlie, D. A. 2017, *An introduction to modern astrophysics* (Cambridge University Press), 82–83

- Cernicharo, J., Marcelino, N., Agúndez, M., & Guélin, M. 2015, *Astronomy & Astrophysics*, 575, A91
- Chandra, S., Maheshwari, V., & Sharma, A. 1996, *Astronomy and Astrophysics Supplement Series*, 117, 557
- Chauvin, G., Videla, M., Beust, H., et al. 2023, *Astronomy & Astrophysics*, 675, A114
- Chiavassa, A., Freytag, B., Masseron, T., & Plez, B. 2011, *A&A*, 535, A22
- Chiavassa, A., Kravchenko, K., & Goldberg, J. A. 2024, arXiv preprint arXiv:2402.00187
- Chiavassa, A., Kravchenko, K., Millour, F., et al. 2020, *Astronomy & Astrophysics*, 640, A23
- Chiavassa, A., Kravchenko, K., Montargès, M., et al. 2022, *Astronomy & Astrophysics*, 658, A185
- Chiavassa, A., Plez, B., Josselin, E., & Freytag, B. 2009, *Astronomy & Astrophysics*, 506, 1351
- Climent, J., Wittkowski, M., Chiavassa, A., et al. 2020, *A&A*, 635, A160
- Colom i Bernadich, M. 2020, *Measuring the Characteristic Sizes of Convection Structures in AGB Stars with Fourier Decomposition Analyses: the Stellar Intensity Analyzer (SIA) Pipeline.*
- Cowling, T. G. 1934, *Monthly Notices of the Royal Astronomical Society*, 94, 768
- Cox, J. P. 1963, *The Astrophysical Journal*, 138, 487
- Cox, J. P. 1968
- Cox, J. P. 2017, *Theory of Stellar Pulsation.(PSA-2), Volume 2, Vol. 31 (Princeton University Press)*
- Creevey, O., Thévenin, F., Berio, P., et al. 2015, *Astronomy & Astrophysics*, 575, A26
- Cruzalèbes, P., Jorissen, A., Chiavassa, A., et al. 2015, *Monthly Notices of the Royal Astronomical Society*, 446, 3277

- Demory, B.-O., Ségransan, D., Forveille, T., et al. 2009, *Astronomy & Astrophysics*, 505, 205
- Deutsch, A. J. 1956, *The Astrophysical Journal*, 123, 210
- Donoho, D. L. 2006, *IEEE Transactions on information theory*, 52, 1289
- Drevon, J., Millour, F., Cruzalèbes, P., et al. 2022, *Astronomy & Astrophysics*, 665, A32
- Ducati, J. 2002, *VizieR Online Data Catalog*
- Dullemond, C., Juhasz, A., Pohl, A., et al. 2012, *Astrophysics Source Code Library*, ascl
- Duvert, G., Young, J., & Hummel, C. A. 2017, *Astronomy & Astrophysics*, 597, A8
- Eddington, A. 1919, *Monthly Notices of the Royal Astronomical Society*, 79, 177
- Eddington, A. S. 1918, *Monthly Notices of the Royal Astronomical Society*, 79, 2
- Eisenhauer, F., Monnier, J. D., & Pfuhl, O. 2023, arXiv preprint arXiv:2303.00453
- Elitzur, M., Brown, J. A., & Johnson, H. R. 1989, *The Astrophysical Journal*, 341, L95
- Engels, D., Kreysa, E., Schultz, G., & Sherwood, W. 1983, *Astronomy and Astrophysics*, 124, 123
- Eriksson, K., Nowotny, W., Höfner, S., Aringer, B., & Wachter, A. 2014, *Astronomy & Astrophysics*, 566, A95
- Foreman-Mackey, D., Hogg, D. W., Lang, D., & Goodman, J. 2013, *Publications of the Astronomical Society of the Pacific*, 125, 306
- Freytag, B. & Höfner, S. 2008, *Astronomy & Astrophysics*, 483, 571
- Freytag, B., Holweger, H., Steffen, M., & Ludwig, H.-G. 1997, in *Science with the VLT Interferometer: Proceedings of the ESO Workshop Held at Garching, Germany, 18–21 June 1996*, Springer, 316–317
- Freytag, B., Liljegren, S., & Höfner, S. 2017, *Astronomy & Astrophysics*, 600, A137
- Freytag, B., Steffen, M., & Dorch, B. 2002, *Astronomische Nachrichten*, 323, 213

- Freytag, B., Steffen, M., Ludwig, H.-G., et al. 2012, *Journal of Computational Physics*, 231, 919
- Freytag, B., Steffen, M., Wedemeyer-Böhm, S., et al. 2003, *CO5BOLD User Manual*
- Gaia Collaboration. 2020, *VizieR Online Data Catalog*, I/350
- Garsden, H., Girard, J., Starck, J.-L., et al. 2015, *Astronomy & astrophysics*, 575, A90
- Gautschy-Loidl, R., Höfner, S., Jørgensen, U. G., & Hron, J. 2004, *Astronomy & Astrophysics*, 422, 289
- Geballe, T., Evans, A., van Loon, J. T., et al. 2007, in *The Nature of V838 Mon and its Light Echo*, Vol. 363, 110
- Gehrz, R. & Woolf, N. 1971, *Astrophysical Journal*, vol. 165, p. 285, 165, 285
- Gillett, F., Low, F., & Stein, W. 1968, *The Astrophysical Journal*, 154, 677
- Gilman, R. C. 1969, *Astrophysical Journal*, vol. 155, p. L185, 155, L185
- Goldreich, P. & Scoville, N. 1976, *Astrophysical Journal*, 205, 144
- Gonzalez, C. G., Absil, O., Absil, P.-A., et al. 2016, *Astronomy & Astrophysics*, 589, A54
- Goorvitch, D. 1994, *The Astrophysical Journal Supplement Series*, 95, 535
- Groenewegen, M., Baas, F., Blommaert, J., et al. 1999, *Astronomy and Astrophysics-Supplement Series*, 140, 197
- Gull, S. F. & Skilling, J. 1984, in *IEE Proceedings F-Communications, Radar and Signal Processing*, Vol. 131, IET, 646–659
- Gull, S. F. & Skilling, J. 1999, *Maximum Entropy Data Consultants Ltd.*, Suffolk, 1
- Habing, H. J. & Olofsson, H. 2013, *Asymptotic giant branch stars* (Springer Science & Business Media)
- Hadjara, M., Cruzalèbes, P., Nitschelm, C., et al. 2019, *Monthly Notices of the Royal Astronomical Society*, 489, 2595

- Haubois, X., Wittkowski, M., Perrin, G., et al. 2015, *Astronomy & Astrophysics*, 582, A71
- Hauschildt, P. H. & Baron, E. 1999, *Journal of Computational and Applied Mathematics*, 109, 41
- Herwig, F. 2000, *A&A*, 360, 952
- Hinkle, K. H., Hall, D., & Ridgway, S. 1982, *The Astrophysical Journal*, 252, 697
- Höfner, S. 2008, *Astronomy & Astrophysics*, 491, L1
- Höfner, S., Bladh, S., Aringer, B., & Ahuja, R. 2016, *Astronomy & Astrophysics*, 594, A108
- Höfner, S., Bladh, S., Aringer, B., & Eriksson, K. 2022, *Astronomy & Astrophysics*, 657, A109
- Höfner, S. & Olofsson, H. 2018, *The Astronomy and Astrophysics Review*, 26, 1
- Högbom, J. 1974, *Astronomy and Astrophysics Supplement Series*, 15, 417
- Ibrahim, N., Monnier, J. D., Kraus, S., et al. 2023, *The Astrophysical Journal*, 947, 68
- Ireland, M., Scholz, M., Tuthill, P. G., & Wood, P. R. 2004a, *Monthly Notices of the Royal Astronomical Society*, 355, 444
- Ireland, M., Tuthill, P., Bedding, T., Robertson, J., & Jacob, A. 2004b, *Monthly Notices of the Royal Astronomical Society*, 350, 365
- Ireland, M., Tuthill, P., Davis, J., & Tango, W. 2005, *Monthly Notices of the Royal Astronomical Society*, 361, 337
- Ireland, M. J., Monnier, J. D., & Thureau, N. 2006, in *Advances in Stellar Interferometry*, Vol. 6268, SPIE, 562–569
- Ireland, M. J., Scholz, M., & Wood, P. R. 2008, *Monthly Notices of the Royal Astronomical Society*, 391, 1994
- Ireland, M. J., Scholz, M., & Wood, P. R. 2011, *Monthly Notices of the Royal Astronomical Society*, 418, 114

- Isbell, J. W., Pott, J.-U., Meisenheimer, K., et al. 2023, *Astronomy & Astrophysics*, 678, A136
- Jennison, R. 1958, *Monthly Notices of the Royal Astronomical Society*, 118, 276
- Jeong, K. S., Winters, J. M., Le Bertre, T., & Sedlmayr, E. 2003, *Astronomy & Astrophysics*, 407, 191
- Jorgensen, U. G. & Johnson, H. R. 1992, *Astronomy and Astrophysics*, 265, 168
- Joyce, M. & Chaboyer, B. 2018a, *The Astrophysical Journal*, 864, 99
- Joyce, M. & Chaboyer, B. 2018b, *The Astrophysical Journal*, 856, 10
- Joyce, M. & Tayar, J. 2023, *Galaxies*, 11, 75
- Kamezaki, T., Nakagawa, A., Omodaka, T., et al. 2012, *Publications of the Astronomical Society of Japan*, 64, 7
- Karovicova, I., Wittkowski, M., Boboltz, D., et al. 2011, *Astronomy & Astrophysics*, 532, A134
- Karovicova, I., Wittkowski, M., Ohnaka, K., et al. 2013, *Astronomy & Astrophysics*, 560, A75
- Kerschbaum, F., Maercker, M., Brunner, M., et al. 2017, *Astronomy & Astrophysics*, 605, A116
- Kippenhahn, R., Weigert, A., & Weiss, A. 1990, *Stellar structure and evolution*, Vol. 192 (Springer)
- Klement, R., Schaefer, G. H., Gies, D. R., et al. 2022, *The Astrophysical Journal*, 926, 213
- Kluska, J., Malbet, F., Berger, J.-P., et al. 2014, *Astronomy & Astrophysics*, 564, A80
- Kraus, S. 2012, in *Optical and Infrared Interferometry III*, Vol. 8445, International Society for Optics and Photonics, 84451H
- Kraus, S., Hofmann, K.-H., Menten, K. M., et al. 2010, *Nature*, 466, 339
- Kupka, F. 2004, *Proceedings of the International Astronomical Union*, 2004, 119

- Labdon, A., Kraus, S., Davies, C. L., et al. 2023, *Astronomy & Astrophysics*, 678, A6
- Labeyrie, A. 1975, *The Astrophysical Journal*, 196, L71
- Lacour, S., Thiébaud, E., Perrin, G., et al. 2009, *The Astrophysical Journal*, 707, 632
- Lada, C. 1987, in *ISU Symp.* 115, Vol. 1, D. Reidel
- Lapeyrere, V., Kervella, P., Lacour, S., et al. 2014, in *Optical and Infrared Interferometry IV*, Vol. 9146, International Society for Optics and Photonics, 91462D
- Lawson, P. 2000, *Principles of long baseline stellar interferometry (JPL)*
- Le Bouquin, J. B., Berger, J. P., Lazareff, B., et al. 2011, *A&A*, 535, A67
- Le Bouquin, J.-B., Berger, J.-P., Lazareff, B., et al. 2011, *Astronomy & Astrophysics*, 535, A67
- Le Bouquin, J.-B., Lacour, S., Renard, S., et al. 2009, *Astronomy & Astrophysics*, 496, L1
- Lèbre, A., Aurière, M., Fabas, N., et al. 2014, *A&A*, 561, A85
- Lebzelter, T., Hinkle, K. H., Wood, P. R., Joyce, R. R., & Fekel, F. C. 2005, *Astronomy & Astrophysics*, 431, 623
- Ledoux, P. & Walraven, T. 1958, *Handbuch der Physik*, 51, 353
- Lena, P. 1979, *Journal of Optics*, 10, 323
- Liljegren, S., Höfner, S., Freytag, B., & Bladh, S. 2018, *Astronomy & Astrophysics*, 619, A47
- Liljegren, S., Höfner, S., Nowotny, W., & Eriksson, K. 2016, *Astronomy & Astrophysics*, 589, A130
- Lopez, B., Lagarde, S., Petrov, R., et al. 2022, *Astronomy & Astrophysics*, 659, A192
- Loup, C., Forveille, T., Omont, A., & Paul, J. 1993, *Astronomy and Astrophysics Supplement Series*, 99, 291
- Ludwig, H.-G., Caffau, E., Steffen, M., et al. 2009, arXiv preprint arXiv:0908.4496

- Maercker, M., Mohamed, S., Vlemmings, W., et al. 2012, *Nature*, 490, 232
- Magic, Z., Weiss, A., & Asplund, M. 2015, *Astronomy & Astrophysics*, 573, A89
- Malbet, F., Cotton, W., Duvert, G., et al. 2010, in *Optical and Infrared Interferometry II*, Vol. 7734, International Society for Optics and Photonics, 77342N
- Martin, R. G., Lubow, S. H., Vallet, D., Anugu, N., & Gies, D. R. 2023, *The Astrophysical Journal Letters*, 957, L28
- Matsuura, M., Barlow, M., Zijlstra, A., et al. 2009, *Monthly Notices of the Royal Astronomical Society*, 396, 918
- McDonald, I., Zijlstra, A. A., & Boyer, M. L. 2012, *Monthly Notices of the Royal Astronomical Society*, 427, 343
- Medeiros, L., Lauer, T. R., Psaltis, D., & Özel, F. 2018, *The Astrophysical Journal*, 864, 7
- Molster, F., Waters, L., & Kemper, F. 2010, *T. Henning (Lecture Notes in Physics, Vol. 815)*
- Monnier, J. D. 2003, *Reports on Progress in Physics*, 66, 789
- Monnier, J. D., Berger, J.-P., Le Bouquin, J.-B., et al. 2014, in *Optical and Infrared Interferometry IV*, Vol. 9146, International Society for Optics and Photonics, 91461Q
- Montargès, M., Cannon, E., Lagadec, E., et al. 2021, *Nature*, 594, 365
- Montargès, M., Kervella, P., Perrin, G., et al. 2014, *Astronomy & Astrophysics*, 572, A17
- Nelder, J. A. & Mead, R. 1965, *The computer journal*, 7, 308
- Neugebauer, G. & Leighton, R. B. 1969, *Two-micron sky survey: A preliminary catalog*, Vol. 3047 (Scientific and Technical Information Division, National Aeronautics and ...)
- Newville, M., Stensitzki, T., Allen, D. B., et al. 2016, *Astrophysics Source Code Library*, ascl

- Norris, B. R., Tuthill, P. G., Ireland, M. J., et al. 2012, *Nature*, 484, 220
- Norris, R. P., Baron, F. R., Monnier, J. D., et al. 2021, *The Astrophysical Journal*, 919, 124
- Nowotny, W., Aringer, B., Höfner, S., & Eriksson, K. 2013, *Astronomy & Astrophysics*, 552, A20
- Nowotny, W., Aringer, B., Höfner, S., Gautschy-Loidl, R., & Windsteig, W. 2005a, *Astronomy & Astrophysics*, 437, 273
- Nowotny, W., Aringer, B., Höfner, S., & Lederer, M. T. 2011, *Astronomy & Astrophysics*, 529, A129
- Nowotny, W., Höfner, S., & Aringer, B. 2010, *Astronomy & Astrophysics*, 514, A35
- Nowotny, W., Lebzelter, T., Hron, J., & Höfner, S. 2005b, *Astronomy & Astrophysics*, 437, 285
- Nürnberger, D. 2003, *Astronomy & Astrophysics*, 404, 255
- o Garatti, A. C., Stecklum, B., Weigelt, G., et al. 2016, *Astronomy & Astrophysics*, 589, L4
- Ohnaka, K., Hofmann, K.-H., Benisty, M., et al. 2009, *Astronomy & Astrophysics*, 503, 183
- Ohnaka, K., Weigelt, G., & Hofmann, K.-H. 2016, *Astronomy & Astrophysics*, 589, A91
- Ohnaka, K., Weigelt, G., & Hofmann, K. H. 2017, *Astronomy & Astrophysics*, 597, A20
- Ohnaka, K., Weigelt, G., & Hofmann, K.-H. 2019, *The Astrophysical Journal*, 883, 89
- Ohnaka, K., Weigelt, G., Millour, F., et al. 2011, *Astronomy & Astrophysics*, 529, A163
- Paladini, C. 2011, *Interferometry of carbon rich AGB stars (na)*
- Paladini, C., Baron, F., Jorissen, A., et al. 2018, *Nature*, 553, 310
- Pashchenko, I. N. 2019, *Monthly Notices of the Royal Astronomical Society*, 482, 1955
- Pedregosa, F., Varoquaux, G., Gramfort, A., et al. 2011, *the Journal of machine Learning research*, 12, 2825

- Perrin, G., Ridgway, S., Lacour, S., et al. 2020, *Astronomy & Astrophysics*, 642, A82
- Perrin, G., Ridgway, S., Mennesson, B., et al. 2004, *Astronomy & Astrophysics*, 426, 279
- Perrin, G., Ridgway, S., Verhoelst, T., et al. 2005, *Astronomy & Astrophysics*, 436, 317
- Perrin, G., Ridgway, S. T., Lacour, S., et al. 2020, *A&A*, 642, A82
- Pluzhnik, E. A., Ragland, S., Le Coroller, H., et al. 2009, *The Astrophysical Journal*, 700, 114
- Price, S. D. & Walker, R. G. 1976, *The AFGL Four Color Infrared Sky Survey: Catalog of Observations at 4.2, 11.0, 19.8, and 27.4 Micrometers (Air Force Geophysics Laboratories, Air Force Systems Command, United States . . .)*
- Ragland, S., Traub, W., Berger, J.-P., et al. 2006, *The Astrophysical Journal*, 652, 650
- Rau, G., Hron, J., Paladini, C., et al. 2017, *Astronomy & astrophysics*, 600, A92
- Rau, G., Paladini, C., Hron, J., et al. 2015, *Astronomy & astrophysics*, 583, A106
- Rau, U. & Cornwell, T. J. 2011, *Astronomy & Astrophysics*, 532, A71
- Rees, N. R., Izzard, R. G., & Karakas, A. I. 2024, *Monthly Notices of the Royal Astronomical Society*, 527, 9643
- Reimers, D. 1975, *Circumstellar absorption lines and mass loss from red giants*, Tech. rep., Univ., Kiel
- Renard, S., Thiébaud, E., & Malbet, F. 2011, *Astronomy & Astrophysics*, 533, A64
- Renzini, A. & Voli, M. 1981, *Astronomy and Astrophysics*, 94, 175
- Roddier, F. 1986, *Optics Communications*, 60, 145
- Rodríguez-Coira, G., Paumard, T., Perrin, G., et al. 2021, arXiv preprint arXiv:2105.09832
- Rosales-Guzmán, A., Sanchez-Bermudez, J., Paladini, C., et al. 2023, *A&A*, 674, A62
- Rosales-Guzmán, A., Sánchez-Bermúdez, J., Paladini, C., et al. 2023, *Astronomy and Astrophysics*, 674, A62

- Rosseland, S. 1949, Oxford
- Sacuto, S., Aringer, B., Hron, J., et al. 2011, *Astronomy & Astrophysics*, 525, A42
- Salaris, M. & Cassisi, S. 2005, *Evolution of stars and stellar populations* (John Wiley & Sons)
- Samus, N., Kazarovets, E., Durlevich, O., Kireeva, N., & Pastukhova, E. 2017, *Astronomy Reports*, 61, 80
- Sanchez-Bermudez, J., Hummel, C., Tuthill, P., et al. 2016a, *Astronomy & Astrophysics*, 588, A117
- Sanchez-Bermudez, J., Millour, F., Baron, F., et al. 2018, *Experimental Astronomy*, 46, 457
- Sanchez-Bermudez, J., Millour, F., Baron, F., et al. 2018, *Experimental Astronomy*, 46, 457
- Sanchez-Bermudez, J., Thiébaud, E., Duvert, G., et al. 2016b, *Reconstruction Test Report And Data Processing Cookbook*, Tech. rep., MPIA, Heidelberg, Germany
- Sanchez-Bermudez, J., Weigelt, G., Bestenlehner, J. M., et al. 2018, *Astronomy & Astrophysics*, 618, A125
- Sánchez-Monge, Á., Cesaroni, R., Beltrán, M., et al. 2013, *Astronomy & Astrophysics*, 552, L10
- Savage, B. D. & Sembach, K. R. 1991, *The Astrophysical Journal*, 379, 245
- Schaefer, G., Brummelaar, T. t., Gies, D., et al. 2014, *Nature*, 515, 234
- Schöller, M. 2007, *New Astronomy Reviews*, 51, 628
- Schwarzschild, M. 1975, *The Astrophysical Journal*, 195, 137
- Schwarzschild, M. 1975, *The Astrophysical Journal*, 195, 137
- Schwarzschild, M. & Härm, R. 1965, *The Astrophysical Journal*, 142, 855
- Shore, S. N. 2003, in *Encyclopedia of Physical Science and Technology* (Third Edition), third edition edn., ed. R. A. Meyers (New York: Academic Press), 737–747

- Skilling, J. & Bryan, R. 1984, *Monthly Notices of the Royal Astronomical Society*, Vol. 211, NO. 1, P. 111, 1984, 211, 111
- Solomon, P., Jefferts, K. B., Penzias, A. A., & Wilson, R. W. 1971, *The Astrophysical Journal*, 163, L53
- Sonoi, T., Ludwig, H.-G., Dupret, M.-A., et al. 2018, in *PHysics of Oscillating STars*. Proceedings from the PHOST (PHysics of Oscillating STars) symposium hosted by the Oceanographic Observatory in Banyuls-sur-mer (France) from 2-7 September 2018. This conference honours the life work of Professor Hiromoto Shibahashi, 27
- Strong, D. & Chan, T. 2003, *Inverse problems*, 19, S165
- Sutton, E. C. & Wandelt, B. D. 2006, *The Astrophysical Journal Supplement Series*, 162, 401
- Takeuti, M., Nakagawa, A., Kurayama, T., & Honma, M. 2013, *Publications of the Astronomical Society of Japan*, 65, 60
- Tallon-Bosc, I., Tallon, M., Thiébaud, E., et al. 2008, in *Society of Photo-Optical Instrumentation Engineers (SPIE) Conference Series*, Ser
- Tayar, J., Somers, G., Pinsonneault, M. H., et al. 2017, *The Astrophysical Journal*, 840, 17
- Thiébaud, É. 2009, *New Astronomy Reviews*, 53, 312
- Thiébaud, É. 2013, *European Astronomical Society Publications Series*, 59, 157
- Thompson, A., Moran, J. M., & Swenson Jr, G. W. 2017, *Interferometry and synthesis in radio astronomy* (Springer Nature)
- Trampedach, R., Asplund, M., Collet, R., Nordlund, Å., & Stein, R. F. 2013, *The Astrophysical Journal*, 769, 18
- Trampedach, R., Stein, R. F., Christensen-Dalsgaard, J., Nordlund, Å., & Asplund, M. 2014, *Monthly Notices of the Royal Astronomical Society*, 445, 4366
- Tremblay, P.-E., Ludwig, H.-G., Freytag, B., Steffen, M., & Caffau, E. 2013, *A&A*, 557, A7

- Tsuji, T. 2006, *The Astrophysical Journal*, 645, 1448
- Ulrich, R. K. 1970, *Astrophysics and Space Science*, 7, 71
- Vassiliadis, E. & Wood, P. 1993, *Astrophysical Journal*, Part 1 (ISSN 0004-637X), vol. 413, no. 2, p. 641-657., 413, 641
- Vehoff, S., Hummel, C., Monnier, J., et al. 2010, *Astronomy & Astrophysics*, 520, A78
- Viani, L. S., Basu, S., JM, J. O., Bonaca, A., & Chaplin, W. J. 2018, *The Astrophysical Journal*, 858, 28
- Whitelock, P. A., Feast, M. W., & Van Leeuwen, F. 2008, *Monthly Notices of the Royal Astronomical Society*, 386, 313
- Wickramasinghe, N., Donn, B., & Stecher, T. 1966, *The Astrophysical Journal*, 146, 590
- Wilson, W. J. & Barrett, A. H. 1968, *Science*, 161, 778
- Wittkowski, M., Boboltz, D. A., Driebe, T., et al. 2008, *Astronomy & Astrophysics*, 479, L21
- Wittkowski, M., Boboltz, D. A., Ireland, M., et al. 2011, *Astronomy & Astrophysics*, 532, L7
- Wittkowski, M., Chiavassa, A., Freytag, B., et al. 2016, *Astronomy & Astrophysics*, 587, A12
- Wittkowski, M., Hauschildt, P., Arroyo-Torres, B., & Marcaide, J. 2012, *Astronomy & Astrophysics*, 540, L12
- Wittkowski, M., Hofmann, K.-H., Höfner, S., et al. 2017, *Astronomy & astrophysics*, 601, A3
- Wittkowski, M. & Paladini, C. 2014, *European Astronomical Society Publications Series*, 70, 179
- Wittkowski, M., Rau, G., Chiavassa, A., et al. 2018, *Astronomy & Astrophysics*, 613, L7
- Woolf, N. & Ney, E. 1969, *Astrophysical Journal*, vol. 155, p. L181, 155, L181

- Xiong, D. & Deng, L. 2007, *Monthly Notices of the Royal Astronomical Society*, 378, 1270
- Yamamura, I., Dominik, C., De Jong, T., Waters, L., & Molster, F. 2000, *Astronomy and Astrophysics*, 363, 629
- Zoubir, A. M. & Iskander, D. R. 2004, *Bootstrap techniques for signal processing* (Cambridge University Press)